

Università degli Studi di Padova

DIPARTIMENTO DI INGEGNERIA INDUSTRIALE
DIPARTIMENTO DI TECNICA E GESTIONE DEI SISTEMI INDUSTRIALI
Corso di Laurea in Ingegneria Meccanica

TESI DI LAUREA MAGISTRALE

Assessment of the Damage Growth in Composite Laminates via DIC Analysis

Analisi dell'Evoluzione del Danno in Compositi Laminati mediante Tecniche DIC

Laureando
Giovanni Piva
Matricola 1171842

Relatore
Ch.mo Prof. Marino Quaresimin

Correlatori
Ch.mo Prof. Stephen L. Ogin
Ch.mo Dr. Iman Mohagheghian

Anno Accademico 2019–2020

Assessment of the Damage Growth in Composite Laminates via DIC Analysis



Giovanni Piva

This thesis was developed at the University of Surrey

2019

DEPARTMENT OF MECHANICAL ENGINEERING SCIENCES

University of Surrey, Guildford, Surrey, GU2 7XH, UK

*Dedicated to Daniela Mapelli,
mentor and great source of inspiration*

Abstract

Although advanced Composite Materials have only been developed over the last decades, they are used in many areas due to their excellent stiffness and strength characteristics. To avoid catastrophic breakages in composite components it is necessary to investigate the failure mechanisms of those materials. So, Non-Destructive Testing (NDT) Techniques, which can be deployed quickly and reliably, are extremely important for detecting and understanding the evolution of damage during the service life of a component.

This research investigates the application of Digital Image Correlation (DIC) as an NDT Technique for monitoring delamination defects in Fibre Reinforced Polymer (FRP) Composites. All the tested specimens, made with 8HS Glass Fibre Fabric impregnated with Epoxy Resin, were flat coupons containing fully embedded delaminations, artificially introduced during the manufacturing using PTFE film with a thickness of 0.05 mm . The Teflon inserts used had a circular or elliptical shape. From Four - Point Bending tests performed on the samples, it was found out that the driving force of the delamination growth is the transversal dimension of the insert. Thus, it was possible to divide the coupons with Single Delamination Insert into two categories: in the first, the samples with an insert having the transverse dimension of 20 mm , while in the second, those with an insert having the transverse dimension of 40 mm . Furthermore, samples having multiple circular inserts were tested.

The work has shown that the DIC Technique can be used to monitor delaminations. However, it is necessary to reach a certain load level in order to identify the effect they have on the strain and on the out-of-plane displacement field of the monitored surface. From the effects that delamination produces on the strain and on the displacement field, it is possible to evaluate its size and growth. Nevertheless, through the results obtained from the DIC analysis, both with respect to the strain field and to the out-of-plane displacement field, the delamination was constantly overestimated. The discovery of this systematic error was the result of the further verification carried out after tests, which included the measurement of the final delamination size via visual instruments.

Acknowledgements

I am indebted to Professor Stephen L. Ogin and Doctor Iman Mohagheghian of The University of Surrey for their guidance and supervision that made this research possible.

The work would not have been achievable without the assistance of Dr Abishek Dixit in the manufacturing of the specimens, of Mr Arron Evans in the testing, of Dr Ghilanè Bragagnolo and Dr Scott J. Matthews with the DIC System, and, of Dr Lucio Maragoni for the validation of the analysis.

I should like to express special thanks to my supervisor at The University of Padova, Professor Marino Quaresimin, for the opportunity given me to participate in the Erasmus Programme and for introducing me to interesting methods for the numerical modelling of the investigated phenomena.

Contents

<i>Abstract</i>	III
<i>Acknowledgements</i>	V
I Introduction	1
1 Presentation of the Work	3
1.1 Background	3
1.2 Aims and Objectives	4
1.3 Outline of the Dissertation	5
II Literature Review	7
2 Composite Materials	9
2.1 Matrix and Reinforcement	9
2.2 Damage Types	12
2.3 Fabrication Processes	14
3 Non-Destructive Evaluation Techniques	15
3.1 Introduction of NDT Techniques	15
3.2 Overview of available NDT Techniques for Composites	16
3.3 Digital Image Correlation as NDT Technique	19
3.3.1 Classification of the various Techniques and Applications	20
3.3.2 How the DIC works	22
3.3.3 Speckle Pattern, Subset and Step Size	23
3.3.4 DIC measurements as a tool for describing deformations in composites	24
4 Growth of Delamination in Composites	25
4.1 Delamination Buckling Mode	25
4.1.1 Effects of the Delamination's Size and Depth	26
4.2 Delamination tracking via DIC Technique	27

4.3	Behaviour of delaminated composite under bending . . .	28
4.4	Conclusion: Mechanisms of Delamination Growth and its Detection	29
III Methodology		33
5	Specimen Manufacturing	35
5.1	Flat Panel Manufacturing	35
5.1.1	Preliminary Operations	36
5.1.2	Wet/Hand Lay-Up	37
5.1.3	Degassing and Curing of the Laminate	40
5.2	Cutting the Flat Panel to make Specimens	41
5.3	Summary of Test Specimens	43
6	Mechanical Testing	45
6.1	Four - Point Bending Test	45
7	Digital Image Correlation (3D-DIC)	49
7.1	Experimental Arrangement	50
7.1.1	Four - Point Bending Test	51
7.2	Calibration	51
7.3	Speckle Pattern	52
7.4	Collecting and Processing	55
IV Monitoring		57
8	Preliminary Research: Assessment of the DIC Technique	59
8.1	Examination of the DIC Technique as a tool for deforma- tion analysis	59
8.2	Assessment of the DIC Technique as a tool for detecting delaminations	62
8.3	Summary: Comparison between specimens with and with- out a delamination insert	65
9	Delamination Growth in Specimens with Single Insert	67
9.1	Analysis Procedure	67
9.1.1	Starting Results	67
9.1.2	Method for measuring the Delamination Size . . .	68
9.1.3	Method for determining the Bulge Area	69
9.2	Specimens with Circular Delamination Insert ($\phi = 20$ mm)	71
9.3	Specimens with Circular Delamination Insert ($\phi = 40$ mm)	73

<i>CONTENTS</i>	IX
9.4 Specimens with Elliptical Horizontal Delamination Insert	76
9.5 Specimens with Elliptical Vertical Delamination Insert	78
10 Delamination Growth in Specimens with Double Insert	81
10.1 Specimens with $\phi_1 = 20 \text{ mm}$ and $\phi_2 = 40 \text{ mm}$ inserts	81
10.2 Specimens with $\phi_1 = 40 \text{ mm}$ and $\phi_2 = 20 \text{ mm}$ inserts	84
11 Finite Element Analysis of Specimens	87
11.1 Numerical Model of the Four - Point Bending Test on a specimen without delamination insert	87
11.2 Numerical Model of the Four - Point Bending Test on a specimen with a delamination insert	89
11.2.1 Cohesive Zone Modelling (CZM)	90
11.2.2 Simulation Results	93
V Conclusion	97
12 Concluding Remarks	99
12.1 Single Delamination Insert	99
12.1.1 Comparison between Specimens with Circular Delamination Insert ($\phi = 20 \text{ mm}$) and Specimens with Elliptical Horizontal Insert	100
12.1.2 Comparison between Specimens with Circular Delamination Insert ($\phi = 40 \text{ mm}$) and Specimens with Elliptical Vertical Insert	102
12.1.3 From the Bulge Area to the Delaminated Area: Validation Process	104
12.2 Double Delamination Insert	106
13 Possible Future Works	107
VI References	111
VII Appendices	119
A.1 Support for the description of test repeatability	121
A.2 Support for the calculation of the Bulge Area	127

List of Figures

2.1	Schematic representation of the Matrix, Reinforcement and Interface system	10
2.2	Types of Reinforcement	11
2.3	Typical Patterns of Woven Fabrics	12
2.4	Three types of Delaminations: (a) internal, (b) near-surface and (c) multiple cracking	13
3.1	Schematic representation of the X-ray method	17
3.2	Schematic representation of the Passive Infrared Thermography method	17
3.3	Schematic representation of the Pulse-Echo method	18
3.4	Three typical DIC Techniques and their imaging models, imaging systems and applicability	21
3.5	Schematic illustration of reference square subset before and after deformation, and the displacement field	22
4.1	Local and Global Mode of Delamination induced Buckling	26
4.2	Buckling Mode Map for varying delamination size and through thickness position	26
4.3	Comparison of the longitudinal strain value between the area having delamination (Target Zone) and the intact area (Reference Zone)	27
4.4	Maps of out-of-plane displacement with rigid body movement removed (Z - displacement) and maximum principal strain (ε_1) for a specimen with a 6 mm radius circular delamination subjected to increasing applied bending	28
4.5	Three modes of fracture in a cracked body	29
4.6	Approach for Delamination Growth determination	30
4.7	Qualitative approach for Delamination Growth determination: the white circles indicate the extent of the artificial delamination	31
5.1	Cutting scheme of plies from the 8HS Fibreglass Fabric roll	36

5.2	Marking scheme of plies and the specific template for 15 th layer	36
5.3	Mould for cutting the PTFE inserts	37
5.4	Initial set-up of the apparatus required for the Wet/Hand Lay-Up manufacturing method including the pooling of resin	39
5.5	Operations for positioning the PTFE inserts	40
5.6	Cutting scheme for making the coupons	42
5.7	Example of a specimen with 10 mm radius PTFE insert	42
5.8	Drilling hole scheme	43
6.1	Four - Point Loading configuration with rolling supports and rolling loading noses	46
6.2	Four - Point Bend specimen Set-Up inside Instron [®] 5982 testing rig	47
7.1	DIC Set-Up scheme with Instron [®] machine to obtain Four - Point Bending results for the compressive side of the specimen	51
7.2	Example of 10 mm Calibration board supplied by <i>Correlated Solutions</i>	52
7.3	Speckle pattern applied using aerosol cans on a finished specimen	53
7.4	Speckle pattern applied using an ink roller kit with 0.013'' dot size supplied by <i>Correlated Solutions</i> on a finished specimen	53
7.5	Speckle pattern applied using a film on a finished specimen with the underside painted in matt white	53
8.1	Bending Moment Diagram of a Four - Point Bending Beam	59
8.2	DIC Strain contours of a sample without delamination insert under load of 1000 N	60
8.3	Schematic drawing of the line along which the data for Strain measurement are extracted	60
8.4	Comparison of the DIC Strain profile along the reference line for different analysis parameters	61
8.5	DIC Strain contours of a specimen with an embedded circular delamination one-ply below the surface under an applied force of 2795 N	62
8.6	DIC Strain profiles of the specimen with $\phi = 20$ mm delamination insert during testing	63
8.7	Schematic drawing of the line along which the data for Displacement measurement are extracted	63

8.8	DIC Displacement contours of a specimen with an embedded circular delamination one-ply below the surface under an applied force	64
8.9	DIC Displacement profiles of the specimen with $\phi = 20$ mm delamination insert	64
8.10	Comparison of the Load/Extension diagram of a specimen without artificial delamination with that of one with a circular ($\phi = 20$ mm) delamination insert	65
8.11	Comparison of the Strain profile calculated with DIC along the reference line for the sample without artificial delamination and that with a $\phi = 20$ mm delamination insert .	66
8.12	Comparison of the Displacement between the sample without artificial delamination with that having it	66
9.1	Schematic drawing of the points in which the data for the thickness of specimens are measured	68
9.2	Example of the measurement method for determining the delamination size	68
9.3	Example of acquired image for measuring, through <i>pixel-mm</i> correlation, the delamination size to check the values obtained with DIC analysis	69
9.4	Schematic drawing of the lines along which the point pairs are extracted from $z - x$ and $z - y$ displacement	70
9.5	Repeatability Load/Extension diagram for specimens with Circular $\phi = 20$ mm insert	71
9.6	Repeatability Load/Extension diagram for specimens with Circular $\phi = 40$ mm insert	73
9.7	Repeatability Load/Extension diagram for specimens with Elliptical Horizontal insert	76
9.8	Repeatability Load/Extension diagram for specimens with Elliptical Vertical insert	78
10.1	Repeatability Load/Extension diagram for specimens with Double Circular Delamination insert with the smallest above	82
10.2	DIC Strain profile at the moment of the 1 st and 2 nd Pop-Up in the specimen with Double Delamination insert with the smallest above	83
10.3	Repeatability Load/Extension diagram for specimens with Double Circular Delamination insert with the biggest above	84
10.4	DIC Strain profile at the moment of the 1 st and 2 nd Pop-Up in the specimen with Double Delamination insert with the biggest above	85

11.1	The numerical geometry of Four - Point Bending Test with the Boundary Conditions	88
11.2	Comparison between the Load/Extension curve generated by the Instron [®] 5982 test machine with that generated by the numerical simulation with <i>Abaqus CAE</i>	89
11.3	Schematic of the Finite Element Model, showing an exploded view of the Sub-Laminate Layer, the Cohesive Interface Layer and the Base Layer	90
11.4	Schematic representation of the Traction - Separation Law	91
11.5	Side View and Top View of the specimen highlighting the Mesh pattern	94
11.6	Final deformation of the sample for a displacement of the load roller $z = -17.75 \text{ mm}$	94
11.7	Delamination at the final instant of the simulated test with <i>Abaqus</i>	95
11.8	Out-of-plane displacement profile of the Bulge at the End of the test for the simulation with <i>Abaqus</i> and for the DIC analysis	95
12.1	Comparison between the Average Bulge Areas of the specimens with an embedded insert having a size of 20 mm along y	101
12.2	Example of the evolution of the Bulge Area for a specimen with Circular $\phi = 20 \text{ mm}$ insert and for one with Elliptical Horizontal insert	101
12.3	Comparison between the Average Bulge Areas of the specimens with an embedded insert having a size of 40 mm along y	103
12.4	Example of the evolution of the Bulge Area for a specimen with Circular $\phi = 40 \text{ mm}$ insert and for one with Elliptical Vertical insert	103
12.5	Example of the method used to calculate the Delaminated Area with <i>ImageJ</i> [®] software	104
1	Bulge Area at different instants for Specimen 1 with $\phi = 20 \text{ mm}$ insert	128
2	Bulge Area at different instants for Specimen 2 with $\phi = 20 \text{ mm}$ insert	130
3	Bulge Area at different instants for Specimen 3 with $\phi = 20 \text{ mm}$ insert	132
4	Bulge Area at different instants for Specimen 1 with $\phi = 40 \text{ mm}$ insert	134
5	Bulge Area at different instants for Specimen 2 with $\phi = 40 \text{ mm}$ insert	136

6	Bulge Area at different instants for Specimen 3 with $\phi = 40$ mm insert	138
7	Bulge Area at different instants for Specimen 1 with Elliptical Horizontal insert	140
8	Bulge Area at different instants for Specimen 2 with Elliptical Horizontal insert	142
9	Bulge Area at different instants for Specimen 1 with Elliptical Vertical insert	144
10	Bulge Area at different instants for Specimen 2 with Elliptical Vertical insert	146

List of Tables

3.1	A summary of the applicability of NDT Techniques of different types of thick-section composites.	19
3.2	Application fields of the DIC Technique and examples of usage (source <i>Correlated Solutions</i>)	22
5.1	Lay-Up sequence for the specimens	39
5.2	Summary of test specimens used for non-destructive testing	43
7.1	Flow Chart and Output for the creation of the Speckle Pattern for the Four - Point Bend Specimen	54
9.1	Values of the Delamination main Size for samples with $\phi = 20 \text{ mm}$ insert calculated with DIC Strain	72
9.2	Values of the Delamination main Size for samples with $\phi = 20 \text{ mm}$ insert calculated with DIC Displacement	72
9.3	Values of the Bulge Area for specimens with $\phi = 20 \text{ mm}$ insert	73
9.4	Values of the Delamination main Size for samples with $\phi = 40 \text{ mm}$ insert calculated with DIC Strain	74
9.5	Values of the Delamination main Size for samples with $\phi = 40 \text{ mm}$ insert calculated with DIC Displacement	74
9.6	Values of the Bulge Area for specimens with $\phi = 40 \text{ mm}$ insert	75
9.7	Values of the Delamination main Size for samples with Elliptical Horizontal insert calculated with DIC Strain	77
9.8	Values of the Delamination main Size for samples with Elliptical Horizontal insert calculated with DIC Displacement	77
9.9	Values of the Bulge Area for specimens with Elliptical Horizontal insert	78
9.10	Values of the Delamination main Size for samples with Elliptical Vertical insert calculated with DIC Strain	79
9.11	Values of the Delamination main Size for samples with Elliptical Vertical insert calculated with DIC Displacement	79

9.12	Values of the Bulge Area for specimens with Elliptical Vertical insert	80
10.1	Values of the Delamination main Size for samples with Double Circular insert, the smallest above, calculated with DIC Strain	83
10.2	Values of the Delamination main Size for sample with Double Circular insert, the biggest above, calculated with DIC Strain	85
11.1	Material properties of 8-HS Glass Woven / Epoxy laminate	88
11.2	Mechanical properties of Interface	93
12.1	Comparison between the values of the Delamination main Size for samples with Circular $\phi = 20 \text{ mm}$ insert and those with Elliptical Horizontal insert	100
12.2	Comparison between the values of the Delamination main Size for samples with Circular $\phi = 40 \text{ mm}$ insert and those with Elliptical Vertical insert	102
12.3	Comparison between the values of the Delaminated Area outside the edge of the Delamination Insert calculated respectively from the images acquired after the tests and from the results obtained with the DIC analysis	105
1	Average Thickness of specimens with $\phi = 20 \text{ mm}$ insert .	121
2	Load at the moment of the Pop-Up for specimens with $\phi = 20 \text{ mm}$ insert	121
3	Average Thickness of specimens with $\phi = 40 \text{ mm}$ insert .	122
4	Load at the moment of the Pop-Up for specimens with $\phi = 40 \text{ mm}$ insert	122
5	Average Thickness of specimens with Elliptical Horizontal insert	123
6	Load at the moment of the Pop-Up for specimens with Elliptical Horizontal insert	123
7	Average Thickness of specimens with Elliptical Vertical insert	124
8	Load at the moment of the Pop-Up for specimens with Elliptical Vertical insert	124
9	Average Thickness of specimens with Double Circular insert, with the smallest above	125
10	Load at the moment of the Pop-Up for specimens with Double insert, with the smallest above	125
11	Average Thickness of specimens with Double Circular insert, with the biggest above	126

12	Load at the moment of the Pop-Up for specimens with Double Circular insert, with the biggest above	126
13	Values for the calculation of the Bulge Area for Specimen 1 with $\phi = 20 \text{ mm}$ insert	127
14	Value of the Bulge Area at different instants for Specimen 1 with $\phi = 20 \text{ mm}$ insert	127
15	Values for the calculation of the Bulge Area for Specimen 2 with $\phi = 20 \text{ mm}$ insert	129
16	Value of the Bulge Area at different instants for Specimen 2 with $\phi = 20 \text{ mm}$ insert	129
17	Values for the calculation of the Bulge Area for Specimen 3 with $\phi = 20 \text{ mm}$ insert	131
18	Value of the Bulge Area at different instants for Specimen 3 with $\phi = 20 \text{ mm}$ insert	131
19	Values for the calculation of the Bulge Area for Specimen 1 with $\phi = 40 \text{ mm}$ insert	133
20	Value of the Bulge Area at different instants for Specimen 1 with $\phi = 40 \text{ mm}$ insert	133
21	Values for the calculation of the Bulge Area for Specimen 2 with $\phi = 40 \text{ mm}$ insert	135
22	Value of the Bulge Area at different instants for Specimen 2 with $\phi = 40 \text{ mm}$ insert	135
23	Values for the calculation of the Bulge Area for Specimen 3 with $\phi = 40 \text{ mm}$ insert	137
24	Value of the Bulge Area at different instants for Specimen 3 with $\phi = 40 \text{ mm}$ insert	137
25	Values for the calculation of the Bulge Area for Specimen 1 with Elliptical Horizontal insert	139
26	Value of the Bulge Area at different instants for Specimen 1 with Elliptical Horizontal insert	139
27	Values for the calculation of the Bulge Area for Specimen 2 with Elliptical Horizontal insert	141
28	Value of the Bulge Area at different instants for Specimen 2 with Elliptical Horizontal insert	141
29	Values for the calculation of the Bulge Area for Specimen 1 with Elliptical Vertical insert	143
30	Value of the Bulge Area at different instants for Specimen 1 with Elliptical Vertical insert	143
31	Values for the calculation of the Bulge Area for Specimen 2 with Elliptical Vertical insert	145
32	Value of the Bulge Area at different instants for Specimen 2 with Elliptical Vertical insert	145

Part I

Introduction

Chapter 1

Presentation of the Work

In this introductory chapter it is proposed a brief description of the operational field, reviewing the objectives pursued and the structure of the work carried out.

1.1 Background

Composites are relatively modern materials, their development began in the 1970s^[1]. However, they immediately established themselves in the advanced materials scenario, given their high mechanical characteristics. These are highly engineered materials designed as a function of the end-use^[2]. Because of the many benefits they guarantee, they are supplanting traditional materials in different areas. The fields of use of these materials are constantly increasing; they were initially used, given the high cost, exclusively for applications aimed at finding peak performance. Nowadays, instead, composite components can be found in the most diverse branches of engineering and not. For the realisation of the laminates, in addition to the use of unidirectional lamina, textile fabrics are also used. The choice of one material in place of the other will lead to different results. In fact, using the laminates the outcome will be highly anisotropic components. On the other hand, by using the fabrics, materials will be guaranteed balanced properties. By far the most widely used fabrics are those of the two-dimensional species, which apply in areas such as aerospace, automotive, energetic and marine sectors, thanks to the relative ease of manufacture. However, the performances that these materials guarantee are paid in terms of production costs and design times. In fact, composite components are significantly more expensive than the analogues made with traditional materials, since the starting materials and production processes are higher-priced^{[4][5]}. Moreover, during the design phase, it is necessary to consider all the possible damage and failure modes that can occur in component life, even during manufacturing^[7].

The detection of damage in composites is made difficult by the anisotropy of the material, and by the fact that the damage occurs, almost every time, within the material instead of on its surface. To address the problem of damage detection in composite materials, Non-Destructive Testing (NDT) Techniques, such as radiography, thermography, ultrasonic, and others, have been adopted^{[10][14]}. Digital Image Correlation can also be used as an inspection technique. This is an optical technique that is able to monitor the full-field deformation of structures' surfaces under load^[15]. With the DIC it is possible to identify the defects inside a component through the detection of unexpected perturbations in the surface deformation fields^{[26][27]}. Compared to traditional non-destructive inspection techniques, it is very versatile and has no particular restrictions. In fact, it is possible to monitor components of any size and shape directly in-situ, without the need to use a controlled analysis environment. Precisely because of its potential, although it has only recently established itself, the DIC is growing more and more in terms of usage between NDT Techniques, in particular for composite materials^[24].

1.2 Aims and Objectives

The general theme of this project is to investigate the application of the Digital Image Correlation as a Non-Destructive Testing Technique to detect and understand the behaviour of delaminations in GFRP fabric composites under compression. To achieve this aim, the following steps were carried out:

- the first stage consists of the production of structural elements with embedded delaminations, made up by different PTFE inserts (circular and elliptical);
- the second step is the loading of both non-delaminated and delaminated specimens, and data acquisition by using DIC, with the purpose of the identification of features and perturbations in the deformation and displacement fields for detecting the defect;
- the final phase consists of a comparison between the different out-of-plane displacements to assess the damage quantifying its size and shape.

By following these passages, it was possible to establish the effective growth of the defects and to provide values consistent with those measured via visual instrument.

1.3 Outline of the Dissertation

The dissertation is so articulated:

- the Second Part provides an in-depth literature survey concerning Composite Materials and NDT Techniques with particular attention to Digital Image Correlation;
- the Third Part describes in detail the manufacturing process of the specimens and the mechanical tests (Four - Point Bending), and the procedure for acquiring data;
- the Fourth Part reports the experimental findings from the three-dimensional image correlation measurements of the specimens undergoing compression loading and, moreover, proposes a finite element model for the simulation of the behaviour of the samples;
- the concluding remarks and suggestions for future works are summarised in the Fifth Part.

Part II
Literature Review

Chapter 2

Composite Materials

Composites are an important class of materials that is increasingly used in recent years. Nowadays, thanks to their high stiffness and strength, and also for a fairly good lightness, they are used in a wide range of applications, including: aerospace, automotive, construction, defence and energy. These are highly engineered materials as they are designed and manufactured in such a way as to ensure the best response in terms of performance according to the specific end-use. For this to be possible, a transversal knowledge of several branches of science is required.

This chapter offers an overview of the types of composites; in particular, it describes the possible solutions in terms of matrix and reinforcement, failure modes, and fabrication procedures.

2.1 Matrix and Reinforcement

Composite is a material made by combining two or more chemically and physically different phases, matrix and reinforcement, separated by a distinct interface^{[5][9]}. These phases, working together, give the composite unique properties that are far superior to those of the constituents taken individually^{[1][2]}. Therefore, through the micromechanics, by knowing the components' properties it is possible to predict the average behaviour of the lamina.

Figure 2.1 shows, at the constitutive level, a schematic fibre-reinforced lamina with a highlighted unit cell.

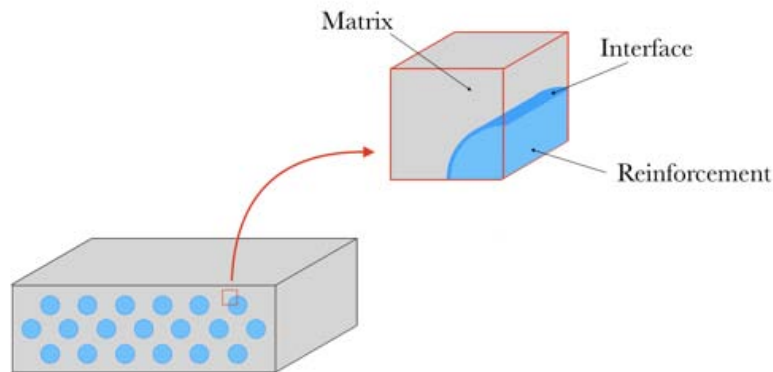


Figure 2.1: Schematic representation of the Matrix, Reinforcement and Interface system.

The matrix phase protects and supports the reinforcements, transfers load between them, and provides interlaminar shear strength. The matrix needs to have good mechanical properties. In addition, a properly chosen matrix provides resistance to heat, chemicals and moisture^[5].

Matrices can be:

- Carbon
- Ceramic
- Metal
- Polymer (Thermoset and Thermoplastic)

Among these the most adopted is the polymeric matrix, in particular the thermosets such as, for example, the epoxy resin used to produce components with high-performance characteristics. However, the choice of a matrix over another implies restrictions in the production process, in use, and in recycling at the end of the useful life.

The role of the reinforcement is to ensure stiffness and strength to the composite material. The reinforcement needs low density, so as to guarantee lightness, and, above all, high specific modulus to the material^[5].

There are different reinforcement categories depending on the type, geometry and orientation, as illustrated in the chart of Figure 2.2; yet, the one with which most high-performance composites are made is the continuous fibre.

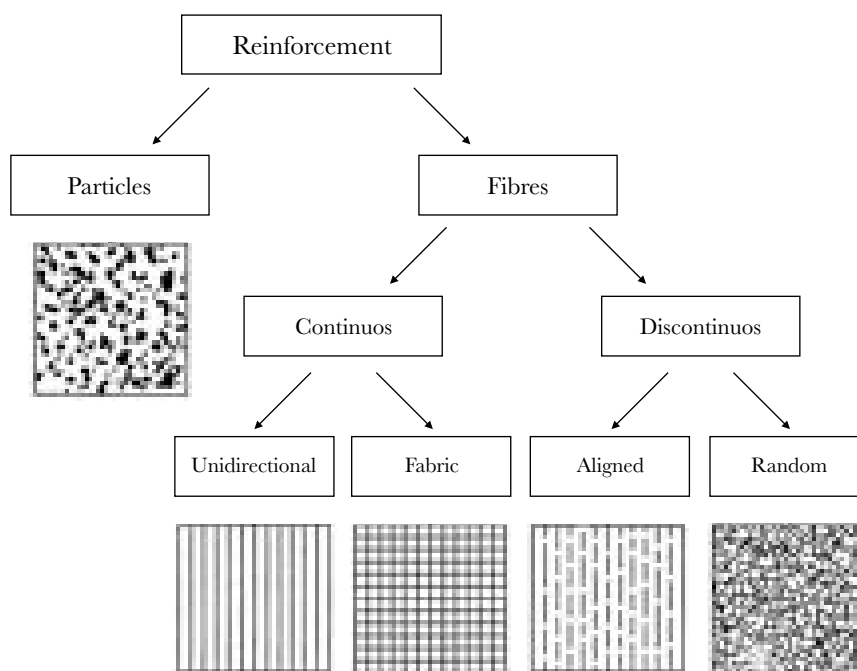


Figure 2.2: Types of Reinforcement.

The reinforcements are made by these materials:

- Aramid
- Carbon
- Ceramic
- Glass
- Metal
- Natural

Each type has its own advantages and disadvantages. The Glass fibre is the most commonly used reinforcement, because of its high tensile strength and low cost; however, only the Carbon fibre provides high stiffness in addition to strength.

Finally, the interface plays an important role in controlling the failure mechanisms (see Section 2.2), especially at the micromechanical level. In fact, a weak interface, may cause a debonding damage, because a crack propagates in parallel to the fibre along its area. By contrast, in the case of a stronger interface, the propagation of a transverse crack through the fibres and the matrix is favoured^[5].

In this work the structural elements to be tested are made out of Glass Fibre Fabric impregnated with Epoxy Resin. Glass fibre is chosen, as already mentioned, due to its high strength and low cost^[1]. Instead, epoxy resin is chosen because, thanks to its low viscosity, it can easily

be used to produce composites made of dry layers. Finally, the materials chosen allow the creation of transparent samples, which is useful for this project. Since this work aims to study the growth of delamination, 2D woven fabrics has been used. But, the woven fabrics are available as 2D or 3D reinforcements^[4]. Two-Dimensional fabrics are used when high in-plane stiffness and resistance is required. If, on the other hand, an out-of-plane load is to be faced, 3D fabrics are preferred. Moreover, 3D fabrics guarantee greater resistance to delamination^[28]. There are several type of interweaving patterns; some of the most common are shown in Figure 2.3.

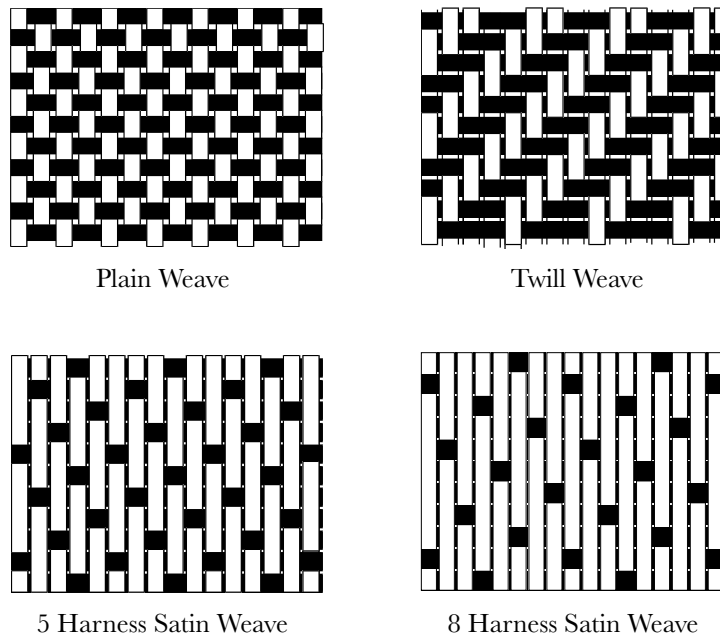


Figure 2.3: Typical Patterns of Woven Fabrics.

The 8HS Glass Fibre Fabric was chosen to manufacture the structural elements in this work, as the drapability of a satin weave is highest than that of a plane weave, meaning that it is easier to form a complex shape when needed.

2.2 Damage Types

Advanced polymeric composite materials are prone to a large number of defects and damage types, influenced by many factors: constituent materials, manufacturing processes, and in-service use of the component^[7]. Composite defects may be grouped in a variety of ways; in this work they are separated into the following categories:

- Delamination
- Fibres and Matrix Cracking
- In-service Defects

Delamination

Also termed interlaminar cracking, is one of the most frequent types of damage^[7]. In-plane cracks propagating between plies of a laminate or within a lamina, separating the constituents generates the delaminations. The main causes behind the development of delaminations are:

- Cracks parallel to the Interface
- Free Edges
- Impact Damage

Delamination may also grow, especially under static and cyclic compressive load. The laminate response to delaminations is influenced by its size and location, by the plies orientation and stacking sequence, and by the use environment. The wider the delamination is, the greater the strength loss of the laminate is. Three main types of delaminations^[3] can be distinguished from one another based on where the delaminations are situated in a structural element, as summarised in Figure 2.4. This distinction between the different types of delamination is made because, depending on where the delamination is positioned, the component is more or less affected by its effect. The delamination near the surface leads to greater instability, so this type is studied below.

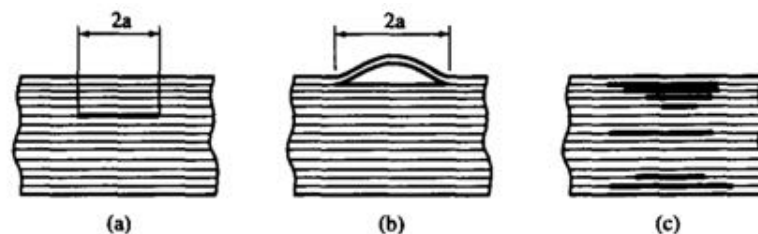


Figure 2.4: Three types of Delaminations: (a) internal, (b) near-surface and (c) multiple cracking ^[3].

2.3 Fabrication Processes

The technology with which a composite component is produced depends on the nature of matrix and fibre, and on the end-use or application. In particular, the production processes for manufacturing the thermosetting composites are:

Dry Layer:

- Wet/Hand Lay-Up
- Vacuum Infusion
- Resin Transfer Moulding
- Others (Filament Winding, Pultrusion, ...)

Pre-Impregnated Layer:

- Autoclave

The structural elements manufactured for this research are made with a technique that uses a vacuum chamber to compact, at a later time, manually laid and resin-impregnated dry layers.

Chapter 3

Non-Destructive Evaluation Techniques

Since the objective of the project is the identification of the embedded defects in the components and the evaluation of their under-load behaviour, the NDT Technique used is described below.

3.1 Introduction of NDT Techniques

The non-invasive inspection techniques are used in the science and technology industry to evaluate the properties of a component. However, they can also be employed to detect and characterise damage mechanisms by defining the size, shape and orientation of cracks and defects. The purpose of NDT Techniques is to inspect a component safely and reliably without causing damage or interruptions. For these very reasons, NDT Techniques can be used as a basis for monitoring components during or after production or even in service depending on whether the final quality or damage status of the component is checked.

The following list includes the most frequently used methods:

- Dye Penetrants Testing
- Eddy Currents Testing
- Magnetic Particle Testing
- Radiography Testing
- Ultrasonic Testing
- Visual Testing

3.2 Overview of available NDT Techniques for Composites

The development of non-destructive tests for composites is based on the experience gained with metals. However, among the methods listed in the previous paragraph, Radiography and Ultrasound are commonly used with composites, although Assisted Visual Testing is emerging recently. Eddy Currents and Magnetic Particle testing have found limited application as they require conductive and magnetic materials. Furthermore, Dye Penetrants can be used to find surface-breaking defects, but then it is difficult to remove them from the component^[10]. Given the difficult applicability to composites of some of the typical NDT Techniques of metallic materials, alternative methods such as Thermography can be used^{[13][14]}. These techniques are particularly suitable as they are more sensitive to defects such as delaminations, that run parallel to the surface of the structure. Finally, NDT Techniques can also be combined to complement each other.

There follows a brief description of the most common NDT Techniques: Radiography, Thermography, and Ultrasonic Testing.

Radiography

Radiography Testing (RT) provides for the verification of the structural internal integrity of components through the analysis of their images which are produced using film or other detectors that, is sensitive to radiation. The differential absorption of radiations from the specimen, which is due to the presence of defects, produces discernible differences when recorded on the radiographic film^[11]. The two main Radiography methods are X-ray and Neutron Radiography. Among these, there are no distinctions at the set-up level as in both cases the test sample is placed between the radiographic generator and the detector, so much that the following Figure 3.1, with the necessary changes, can be used to represent both; the different radiation wavelength distinguishes them.

Radiography allows, using radiographic images of different perspectives, to reconstruct the three-dimensional volume of components. Nevertheless, this technique has some limitations, the access to both sides of the structure and the use of contrast media in radiolucent materials is required.

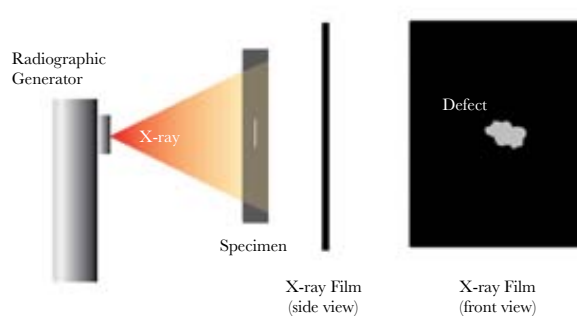


Figure 3.1: Schematic representation of the X-ray method.

Thermography

Thermography (IRT) is based on the recording of the thermal radiation emitted from the surface of a specimen by using a high-specialised infrared visual scanning technology^{[13][14]}. Then, through the images of the thermal pattern, the state of the component can be evaluated; in fact, the thermal conductivity of the material is modified by the presence of a defect which, therefore, is easily detectable. Besides, there are two approaches to thermographic inspection: Passive or Active IRT. The first one relies on the heat transmission of the material, which, therefore, must have a significantly higher or lower temperature than the background; the second, instead, on the reflection of the heat coming from an energy source able to produce a thermal contrast between the component and the rest (Figure 3.2).

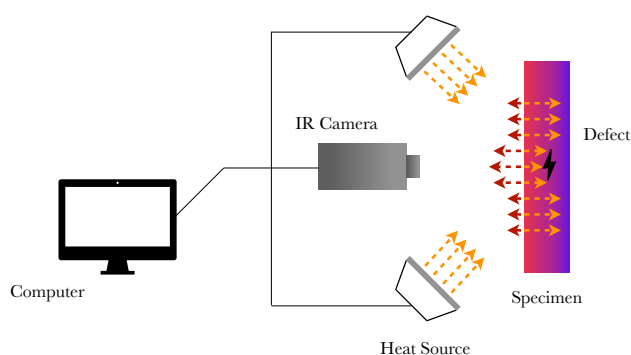


Figure 3.2: Schematic representation of the Passive Infrared Thermography method.

The strengths of this technique are its versatility and the fact that an in-situ examination can be done as the equipment does not have to be

coupled with the material; however, with that is difficult to trace the deepest defects.

Ultrasonic Testing

Ultrasonic Testing (UT) techniques are acoustic techniques commonly used to determine the presence of flaws. To do that, high-frequency sound waves on the order of $500\text{ kHz} - 10\text{ MHz}$ generated by a transducer, a piezoelectric material, are sent into the component^[13]. The sound waves, after crossing the material, are received by the same transducer or a second one; in the former case, it is about Pulse-Echo mode and in the second of Through-Transmission mode^{[10][14]}. Defects are identified by analysing the difference between the amount of energy transmitted and received, and the time of receipt; in fact, a void in the solid material reflects some energy to the transducer, which is detected and displayed (Figure 3.3).

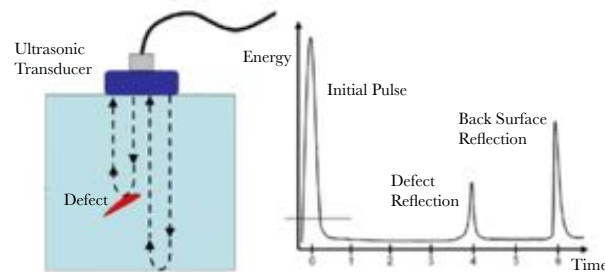


Figure 3.3: Schematic representation of the Pulse-Echo method.

Ultrasonic is the most used NDT Technique, however, there are some disadvantages. Firstly, both in the case of Pulse-Echo and in the Through-Transmission, the transducer and the material have to be coupled via liquid or solid medium, so an in-situ analysis could be complicated, particularly, when using two transducers. Furthermore, an accurate 3D mapping is required to characterise defects due to UT is not full-field.

Several revisions of the NDT Techniques available for composite materials have taken place so far. The following Table 3.1 summarises what has been proposed by Heslehurst R. B. in *Defects and Damage in Composite Materials and Structures*^[7] and Ibrahim M. E. in *Non-destructive Evaluation of Thick-Section Composites and Sandwich Structures: A review*^[12].

	Acoustic Emission	Dye Penetrant	X-Ray (Radiography)	Neutrons (Radiography)	Thermography	Pulse-Echo (Ultrasound)	Through-Transmission (Ultrasound)	Visual Inspection
Delamination	☆ ☆	☆	★		★ ★	★ ★	★ ★	★
Fibre Failure	☆ ☆		★ ★		★	★ ★	★ ★	
Inclusions				★ ★	★ ★	★ ★	★ ★	
Interfacial Cracks					★	★	★	
Macro Cracks	☆ ☆	☆	☆		★ ★	★ ★	★ ★	★
Micro Cracks		☆	☆		★ ★	★ ★	★ ★	
Moisture			★	★ ★	★			★
Porosity			★		★	★ ★	★ ★	★
Voids			★		★ ★	★ ★	★ ★	

Table 3.1: A summary of the applicability of NDT Techniques of different types of thick-section composites. The defects each technique is most capable of detecting are listed with a rating on the reliability of the technique to detect the specific defect:

- the empty star is the ability to detect defects near surface;
- the filled star is the ability to detect and characterise defects near the surface;
- two empty stars is the ability to detect defects not close to the surface;
- two filled stars is the ability to detect and characterise defects not close to the surface;
- half-filled star indicates limitations.

From this review, it follows that the detection and characterisation of defects, in particular delaminations, in solid polymer matrix composite laminates is best done using Thermographic or Ultrasound Inspection Techniques. However, since the purpose of this project is to monitor full-field delaminations, it was decided to use an Assisted Visual Testing Technique: Digital Image Correlation (DIC).

3.3 Digital Image Correlation as NDT Technique

Digital Image Correlation (DIC) is a non-contacting image-based optical method for full-field displacement and deformation measurements. DIC technique firstly acquires high-resolution digital images of an object at different loadings using digital cameras, and then quantitatively extracts full-field responses of materials to changes by comparing photographs of the various stages with the reference images^[15].

The historical route of the DIC can be divided into a phase of foundation/development and a phase of consolidation/boom. The technique was first conceived at the University of South Carolina in the early 1980s; with Sutton, *et al.*, (1983) it was introduced a method for determining full-field in-plane deformations and only in the mid-nineties it was presented the method for the measurement of out-of-plane deformations. So, the theoretical foundations and basic frameworks of DIC techniques were virtually established before 2000^[24].

However, until the 2000s, DIC techniques were not so popular because the accuracy and precision of measurements, computational efficiency, robustness, and repeatability were unsatisfactory since the instruments of that time were inadequate and too expensive. Nowadays, instead, given the advanced technological development and the now unlimited computational capacity, powerful and easily accessible digital cameras and processing hardware are available that facilitate the use of DIC techniques. Furthermore, during the first phase, the influence of the Speckle Pattern's quality, the Subset Size, the interpolation and calculation path were not fully understood.

3.3.1 Classification of the various Techniques and Applications

Classification

As shown in Figure 3.4, DIC Techniques can be divided into three main categories: 2D-DIC, 3D-DIC or Stereo-DIC and DVC^[24].

The 2D-DIC method is limited to the mere measurement of the in-plane deformation of nominal objects as it uses a single fixed camera; while to acquire accurate three-dimensional measurements of surfaces and out-of-plane deformations it is necessary to use the 3D-DIC configuration with the stereoscopic cameras. Finally, Digital Volume Correlation (DVC) is an innovative technique always for the full 3D internal measurements of objects; this technique imports the volumetric images of the analysed component at the different stages and it can calculate the complete deformation map. If, for the first two techniques, simply cameras for image acquisition are sufficient, as far as DVC is concerned, X-ray Computed Tomography (X-ray CT) or Magnetic Resonance Imaging (MRI) is required as an imaging system. Therefore, for this latter technique, the typical problems arising from the use of these technologies occur.

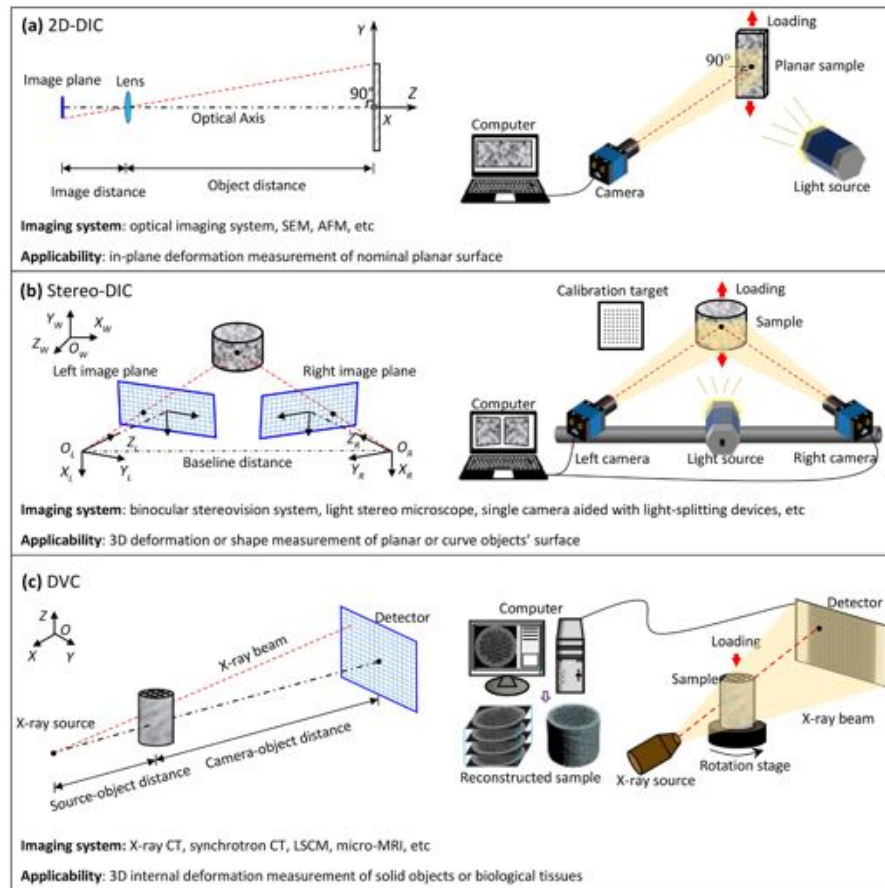


Figure 3.4: Three typical DIC Techniques and their imaging models, imaging systems and applicability^[24].

Applications

There are no limits to the scope of the DIC. That technique can be applied to any type of material, natural and artificial (e.g. wood, metal, concrete, polymer, composite material, etc.), and to any type of test (e.g. tensile, compression, shear, bending, etc). Data can be acquired to characterise a material or component by obtaining information from static or dynamic tests. Furthermore, besides the common tests, the DIC can be used for special measurements (e.g. high-temperature measurement) on a macroscopic scale or micro and even nanoscale^[24].

So, there are several applications of this technique; some examples are shown in Table 3.2.

Automotive	Aerospace
Component testing (e.g. gear, suspension, tire)	Component testing (e.g. break gear, fuel system, wings)
Vibration analysis (e.g. brake system)	Vibration analysis (e.g. engine)
High-speed crash testing	High-speed bird strike
Thermal deformation analysis	Wind tunnel
Civil	Military
Building analysis	Defence armour testing (e.g. helmet)
Earthquake analysis	Defence building testing (e.g. barricade, barrier)
Oil pipeline testing	Ballistic
Wind turbine deflection	Explosive

Table 3.2: Application fields of the DIC Technique and examples of usage (source *Correlated Solutions*).

3.3.2 How the DIC works

After recording the digital images of a test object before and after deformation, the deformed images are compared against the reference image to extract full-field displacements and strains. To do that, it is necessary to determine the position of calculation points by defining the appropriately subdivided Region Of Interest (Subset and Step Size, see Paragraph 3.3.3), and to track their motion, as schematically shown in Figure 3.5.

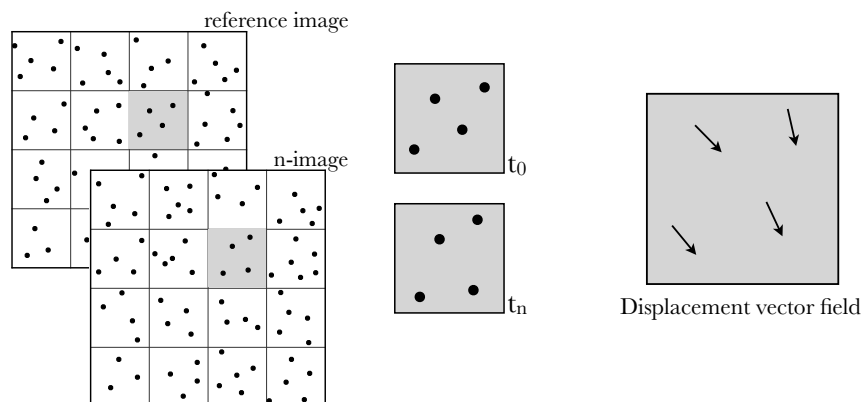


Figure 3.5: Schematic illustration of reference square subset before and after deformation, and the displacement field.

In order to evaluate the similarity (or difference) degree between the reference subset and its deformed counterpart, a correlation criterion must be defined^[19]. The correlation methods, in the literature, are classified into: Cross-Correlation (CC), Sum of Squared Difference (SSD), and Parametric Sum of Squared Difference (PSSD). Nowadays, the most robust Zero-mean Normalised Sum of Squared Difference (ZNSSD) criterion is used, thanks to an almost insensitivity to noise^[24].

The deformation field is evaluated by derivatives of the calculated displacement field. In fact, using the grid of data points containing information on the X, Y, and Z positions as well as the U, V, and W displacement vectors, a local mesh (triangles mesh) of the data points is created. The difference in displacement between the points is used to compute a strain tensor. And, since this is done for all the triangles within the grid of data points, it is possible to define the deformation field^[28].

3.3.3 Speckle Pattern, Subset and Step Size

The most important parameters related to the calculation in DIC softwares are Speckle Pattern, Subset Size and Step Size; so, a number of studies have been conducted on those (Lecompte *et al.* (2006), Yaofeng *et al.* (2007), Pan *et al.* (2008), and Pan (2018)).

It is essential that there is an adequate speckle pattern: the pattern needs to be high-contrast opaque black and white random dots. Moreover, it is important to avoid repeating textures as they could cause interpretation problems during data processing.

In order to obtain a correlation able to guarantee good results, it is important to find the optimal size of the Subset by which the image is subdivided during the data processing. It is necessary that each subset is sufficiently large so as to ensure an appropriate degree of uniqueness and distinctiveness, but, in any case, limited so as to avoid the possibility of having similar zones. Furthermore, given that for each box, there is only one reference point, and hence analysis, a high subset limits the details, so it is necessary to find the right compromise so as to have a reliable and reasonably detailed measurement.

The last parameter to define is the Step Size, which defines the spacing of the pixels being analysed during the correlation^[20]. In fact, a step size of 1 means the software will perform analysis on every pixel individually, while, for example, a step size of 10 means that the software is tracking the deformation of the subset areas every 10 pixels. Thus, the lower the step size, the higher the computational resources required for the analysis will be.

Therefore, it is necessary to find the combination between Subset and Step Size able to guarantee the best results. However, this may not be sufficient as there is a further parameter, the Filter Size (see Paragraph 7.4), which affects the quality of the results. With this parameter it is possible to modify the size of the ideal strain gauge with which the average deformation value of the area of interest is calculated.

3.3.4 DIC measurements as a tool for describing deformations in composites

DIC is a promising technique for evaluating composite laminates' characteristics; in fact, from the measurement of the strain field it is possible to obtain the elastic constants, which are usually obtained starting from the stress-strain curves determined by the use of an electromechanical extensometer. This is, because DIC can be thought of as an optical extensometer^[26].

In addition to the determination of elastic constants, the DIC techniques help to better understand the damage mechanisms in composites, since the damage events manifest themselves in the strain distribution through a singularity.

Chapter 4

Growth of Delamination in Composites

Delamination is one of the most common failure modes in composite laminates; particularly, when these are subjected to compressive loads, care should be taken during the design process to limit this type of damage. In fact, under compressive loads, the region bounded by delamination and the laminate free surface is liable to buckle locally forming a blister on the panel surface, thereby creating conditions conducive of delamination growth, and consequent global failure of the structure^[30].

4.1 Delamination Buckling Mode

Several studies have been conducted on the Compressive Buckling of composite laminates with embedded delamination (Hu N. *et al.* (1999), Short G. J. *et al.* (2002), and Rhead A. T. *et al.* (2017)). Depending on the size and shape of delaminations, and on its position through-thickness, three different modes of buckling behaviour occur; but to facilitate the discussion is preferred to refer only to Local and Global Buckling Mode (Figure 4.1). The first is characterised by the out-of-plane displacement of the upper surface of the laminate in the opposite direction to that of the lower surface, in particular, the bulge of the area above the delamination occurs. Conversely, when the sub-laminates above and below the delamination buckle in the same direction, the Global Buckling Mode occurs which is similar to that of an intact plate.

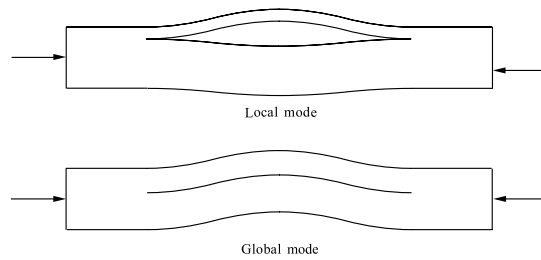


Figure 4.1: Local and Global Mode of Delamination induced Buckling^[31].

4.1.1 Effects of the Delamination's Size and Depth

Due to small delaminations, the plate in compression buckles globally, so the delamination does not affect the failure mode. Conversely, for large delaminated areas, the plaque deforms in local mode presenting the bulge of the upper thin layer. Instead, as the depth of the embedded delaminated area increases, the opening possibility of delamination is reduced. So, only if the delaminated area is close to the surface of the plate, that will be deformed with a Local Buckling Mode.

Thus, the behaviour of composite laminates containing delaminations of different size and position can be characterised by using the following Buckling Mode Map shown in Figure 4.2.

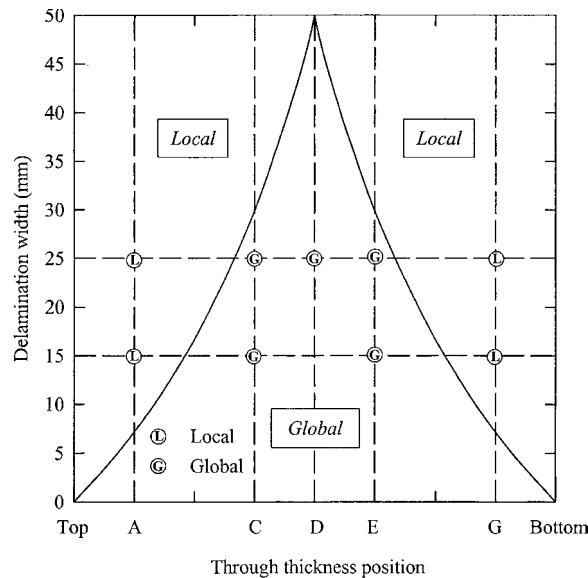


Figure 4.2: Buckling Mode Map for varying delamination size and through thickness position^[31].

To use the previous map, it must be adapted adequately since the y – $axis$, relative to the delamination dimensions, is valid for square-shaped delaminations.

Finally, the delamination’s shape also plays an important role, delamination with major size perpendicular to the loading direction facilitates the formation of the bulge and the consequent advancement of the defect^[30].

4.2 Delamination tracking via DIC Technique

Given that under load the part of the sample where there is a defect such as delamination will deform differently than the intact part due to the altered interaction between the adjacent layers, this defect is easily detectable with the DIC Technique^[35]. In fact, the influence of the delamination position on the strain distribution can be observed in the following Figure 4.3 where the strain singularities indicate the damaged area.

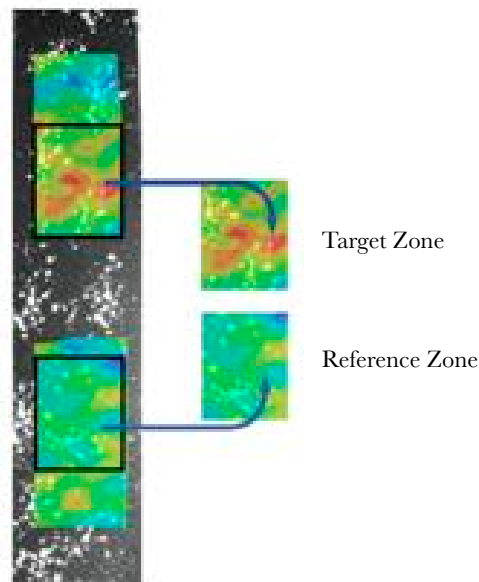


Figure 4.3: Comparison of the longitudinal strain value between the area having delamination (Target Zone) and the intact area (Reference Zone)^[34].

4.3 Behaviour of delaminated composite under bending

Gong *et al.* investigated in *An experimental study of the behaviour of delaminations in composite panels subjected to bending*, the behaviour of composites, containing near-surface embedded delamination, subject to Four - Point Bending, in particular, the failure phenomena and damage mechanisms. Therefore, in order to enhance the understanding of the interaction between the buckling behaviour and the delamination growth, in that work the influence of the shape and the size of the delamination area was studied. If the shape of the delamination is circular, the delamination growth is driven initially by buckling behaviour in the transverse direction. But then, at the increasing of the applied load, matrix cracks arise along the longitudinal direction in increasing numbers and caused the delamination to extend in that direction. An example of this behaviour is shown in Figure 4.4.

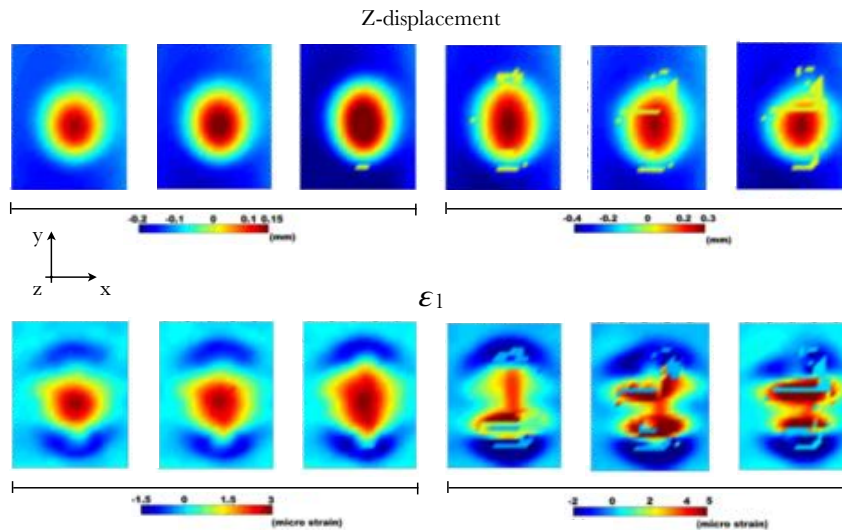


Figure 4.4: Maps of out-of-plane displacement with rigid body movement removed (Z - displacement) and maximum principal strain (ε_1) for a specimen with a 6 mm radius circular delamination subjected to increasing applied bending^{[35][36]}.

Finally, the critical load of instability is a function of the size of the delamination, in fact, there exists a minimum dimension (radius of 4 mm) below which the bulge typical of the local buckling does not form on the laminate surface^[35].

4.4 Conclusion: Mechanisms of Delamination Growth and its Detection

Mechanisms

Compression loads are harmful to composite plates with embedded delaminations as these could grow if the structures had a local buckling. The mechanisms controlling the initiation and growth of delamination are the Mode I and Mode II forces at the defect boundary; in particular, the Opening Mode, which is the main driving force, since composites exhibit a higher fracture resistance into the Sliding Mode than in this one^[37].

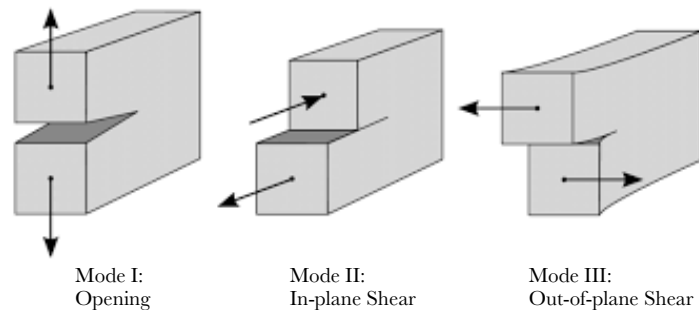


Figure 4.5: Three modes of fracture in a cracked body.

The propagation of the delaminations occurs transversely to the loading direction; although defects initially have a circular shape, the compressive load always generates an elliptical blister with the major axis perpendicular to the load. The elliptical shape of the blister can be attributed to the curvatures all around the defect edge caused by the bulging out of the delaminated layers^[40].

In conclusion, the direction and rate of growth of the delamination are governed by the type of composite material, the position of the initial delamination, and the applied external load.

Detection

For the analytical determination of the delamination growth, a criterion^[37] based on the components of the energy release rate (SERR) G_I , G_{II} and G_{III} is used. In the FEA of composite structures, it is assumed that the linear elastic fracture mechanics (LEFM) is applicable so that the growth of cracks can be predicted. Thus, a crack in a structure under load will propagate only if the SERRs exceed the fracture resistance of the material, that is the critical energy release rates^[39].

Instead, to determine from the collected experimental data the beginning of delamination and to trace its propagation, the following methods can be used:

- the correlation between the out-of-plane displacement along the main axes of the elliptical bulge and the distance along the chosen axis;
- the correlation between the strain field along the main axes of the elliptical bulge and the distance along the chosen axis;
- the qualitative investigation through the virtual overlap of the DIC images of the delamination present in the component.

The first method, which was proposed by Reeder J. R *et al.*, in *Postbuckling and growth of delaminations in composite plates subjected to axial compression*, is illustrated in Figure 4.6.

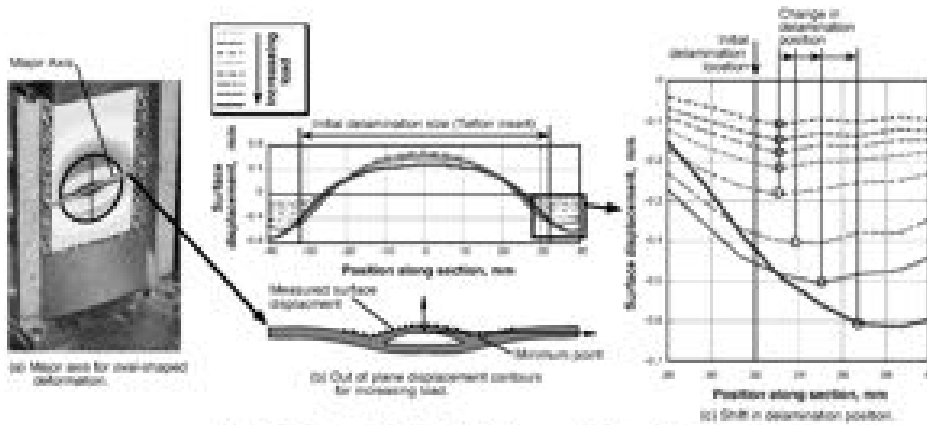


Figure 4.6: Approach for Delamination Growth determination^[38].

As shown in the Figure, Reeder uses the minimum value of the out-of-plane deformation to evaluate the delamination growth since, at that value, there is a considerable variation in the slope of the curve. Although that point probably does not correspond exactly to the delamination front, the author believes that a given shift at that point due to the change from a certain load level to the next corresponds to an equal shift in the position of the delamination front. Then, if the original size of the delamination is known, it is possible to determine the size of the delamination at an imposed load level by adding the shift position to the original size^[38].

The procedure just described can also be followed for the second method by considering the deformation along a specific line of the component's section, e.g. ε_{xx} against the horizontal mid-line.

Instead, in the last, it is used to overlap on the DIC images the delamination shape as a benchmark of the real, and it is believed that the embedded delamination in the component propagates if the bulge is, in subsequent images at higher loads, no longer contained within the reference form (Figure 4.7). For this method, it is necessary to be aware of the geometry and position of the initial delamination.

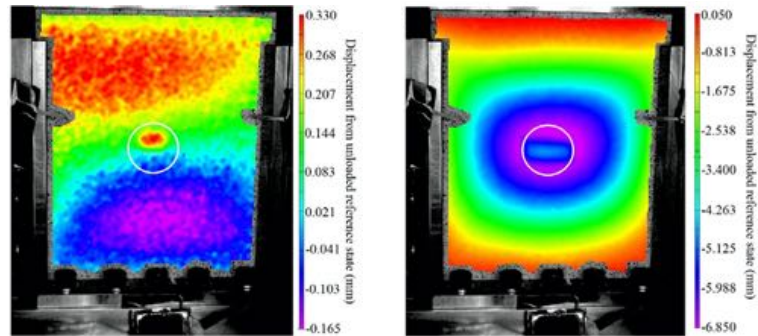


Figure 4.7: Qualitative approach for Delamination Growth determination: the white circles indicate the extent of the artificial delamination^[33].

Part III
Methodology

Chapter 5

Specimen Manufacturing

With this chapter aims to indicate the guidelines for specimens' preparation.

5.1 Flat Panel Manufacturing

All the specimens were made with 8-Harness Satin (8HS) GFRP Fabric, impregnated with epoxy resin. This type of fabric was selected by its high drapability that guarantees the realisation of complex shape structures. The fabric and resin are selected to obtain, after curing, a sufficiently transparent panel that allows to visually inspect the damage growth under load.

The chosen Lay-Up is a cross-ply $[(0/90)/(90/0)]_{4S}$. This 16 plies configuration has been selected in order to have a bending stiffness, undergoing bending (see Chapter 6 Mechanical Testing: Four - Point Bending), such as to guarantee the use of the DIC as Non-Destructive Testing Technique to evaluate at best the strain even for smaller displacements.

The following steps were necessary for the correct realisation of the flat panel:

- cutting the fabric and cutting the delamination inserts (see Paragraph 5.1.1 Preliminary Operations);
- preparing the resin and plies laying (see Paragraph 5.1.2 Hand Lay-Up);
- degassing, curing and post-curing the laminate (see Paragraph 5.1.3 Degassing and Curing of the Laminate).

5.1.1 Preliminary Operations

Cutting the Glass 8HS Fabric

The plies, which were used for the manufacturing of the panel, have dimensions of $310 * 305 \text{ mm}$. A roll of 8HS Glass Fibre Fabric with a width of 920 mm was available, it was entirely exploited to obtain, simultaneously, three sheets. In fact, after unrolling about a meter on the work table, the cutting pattern was marked using a sharpie with the help of a meter ruler (Figure 5.1). The fabric was then carefully cut out using sewing scissors. The dimensions of the cut plies were verified using a paper stencil.

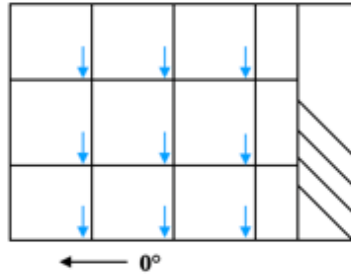


Figure 5.1: Cutting scheme of plies from the 8HS Fibreglass Fabric roll.

The direction of 90 bundles of the fabric was marked with an arrow at the corner of each cutting ply (Figure 5.2). Whereas in the 15th ply was also marked the centres where will be positioned the PTFE inserts during the manufacturing of the panel (Figure 5.2).

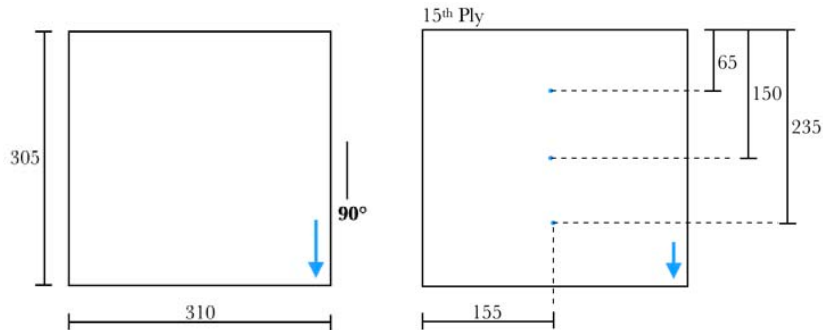


Figure 5.2: Marking scheme of plies and the specific template for 15th layer.

Cutting the PTFE Delamination Insert

The artificial delamination is generated using a PTFE film of 0.05 mm thick as an insert, that was placed between the first or upper and the second layers. The selected shapes of the insert were circular and elliptical, circles with 10 mm and 20 mm radius, and ellipses with the minor axis of 20 mm and major of 40 mm were used. The first type of inserts was realised cutting the PTFE film by a hollow circular mould with the sharp end (Figure 5.3) while the others by hand using a blade.



Figure 5.3: Mould for cutting the PTFE inserts.

5.1.2 Wet/Hand Lay-Up

Resin Preparation

From previous trials, the necessary amount of resin required, for the manufacturing process, was determined. Due to a huge amount of resin, two identical batches were contemporary produced.

The resin was created by a $100 : 60 : 4$ ratio weight as specified by the suppliers, by mixing:

- 175.0 g of epoxide 300 resin;
- 105.0 g of MNA hardener;
- 7.0 g of Ancamine K61B curing agent.

All the quantities were measured by a scale accurate to 0.001 g .

After the measure, the resin was mixed slowly by hand for 5 minutes at room temperature. Then, while the beakers were partially submerging, the bottom and sides, in warm water, approximately at $35\div 40\text{ }^{\circ}\text{C}$, it was proceeded to homogenise for another 5 minutes. The mixing was slow

in order to obtain the minimum numbers of air bubbles. Nevertheless, in order to remove the remaining air, the two beakers were put into a Vacuum Oven at 60 °C with 1 bar vacuum pressure. The degassing time was of 50 minutes.

Specimen manufacturing

The Wet/Hand Lay-Up method requires a stiff flat working surface. Consequently, two steel plates were used in different timing, like a basement (400 * 400 mm) and as mould a PTFE frame (325 * 325 mm) and two tempered glass plates (400 * 400 mm and 300 * 300 mm).

In order to accomplish a correct preparation of the mould, the surfaces of the glass plates were cleaned and waxed and then, along with the steel basement, put into the Oven at 100 °C for 1 hour. The operation was undertaken while the resin was degassing. Then, the heat plate was heated up, in order to reduce the viscosity of the resin once poured on the mould. In the meantime, the frame, which consisted of four beams with a section of 25 * 25 mm, was built by tightening two screws for each corner. Using the frame has proved to be a good solution for helping the operator with the positioning of the plies, and, moreover, to limit the resin leakage.

After a certain amount of time, both the steel plates and the larger glass plate were removed from the oven and stacked on each other on the working surface. Then, a sheet of Melinex[®] Coated (approximately 450 * 450 mm) was attached by applying the tacky tape at the bottom of the frame; thus, these were placed above the glass plate. Eventually, after all these steps, the mould is ready to use.

The panel was realised by the following step:

- (1) an amount of resin was poured onto the centre of the sheet (Figure 5.4);
- (2) one layer of fabric was laid checking the right verse with the Lay-Up Table (Table 5.1);
- (3) a sheet of Melinex[®] Uncoated (approximately 350 * 350 mm) was placed over the fabric and with a hand roller the resin has flowed across the fabric;
- (4) the last sheet of Melinex[®] was removed slowly to not create air bubbles;
- (5) Step (1), (2), (3) and (4) were repeated for each layer.

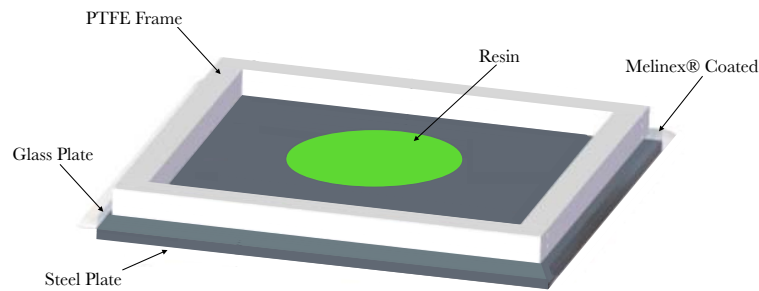


Figure 5.4: Initial set-up of the apparatus required for the Wet/Hand Lay-Up manufacturing method including the pooling of resin^[28].

LAYUP SEQUENCE			
START from the BOTTOM			
Top	16	[0/90]	NF
INSERT	15	[90/0]	F
	14	[0/90]	NF
	13	[90/0]	F
	12	[0/90]	NF
	11	[90/0]	F
	10	[0/90]	NF
	9	[90/0]	F
	8	[0/90]	NF
	7	[90/0]	F
	6	[0/90]	NF
	5	[90/0]	F
	4	[0/90]	NF
	3	[90/0]	F
	2	[0/90]	NF
BOTTOM	1	[90/0]	F

NF

F

Table 5.1: Lay-Up sequence for the specimens.

Further instructions:

- the resin, every single time after being poured, was put again into the oven, furthermore, the two beakers were used alternatively;
- the sheet of Melinex[®] Uncoated was changed every 4 plies.

After the deposition of the 15th ply, the PTFE inserts must be placed, in particular, the centre of each disk must be positioned on the 15th ply's marks previously made. Special attention should be given to the pouring of the resin. The resin is poured away from the inserts so that they do not change their position. The specific steps performed to include the PTFE inserts are shown in the following Figure 5.5.

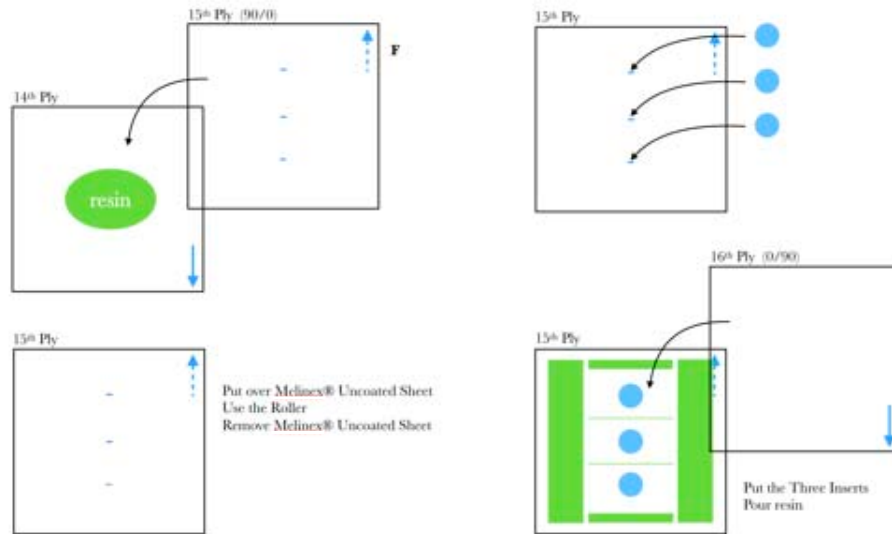


Figure 5.5: Operations for positioning the PTFE inserts.

After those particular steps, the previous sequence was repeated, steps (1) to (4), to lay the last ply. When all plies were put, a sheet of Melinex[®] Coated was laid, and, over that it was placed the smaller glass plate to close the mould. These final operations conclude the Hand Lay-UP.

5.1.3 Degassing and Curing of the Laminate

The degassing of the laminate was obtained through a vacuum chamber. After positioning the second steel plate inside the chamber, the laminate along with its mould was placed on top of the new hot basement. With the help of a vacuum pump, the pressure in the well-sealed chamber was reduced to negative 1 *bar* for 1 hour.

The laminate, without the top glass plate, was placed on the work table. Due to a large number of bubbles of air trapped in the resin, it was necessary to employ a rounded spatula to push those towards the edges of the laminate. This operation took 15 minutes and must be carried out gently and slowly in order to avoid trapping the bubbles within the panel.

At this stage, the laminate along with its mould was placed in the Curing Oven. Then, a pressure of approximately 12 *kPa* was applied on the

laminated from a large metal plate clamped to the top of the laminate with additional weights placed on the top (the total weight is 219,8 *lbs*). Then, the laminate was cured for 3 hours once the oven reached 100 °C. The oven was set up to increase the internal heat at a rate of 1.0 °C per minute from room temperature (approximately 80 ÷ 90 minutes). The relatively slow heating rate allowed the epoxy matrix to fully infuse the fabrics.

The laminate was taken out after the oven returned to room temperature. The mould was then removed through the following steps:

- the top glass plate;
- the top sheet of Melinex[®] Coated;
- the frame and the bottom sheet of Melinex[®] Coated;
- the bottom glass plate.

Finally, the panel between the glass plates, which were both cleaned and waxed again, was put inside the Post-Curing Oven for 3 hours until it reached a temperature of 150 °C (approximately 40 minutes, the temperature was raised at a rate of 3.0 °C per minute).

Exactly after the time required to avoid the degradation of the properties, the laminate was removed and gently cleaned.

The manufacturing of the panel is completed, and it is possible to proceed to cut the specimens.

5.2 Cutting the Flat Panel to make Specimens

The product panel presents a huge quantitative of irregularities that have to be eliminated. So, it was used an electric Wet Saw, with which is possible to obtain a completely flat laminate, for trimming those defects. Whereas, to have the specimens it was used the COMPCUT[®] 200 - Composite Saw. The COMPCUT[®] 200 is a CNC machine with an electroplated diamond abrasive blade.

The coupons (Figure 5.7) has a length of 200 *mm*, a width of 70 *mm* and the same thickness of the flat panel, 4 *mm*. So, the hypothetical cutting scheme of the panel in three flat coupons is shown in Figure 5.6.

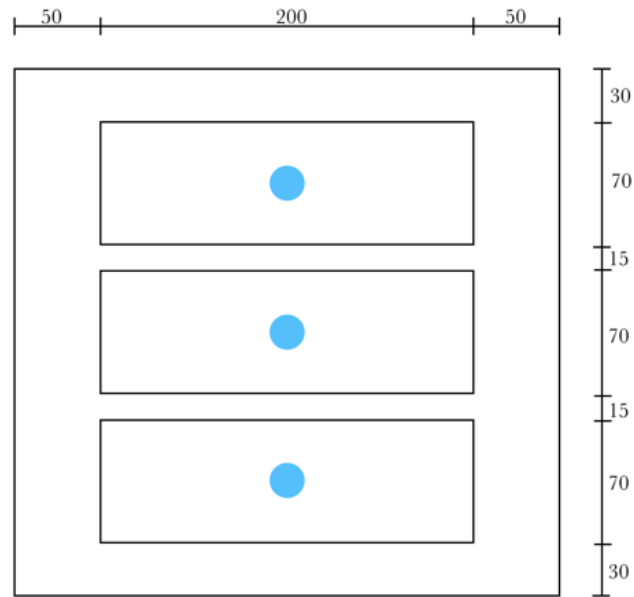


Figure 5.6: Cutting scheme for making the coupons.

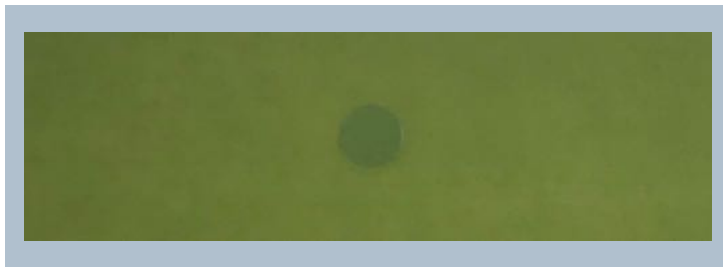


Figure 5.7: Example of a specimen with 10 *mm* radius PTFE insert.

Then, each specimen is drilled (Figure 5.8) at the centre of the PTFE insert in order to release the vacuum created between the insert and the adjoining plies.

Attention: this operation took place after applying the speckle pattern (see Paragraph 7.3) to ensure that it does not obstruct the hole.

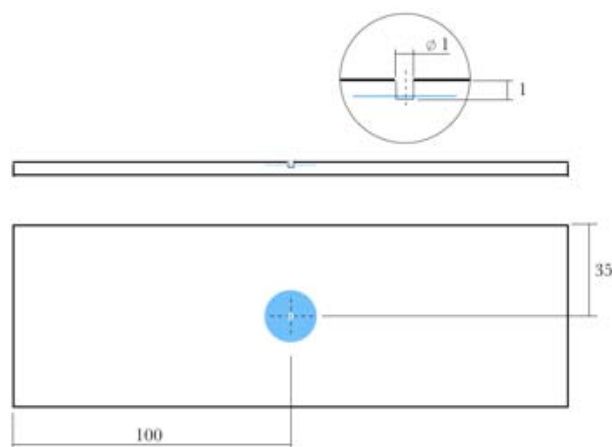


Figure 5.8: Drilling hole scheme.

5.3 Summary of Test Specimens

Table 5.2 shows the types of the specimens used in this work; all the coupons were realised following the process outlined above, so they are identical in terms of Lay-Up and Size, but different as regards the De-lamination Insert. In particular, for the specimens with Elliptical Insert, the insert in two coupons was positioned with the major axis parallel to the width of the specimen, and in the other two along the length. Instead, for the specimens with the Double Circular Insert, it was decided to manufacture a type with the first insert ($\phi = 20 \text{ mm}$) between the 1st and 2nd ply and the second insert ($\phi = 40 \text{ mm}$) between the 3rd and 4th ply, while for the other type the inserts have been inverted during the deposition. Finally, three samples have been made without any type of defect.

Specimens		
Type of Test	Defect Type	Number of Specimens
4 - PB	None	3
	Circular PTFE Insert ($\phi = 20 \text{ mm}$)	3
	Circular PTFE Insert ($\phi = 40 \text{ mm}$)	3
	Elliptical PTFE Insert (a = 20, b = 40 mm)	2
	Elliptical PTFE Insert (a = 40, b = 20 mm)	2
	Double Circular PTFE Insert ($\phi = 20$ and $\phi = 40 \text{ mm}$)	2
	Double Circular PTFE Insert ($\phi = 40$ and $\phi = 20 \text{ mm}$)	1

Table 5.2: Summary of test specimens used for non-destructive testing.

A substantial number of specimens was made, to ensure statistical significance to the results.

Chapter 6

Mechanical Testing

All the specimens investigated in this work were mechanically loaded quasi-statically. In the quasi-static loading, the load depends on the time, but, since it is applied with a speed so low as to basically deform the structure in a static manner, the inertial effects are neglected. So, the small loading rate allows to correctly monitor the strain of the sample being tested; in particular it is possible to detect with the DIC technique the growth of delamination between the PTFE insert and the adjacent plies. At last, thanks to limited nominal loads, the development of further damage mechanisms is also avoided.

The mechanical loading used in this work is:

- Four - Point Bending Flexural Test (see Paragraph 6.1).

6.1 Four - Point Bending Test

In this work for carrying out the Four - Point Bending Testing the guidelines indicated by the standard method ASTM D7264/D7264M were followed. The Four - Point Bend Test is shown in the schematic diagram in Figure 6.1, with the support rollers placed 160 *mm* apart, and the loading rollers with a span of 80 *mm*. The rollers shall have a cylindrical contact surface of 5.00 *mm* radius and shall have finely polished surfaces. Furthermore, the loading noses and supports have to touch the specimen evenly across its width to avoid a non-uniformly loading.

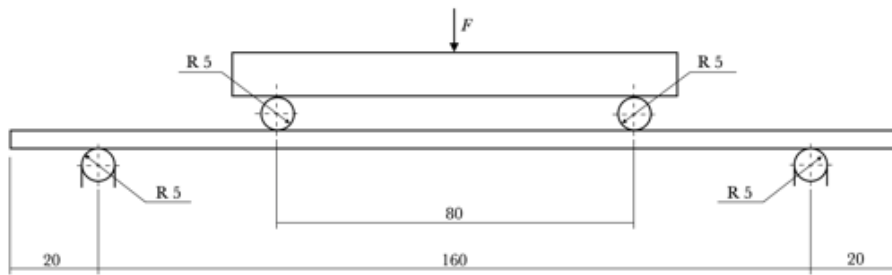


Figure 6.1: Four - Point Loading configuration with rolling supports and rolling loading noses.

Therefore, the real apparatus with which the test is performed is shown in Figure 6.2. The support block and loading block were bolted to the machine basement and crosshead respectively to ensure that they did not change their relative position during testing. And so, after accurately positioning the specimen, having the span to thickness ratio of 40 : 1, it was performed the test by setting the descent rate of the cross-head equal to $1.0 \text{ mm}/\text{min}$. The test was interrupted, and so concluded, when a load of 3.5 kN was reached, that corresponds to the deformation of Figure 6.2 (b).



(a) Four - Point Bending before loading



(b) Four - Point Bending after loading

Figure 6.2: Four - Point Bend specimen Set-Up inside Instron[®] 5982 testing rig.

Chapter 7

Digital Image Correlation (3D-DIC)

The DIC is the NDT Technique that was used in this work to detect the deformations on the surface of the specimens under loading in order to assess the Delamination's growth from the PTFE insert between the first two plies. For all the tested specimens was used a standard 3D stereo DIC system consisting of two 9.2 Megapixel Allied Vision Technology Manta cameras, containing a 2/3" chip, with LINOS MeVis-C 1.6/35 lenses supplied by *Correlated Solutions*. Together with the equipment came the software for setting up and calibrating the cameras (*VIC-Snap*[®]), and the one for post-processing the acquired images (*VIC-3D*[®]).

This non-contact measurement solution requires:

- the camera system Set-Up (see Paragraph 7.1);
- the cameras Calibration (see Paragraph 7.2);
- the Speckling of the surface of specimens (see Paragraph 7.3);
- the images Collecting and Processing (see Paragraph 7.4);
- the Post-Processing of the acquired DIC images during testing (see Part IV).

7.1 Experimental Arrangement

After connecting the system for image acquisition and fixing the specimen to the test machine, the cameras and light source were placed. Their positioning depends on the sample geometry, type of test, and environment. The cameras must be positioned far enough away to allow a wide shot, with a high resolution, of the entire surface of the specimen tested. Therefore, finding the correct frontal distance is essential as the cameras and lenses supplied are independent; in fact, they are not equipped of built in optical zoom. Instead, the light source is usually positioned sideways or over the sample in order to prevent the light beams reflected by the specimen from saturating the cameras. In addition, it is necessary for the cameras to be centred on the sample and to do that the *Crosshairs* function, included in *VIC-Snap*[®], through which the centre of each camera is displayed on the screen, is used. The cameras, then, are adjusted in height by setting their support, and horizontally by moving them equally from the centre of their bracket maintaining a tilt angle with respect to the sample not exceeding $10 \div 15$ degrees. Once these operations were completed, the Aperture, Focus and Exposure Time of the two cameras have been set by using *VIC-Snap*[®] according to the following steps:

- (1) the Aperture of each camera was completely opened;
- (2) the Exposure Time was adjusted by reducing the frame rate until all the saturation on the images disappears;
- (3) the function *Sigma Estimate* was launched on both images for assessing the quality of the speckle pattern;
- (4) the Focus on both cameras was adjusted until the images turn into blue/purple (the colours of the rainbow scale used to evaluate the *Sigma Estimate* which guarantee a good outcome);
- (5) the function *Sigma Estimate* was shut down;
- (6) the Aperture of each camera was closed approximately halfway;
- (7) the Exposure Time was adjusted again by increasing the frame rate to the saturation's threshold (the limit beyond which the images begin to turn red);
- (8) the function *Sigma Estimate* was rechecked by adjusting the Focus (as in Step 4).

Thus, the images were focused and the Aperture and Exposure Time were balanced so that to allow the proper amount of light to enter into the cameras.

7.1.1 Four - Point Bending Test

Even though the DIC technique with a double set of cameras allows the simultaneous monitoring of both surfaces of the specimens during the tests, in this work, only the compression surface was investigated.

Figure 7.1 shows the Set-Up for obtaining data from the Four - Point Bending Test. The cameras and the light-sources were pointed at the central area of the sample which was defined respectively by the upper loading rollers.

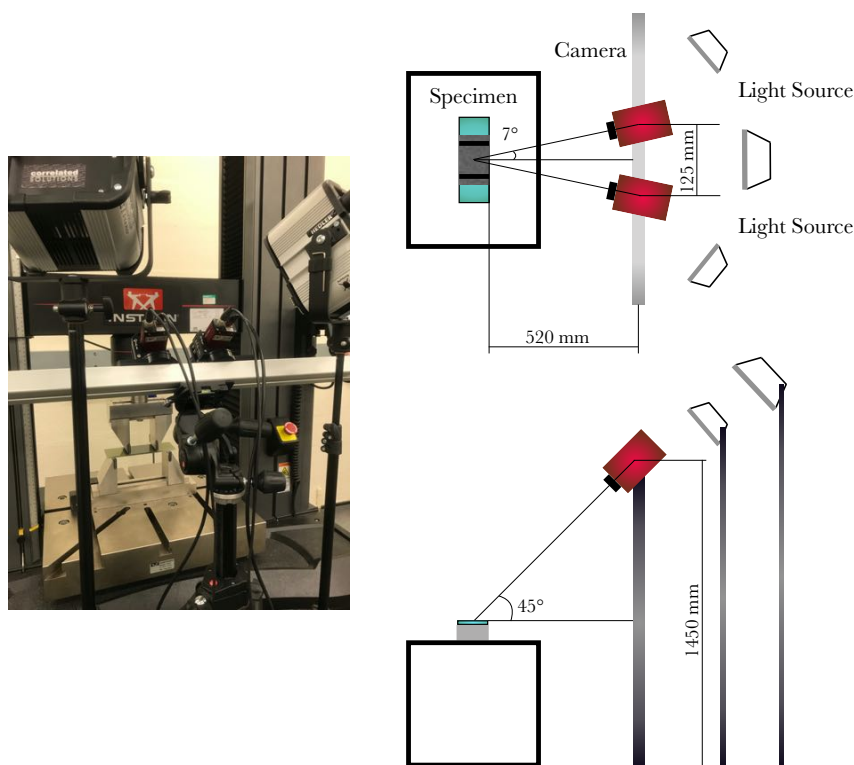


Figure 7.1: DIC Set-Up scheme with Instron[®] machine to obtain Four - Point Bending results for the compressive side of the specimen.

7.2 Calibration

After the Set-Up of the DIC system, the cameras have to be calibrated. For the system to acquire data, the software must match the images from both cameras. In order to do so, using *VIC-Snap[®] - Calibration Mode*, a minimum of 30 images of a 2D Calibration board (Figure 7.2) held in

multiple positions and angles were acquired simultaneously from both cameras. The positions and angles of the board have to be as varied as possible to ensure the best mapping of the area of interest. As shown in Figure 7.2 the grids have a predefined distance between each dot. The calibration software (*VIC-3D*[®]) matches these dots to define an origin, and matches the focal planes for each camera to calibrate them. In particular, the function *Calibrate Stereo System* provides a feedback on the quality of the calibration: the calibration score. The score is based on the distance between the predicted grid point locations and the actual grid point locations in each image. The calibration score should be less than 0.03. If the required score is not obtained, it is possible to improve it by increasing the *Distortion Order* which takes account into the lenses' curvature, and by deleting the images with a score higher than 0.05 from the calibration images.

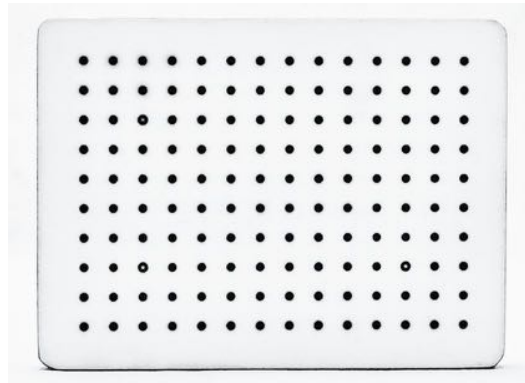


Figure 7.2: Example of 10 mm Calibration board supplied by *Correlated Solutions*.

7.3 Speckle Pattern

To ensure that DIC's measurements are accurate, a random speckle pattern needs to be applied to the surface of the specimens. In coupons the speckle pattern can be made by first spraying a matt white layer as a base and, once it dried, a matt black acrylic paint aerosol can be used to create spots (Figure 7.3); as an alternative to black spray it is possible to use an ink roller (Figure 7.4). It is necessary that the applied pattern has a good white - black contrast, and that the black spots have an optimal size^[20]; actually, there must be approximately $10 \div 20$ speckles for each Subset. However, if the resulting pattern has predominantly black areas, or too large speckles, the painting process has to be done again.



Figure 7.3: Speckle pattern applied using aerosol cans on a finished specimen.

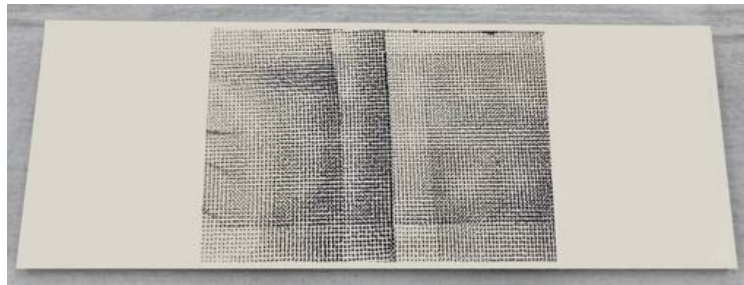


Figure 7.4: Speckle pattern applied using an ink roller kit with 0.013" dot size supplied by *Correlated Solutions* on a finished specimen.


After trying numerous alternatives, it was decided that the best results were obtained by using an adhesive film with a printed speckle pattern (Figure 7.5).



Figure 7.5: Speckle pattern applied using a film on a finished specimen with the underside painted in matt white.

A calculation scheme, shown in Table 7.1, was implemented for the creation of the speckle pattern to be printed on the films. The scheme generates a pattern capable of complying with the guidelines proposed by Pan^[24] (see Paragraph 3.3.3), which ensure the best results.

INPUT			
Specimen's ROI			
Height	100	[mm]	
Width	70	[mm]	
Camera's Resolution			
Horizontal	3384	[pixel]	
Vertical	2710	[pixel]	
Sheet's Dimension			
Height	297	[mm]	
Width	210	[mm]	
Speckle Diameter Required			
Chosen	5	[pixel]	
	9	[pixel]	
	14	[pixel]	



Preliminary Calculations			
Calculation of pixel per mm			
Horizontal Resolution	Height ROI	33.840	
Vertical Resolution	Width ROI	38.714	
Minimum		33.840	
Pattern Diameter Calculation			
Speckle Diameter	Minimum pixel/mm	0.148	[mm]

Pattern Density Calculation			
Pattern Area	$\pi * \left(\frac{\text{Pattern Diameter}}{2}\right)^2$	0.017	[mm ²]
Sheet Area		62370	[mm ²]
Speckles Needed Total	$\frac{1}{2} * \frac{\text{Sheet Area}}{\text{Pattern Area}}$	181870	
Columns	$\frac{\text{Height}}{\text{Width}} * \sqrt{\text{Speckles Needed Total}}$	1907	
Rows	$\frac{\text{Width}}{\text{Height}} * \sqrt{\text{Speckles Needed Total}}$	954	
Height	$\frac{\text{Columns}}{\text{Pattern Diameter}}$	281.816	[mm] 94.9 [%]
Width	$\frac{\text{Rows}}{\text{Pattern Diameter}}$	149.893	[mm] 67.1 [%]
Pattern Density	Minimum between Height and Width	67.1	[%]

OUTPUT			
Generation of Speckle Pattern			
Pattern Diameter	0.148	[mm]	
Pattern Density	67.1	[%]	
Pattern Variation	90.0	[%]	
Geometry Height	297	[mm]	
Geometry Width	210	[mm]	




Table 7.1: Flow Chart and Output for the creation of the Speckle Pattern for the Four - Point Bend Specimen.

7.4 Collecting and Processing

The images during the test were automatically acquired by using the *Time Collecting* function of *VIC-Snap*[®], set at a 3-seconds interval between shots. The Calibration images and the newly collected images were opened with *VIC-3D*[®] to be processed. The processing was then taken on via the following steps:

- (1) the ROI, region of interest, was selected using the *Polygon* command;
- (2) the Subset size and Step size were chosen;
- (3) a Seed Point, a characteristic point, for instance, a bigger speckle dot, was marked on the ROI;
- (4) the *Green Arrow* command was clicked and executed up to 100%;
- (5) the Strain was calculated opening *Data Drop*, *Processing Tools* and *Calculate Strain*.

So, once the Strain was obtained, it is possible to assess e.g. Displacement X, Y and Z or Deformation ε_{xx} , ε_{yy} and ε_{xy} .

In case the calculated strain is noisy, fluctuations can be reduced by applying a strain filter defined as the area where the strain is averaged. In this project, it was used a strain filter equal to 11 for most of the time, that was able to provide a good compromise between the resolution of the strain, higher with a smaller strain filter, and the accuracy, better with a larger strain filter. Thus, the total area over which the strain was measured is $10 * 11 = 110$ pixels.

Part IV
Monitoring

Chapter 8

Preliminary Research: Assessment of the DIC Technique

This chapter presents the work done to verify the capabilities of the DIC as an NDT Technique in measuring deformation and detecting delaminations.

8.1 Examination of the DIC Technique as a tool for deformation analysis

A beam subjected to Four - Point Bending is characterised by a constant bending moment between the load application points (Figure 8.1). This means that the deformation is also constant.

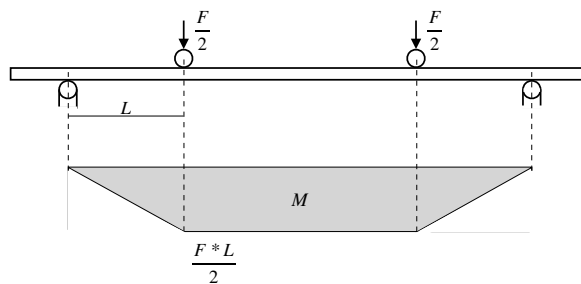


Figure 8.1: Bending Moment Diagram of a Four - Point Bending Beam.

Therefore, to verify the reliability of the DIC Technique it is necessary that a uniform deformation field is obtained for the Region Of Interest. The ε_{xx} field, measured using the DIC, of a specimen without PTFE insert is shown in Figure 8.2.

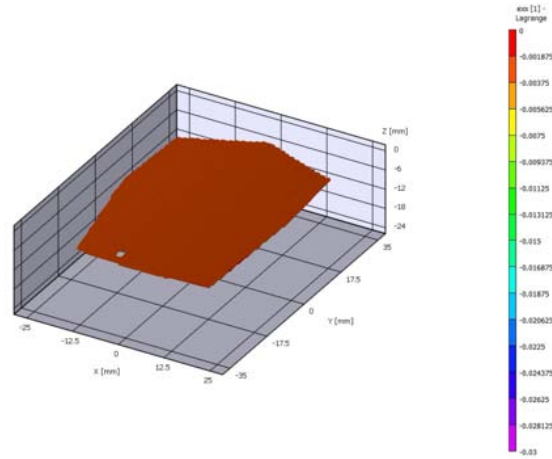


Figure 8.2: DIC Strain contours of a specimen without delamination insert under load of 1000 N.

The figure shows that in the area enclosed between the loading supports the field is almost constant, but each band of the ε_{xx} scale is constituted by a range of values. Further verification is carried out to establish the accuracy of the measurements and establish the noise level. Thus, with the strain values measured along the reference line defined as shown in Figure 8.3, the variability of the deformation is evaluated.

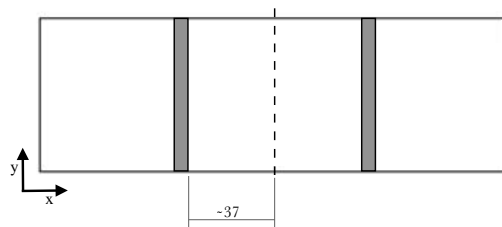


Figure 8.3: Schematic drawing of the line along which the data for Strain measurement are extracted.

The study also requires the comparison of the strain values obtained at the various load levels for different sets of characteristic parameters of the DIC, i.e. different Subset, Step Size and Filter Size.

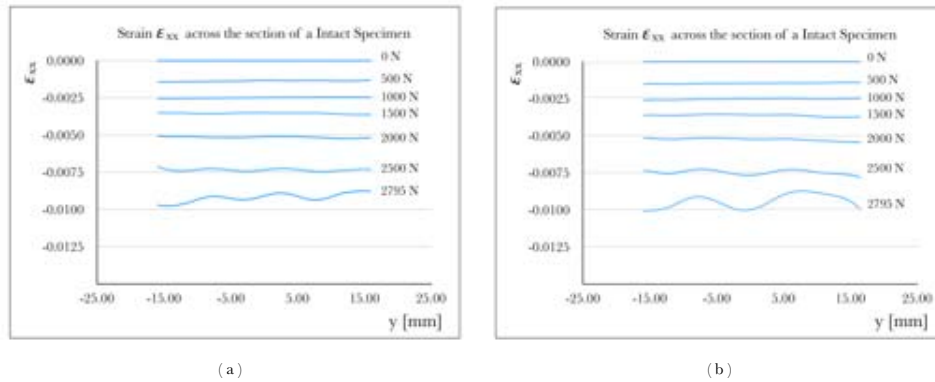


Figure 8.4: Comparison of the DIC Strain profile along the reference line (see Figure 8.3) for different analysis parameters: (a) Subset 27, Step Size 9, Filter Size 13; (b) Subset 33, Step Size 10, Filter Size 11.

From the comparison of Figure 8.4 (a) and (b), it can be seen that better accuracy is obtained in the determination of the strain values using the analysis parameters of (a). Compared to the resulting data of the other configuration, there is a deviation from the average value of the strain next to nihil, except for high loads. However, even for the latter, the deviation is lower than that of (b). This is because with the configuration of (a) a more accurate measurement is performed as the number of the calculation points is increased.

As a result of the above analysis, it can, therefore, be concluded that DIC is a valid NDT Technique for the assessment of the strain field of a composite structural element.

8.2 Assessment of the DIC Technique as a tool for detecting delaminations

From what has been proposed in the literature (see Part II), the DIC can detect the defects, in particular the delaminations, which affect the tested structural elements by considering their influence on the superficial strain trend. As seen in the previous Section 8.1, a non-delaminated specimen subjected to Four - Point Bending has a constant deformation for the load-case. Instead, that is not true for a specimen having a delamination insert. Figure 8.5 shows the strain profile of the latter, highlighting the edge of the delamination insert with a dashed line.

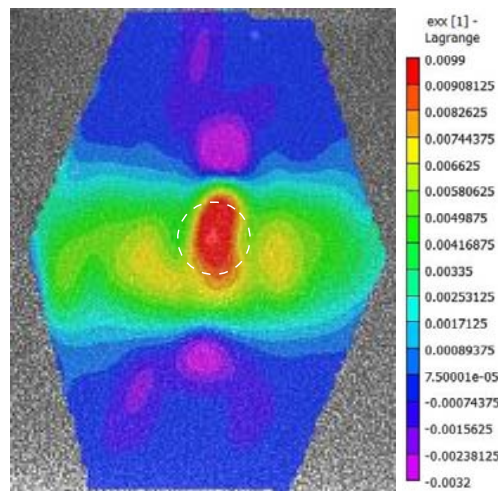


Figure 8.5: DIC Strain contours of a specimen with an embedded circular delamination one-ply below the surface under an applied force of 2795 N . The dashed circle indicates the location of the delamination insert.

The presence of delamination is visible from the irregularities in the strain contours. If it is compared with what was obtained in the previous Section 8.1 (Figure 8.2), the difference is substantial: there is stress concentration at the peak of the defect.

Then, using the data collected along the reference line of Figure 8.3, it is possible to plot the strain profile development as the load varies during the test, for a specimen with $\phi = 20 \text{ mm}$ delamination insert the evolution is shown in Figure 8.6.

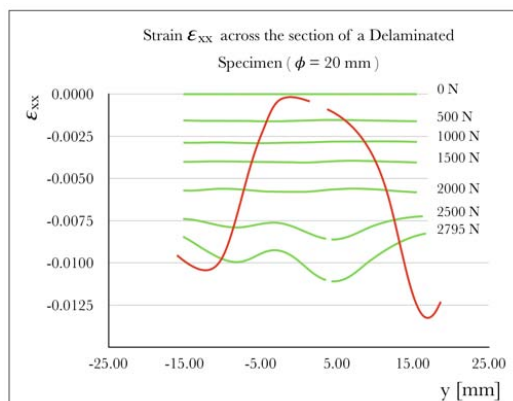


Figure 8.6: DIC Strain profiles of the specimen with $\phi = 20 \text{ mm}$ delamination insert during testing. In red the Displacement profiles after the Pop-Up.

It is possible to use the measurement of the out-of-plane displacement to evaluate the delamination behaviour. In particular, through these measurements the evolution of the characteristic bulge of the delaminated layer is determined, since the sample has gone into a localised buckling.

To evaluate the displacement the data collected along the reference line of Figure 8.7 are analysed.

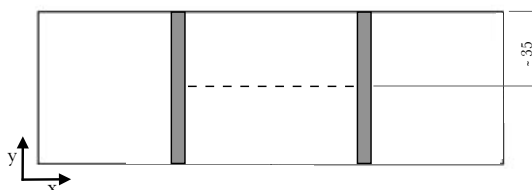


Figure 8.7: Schematic drawing of the line along which the data for Displacement measurement are extracted.

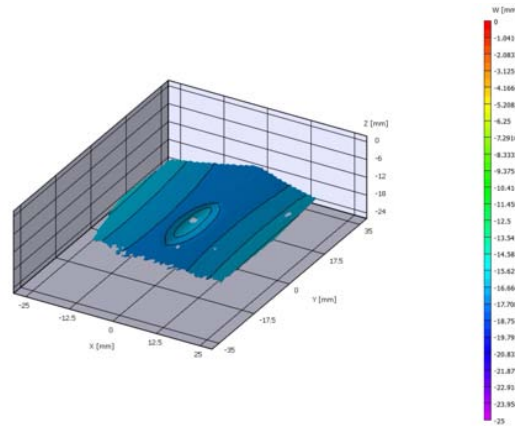


Figure 8.8: DIC Displacement contours of a specimen with an embedded circular delamination one-ply below the surface under an applied force of 2795 N .

After obtaining the data for the different instant of the test, the displacement trend is obtained. In particular, in the following Figure 8.9 is shown the trend related to a sample having a $\phi = 20 \text{ mm}$ insert.

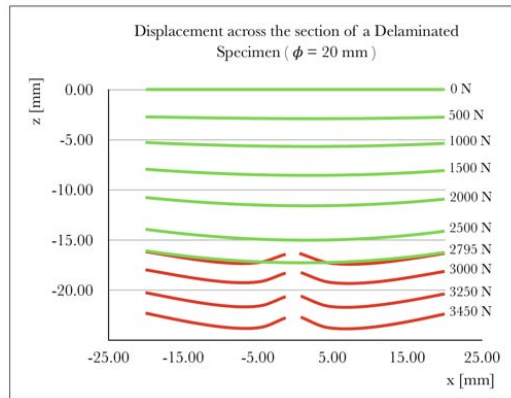


Figure 8.9: DIC Displacement profiles of the specimen with $\phi = 20 \text{ mm}$ delamination insert. In red the Displacement after the Pop-Up.

8.3 Summary: Comparison between specimens with and without a delamination insert

For the sake of completeness, the typical values of specimens with and without a delamination insert are now presented in summary form. What has obtained is now compared starting from the Load / Extension diagram relating to the tests performed.

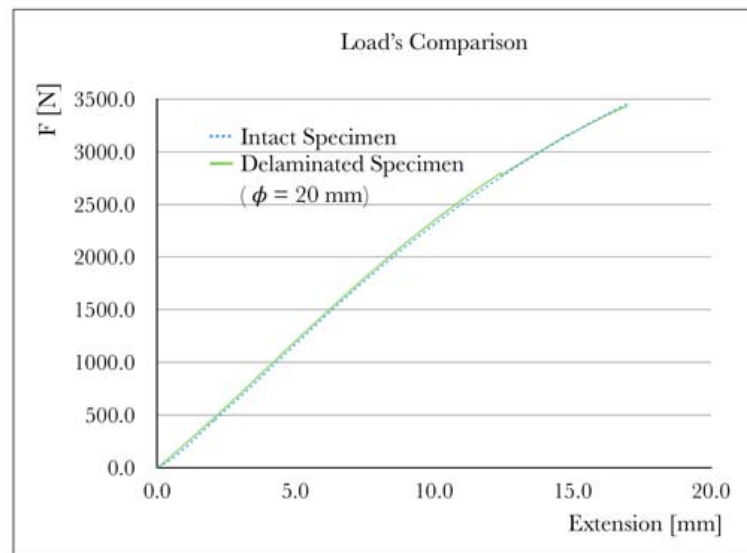


Figure 8.10: Comparison of the Load/Extension diagram of a specimen without artificial delamination with that of one with a circular ($\phi = 20$ mm) delamination insert.

From the diagram (Figure 8.10) it can be seen that the trend is approximately identical; the curve relative to the specimen having delamination has higher inclination, but this is due exclusively to the fact that during the realisation of the samples it was not possible to obtain the same thickness in both. It is important to pay particular attention to the fact that in the characteristic curve of the delaminated sample at the instant in which the detachment of the layer occurs above the delamination insert there is a drop, an immediate reduction of the stiffness of the sample. This is reflected in the strain's curve by directly comparing the profiles for the two samples: the delaminated sample presents a completely different profile when the Pop-Up occurs (Figure 8.11).

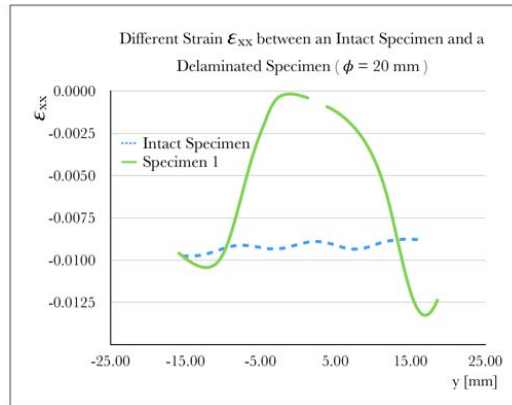


Figure 8.11: Comparison of the Strain profile calculated with DIC along the reference line for the sample without artificial delamination and that with a $\phi = 20 \text{ mm}$ delamination insert.

Similarly, with regard to the out-of-plane displacement, there is a marked difference in the trend (Figure 8.12). In fact, the profile of the delaminated samples has a bulge in correspondence of the delaminated area.

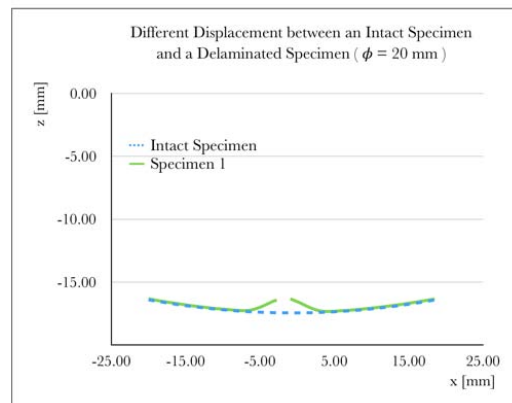


Figure 8.12: Comparison of the Displacement between the sample without artificial delamination with that having it.

These differences are due to the fact that the specimen without delamination does not present localised buckling, and therefore it does not show the detachment of the upper layer due to the delamination.

Chapter 9

Monitoring of Delamination Growth in the Specimens with a Single Delamination Insert

Given that the purpose of this work is to study the method to be adopted to quantify the size of the delamination, in this chapter the procedure is presented and the results obtained for specimens with single delamination insert are shown. The insert in those samples, during the manufacturing, was placed only one-ply below the surface of interest. This was done to ensure that the delamination had the maximum effect on the specimen surface strain, minimising the effect of experimental noise on the resolution.

9.1 Analysis Procedure

The analysis procedure implemented for each series of samples grouped according to the geometry of the insert used to reproduce delamination is now presented.

9.1.1 Starting Results

Initially, the average thickness of each sample is determined, then the load profiles for each type of sample are compared.

The thickness of the sample is the result of a series of measurements carried out with a digital caliper, having a resolution of 0.01 *mm*, in specific detection points shown in Figure 9.1.

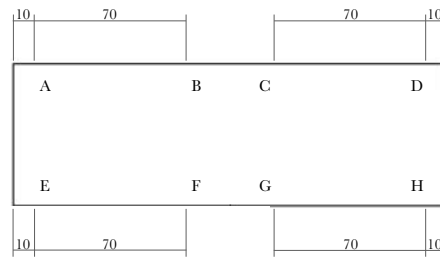


Figure 9.1: Schematic drawing of the points in which the data for the thickness of specimens are measured.

The evaluation of the samples' thickness is used to verify the correctness of the differences that may emerge from the comparison between the load profiles, in particular with regard to their slope.

9.1.2 Method for measuring the Delamination Size

For the evaluation of delamination growth, the deformation and the out-of-plane displacement field were used. The adopted technique involved the placing of markers at the points of the profiles where the values deviated from those relating to no-defect-insert specimen. Then, the distance between the markers was measured for establishing the delamination size. An example of the measurement method is shown in Figure 9.2.

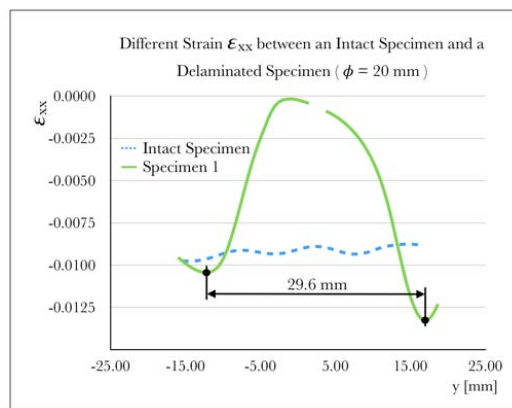


Figure 9.2: Example of the measurement method for determining the delamination size.

The delamination size has been assessed in two different instants: the first at the time of the Pop-Up and the second at the End of the test. This was done to understand the growth of the defect.

To verify whether the values obtained through the DIC were truthful, at the end of each test, further images of the samples were acquired. From those images, the size of the real defect was measured by a *pixel-mm* correlation. To do this the *ImageJ*[®] software was used. The measurement was carried out as follows: firstly, the *pixel-mm* scale of the image was set by measuring in *pixel* the extension of the ruler placed as a reference near the sample during the images acquisition; and, secondly, the extent of the delamination was measured. To obtain the value in *mm*, the software exploits the following correlation:

$$\text{Delamination Size in } mm = \frac{\text{Ruler in } mm * \text{Delamination Size in } pixel}{\text{Ruler Dimension in } pixel}$$

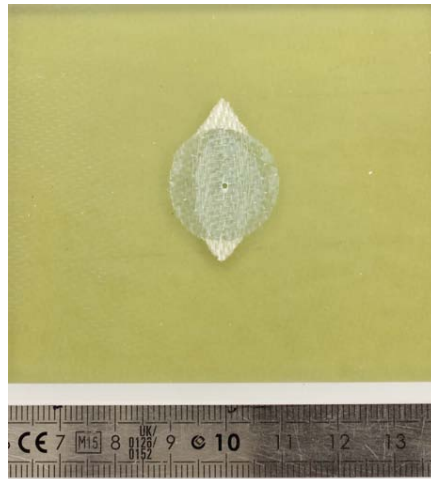


Figure 9.3: Example of acquired image for measuring, through *pixel-mm* correlation, the delamination size to check the values obtained with DIC analysis.

To determine the *pixel-mm* conversion ratio, the part of the ruler between 9.5 to 10.5 *cm* was measured, which means that a line of 10 *mm* was evaluated in *pixel*. This conversion factor was determined for each image analysed.

9.1.3 Method for determining the Bulge Area

Lastly, the area related to the Bulge caused by the local buckling effect that occurred on the top layer above the insert was investigated. To evaluate the truly delaminated area, the data of the out-of-plane displacement profiles ($z - x$ and $z - y$) obtained along the reference lines shown in Figure 9.4, were analysed.

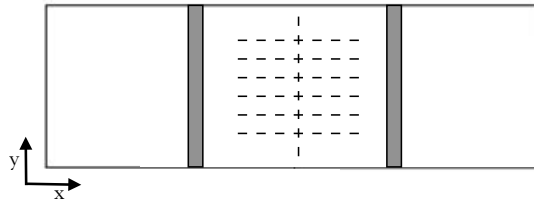


Figure 9.4: Schematic drawing of the lines along which the point pairs are extracted from $z - x$ and $z - y$ displacement.

From the inflection points of the displacement curves, identified with the same procedure previously exposed (Figure 9.2), the point pairs $(x; y)$ for the determination of the approximate geometry of the delaminated area were obtained. The value of the area was calculated using the *Polyarea* function, included in *MATLAB*[®].

Also for this analysis, the values of the point pairs were determined at different times to understand the evolution of the delaminated area.

To verify whether the values obtained through the DIC were truthful, the real defect area outside the PTFE Insert was measured by a *pixel-mm* correlation from the images acquired at the end of the tests. To do this the *ImageJ*[®] software was used again.

9.2 Specimens with Circular Delamination Insert ($\phi = 20 \text{ mm}$)

Three samples have been tested for this type of insert. Their load profiles are shown in Figure 9.5.

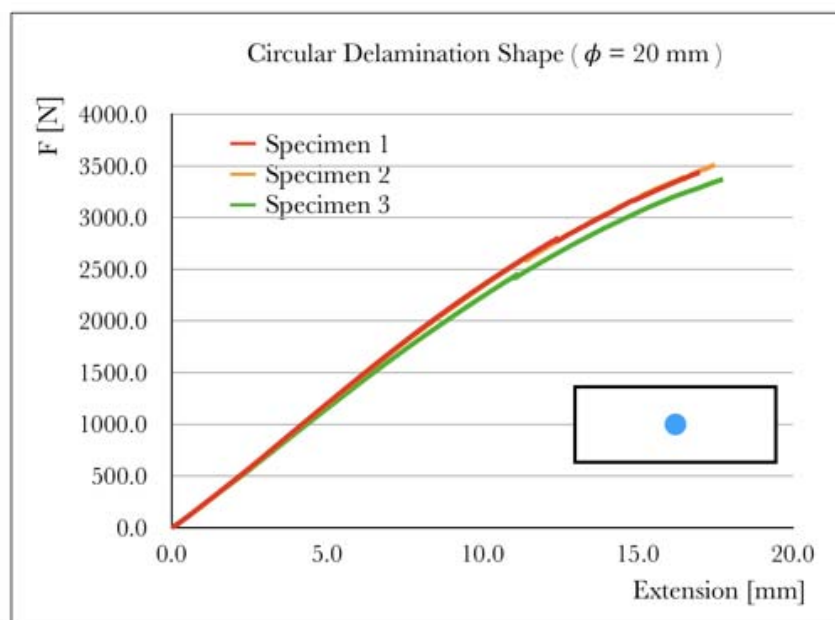


Figure 9.5: Repeatability Load/Extension diagram for specimens with Circular $\phi = 20 \text{ mm}$ insert.

The different slope of the load profiles is due to the fact that the specimens differ from each other in terms of thickness; actually, they have a thickness of 4.32 ± 0.05 , 4.30 ± 0.04 , and $4.18 \pm 0.06 \text{ mm}$ respectively.

Delamination Size

The longitudinal strains along the transverse data paths suggested defect widths of 29.4 mm and 31.4 mm respectively at the time of Pop-Up and at the End of the test. Instead, 29.0 mm and 30.8 mm were obtained with the out-of-plane displacement along the data line.

Size of Delamination along Y using ϵ_{xx}		
	After Pop-Up [mm]	End [mm]
Specimen 1	29.6	31.6
Specimen 2	29.2	31.8
Specimen 3	28.4	30.9
Average	29.1	31.4
Standard Deviation	0.6	0.5

Table 9.1: Values of the Delamination main Size for samples with $\phi = 20$ mm insert calculated with DIC Strain.

Size of Delamination along Y using Displacement		
	After Pop-Up [mm]	End [mm]
Specimen 1	29.1	31.0
Specimen 2	29.4	31.2
Specimen 3	28.5	30.1
Average	29.0	30.8
Standard Deviation	0.5	0.6

Table 9.2: Values of the Delamination main Size for samples with $\phi = 20$ mm insert calculated with DIC Displacement.

The values obtained from the strain and displacement profiles differ from each other, in particular, those resulting from the analysis of the deformation field are higher. However, both provide overestimated results, since the accurate value of the delamination at the End of the test, measured with the *pixel-mm* correlation, is 29.3 ± 0.2 mm. Therefore, an error of 7.2% and 5.1% was made with the strain and displacement data.

Bulge Area

Concerning the values for the Bulge Area, in the following Table 9.3 the calculated area at the time of the Pop-Up of the top layer and at the End of the test are shown.

As can be seen from Table 9.3, there is a decrease of the Bulge Area, but the real growth of the delamination along its transverse direction is clear from Figure 1, Figure 2 and Figure 3 (see Appendices: A.2).

Area of the Bulge using Displacement		
	After Pop-Up [mm ²]	End [mm ²]
Specimen 1	228.7	229.9
Specimen 2	236.7	234.3
Specimen 3	224.6	219.4
Average	230.0	227.9
Standard Deviation	6.2	7.7

Table 9.3: Values of the Bulge Area for specimens with $\phi = 20 \text{ mm}$ insert.

9.3 Specimens with Circular Delamination Insert ($\phi = 40 \text{ mm}$)

Three samples have been tested for this type of insert. Their load profiles are shown in Figure 9.6.

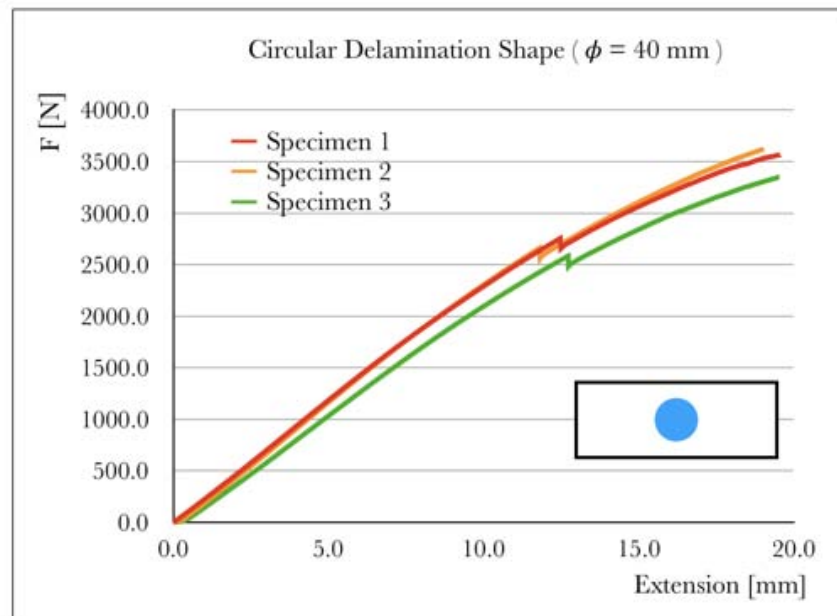


Figure 9.6: Repeatability Load/Extension diagram for specimens with Circular $\phi = 40 \text{ mm}$ insert.

The specimens have a thickness of 4.31 ± 0.03 , 4.28 ± 0.04 , and $4.21 \pm 0.05 \text{ mm}$ respectively. The load profiles of the first and the second sample are nearly the same, given the near equality of their thicknesses, while the

profile of the third specimen differs from the others by being less thick and by presenting manufacturing defects (voids-bubbles).

Delamination Size

The longitudinal strains along the transverse data paths suggested defect widths of 52.6 mm and 54.3 mm respectively at the time of Pop-Up and at the End of the test. Instead, 52.0 mm and 54.5 mm were obtained with the out-of-plane displacement along the data line.

Size of Delamination along Y using ϵ_{xx}		
	After Pop-Up [mm]	End [mm]
Specimen 1	53.4	54.3
Specimen 2	50.9	54.1
Specimen 3	53.6	54.6
Average	52.6	54.3
Standard Deviation	1.5	0.3

Table 9.4: Values of the Delamination main Size for samples with $\phi = 40$ mm insert calculated with DIC Strain.

Size of Delamination along Y using Displacement		
	After Pop-Up [mm]	End [mm]
Specimen 1	52.4	55.0
Specimen 2	50.2	53.7
Specimen 3	53.4	54.8
Average	52.0	54.5
Standard Deviation	1.6	0.7

Table 9.5: Values of the Delamination main Size for samples with $\phi = 40$ mm insert calculated with DIC Displacement.

The accurate value of the delamination at the End of the test, measured with the *pixel-mm* correlation, is 53.0 ± 0.5 mm. So, an error of 2.4% and 2.8% was made with the strain and displacement data.

Bulge Area

As regards the values for the Bulge Area, in the following Table 9.6 the calculated area at the time of the Pop-Up of the top layer and at the End of the test are shown.

Area of the Bulge using Displacement		
	After Pop-Up [mm ²]	End [mm ²]
Specimen 1	580.8	583.9
Specimen 2	584.6	563.6
Specimen 3	588.1	582.8
Average	584.5	576.8
Standard Deviation	3.7	11.4

Table 9.6: Values of the Bulge Area for specimens with $\phi = 40 \text{ mm}$ insert.

Although a decrease of the Bulge Area can be seen from Table 9.6, the real growth of the delamination along its transverse direction is clear from Figure 4, Figure 5 and Figure 6 (see Appendices: A.2).

9.4 Specimens with Elliptical Horizontal Delamination Insert

Only two specimens with this type of insert were tested. In the samples, the elliptical insert was placed with the major axis parallel to the length of the sample. The load profiles of the specimens are shown in Figure 9.7.

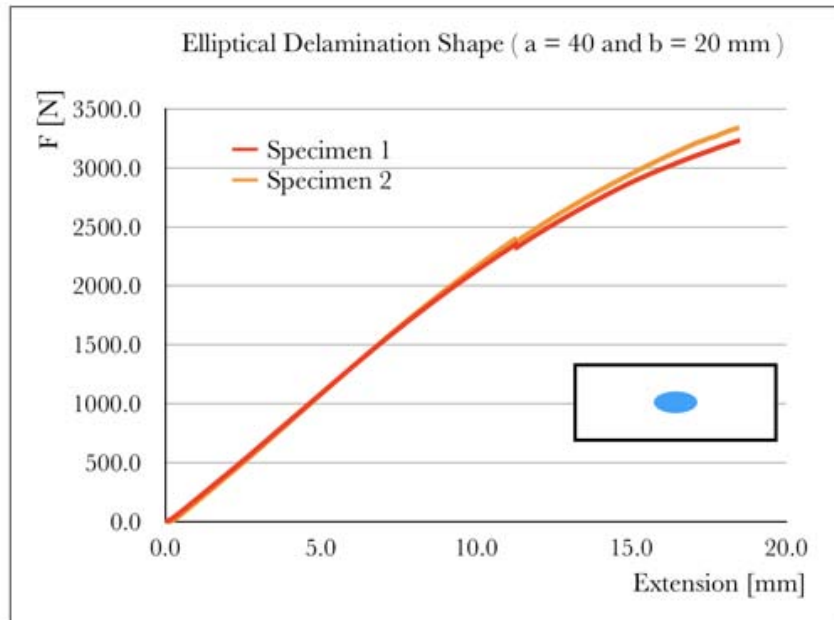


Figure 9.7: Repeatability Load/Extension diagram for specimens with Elliptical Horizontal insert.

The first specimen has a thickness of 4.11 ± 0.02 mm, instead, the other has 4.12 ± 0.04 mm. The load profiles are approximately the same, given the near equality of the thicknesses of the samples.

Delamination Size

The longitudinal strains along the transverse data paths suggested defect widths of 26.6 mm and 31.3 mm respectively at the time of Pop-Up and at the End of the test. Instead, 30.6 mm and 31.5 mm were obtained with the out-of-plane displacement along the data line.

Size of Delamination along Y using ϵ_{xx}		
	After Pop-Up [mm]	End [mm]
Specimen 1	26.7	31.6
Specimen 2	26.5	30.9
Average	26.6	31.3
Standard Deviation	0.1	0.5

Table 9.7: Values of the Delamination main Size for samples with Elliptical Horizontal insert calculated with DIC Strain.

Size of Delamination along Y using Displacement		
	After Pop-Up [mm]	End [mm]
Specimen 1	30.7	31.7
Specimen 2	30.5	31.3
Average	30.6	31.5
Standard Deviation	0.1	0.3

Table 9.8: Values of the Delamination main Size for samples with Elliptical Horizontal insert calculated with DIC Displacement.

The accurate value of the delamination at the End of the test, measured with the *pixel-mm* correlation, is $30.1 \pm 0.8 \text{ mm}$. So, an error of 4.0% and 4.6% was made with the strain and displacement data.

Bulge Area

As regards the values for the Bulge Area, in the following Table 9.9 the calculated area at the time of the Pop-Up of the top layer and at the End of the test are shown.

Although a decrease of the Bulge Area can be seen from Table 9.9, the real growth of the delamination along its transverse direction is clear from Figure 7 and Figure 8 (see Appendices: A.2).

Area of the Bulge using Displacement		
	After Pop-Up [mm ²]	End [mm ²]
Specimen 1	236.6	235.0
Specimen 2	224.8	221.8
Average	230.7	228.4
Standard Deviation	8.3	9.3

Table 9.9: Values of the Bulge Area for specimens with Elliptical Horizontal insert.

9.5 Specimens with Elliptical Vertical Delamination Insert

Only two specimens with this type of insert were tested. In the samples, the elliptical insert was placed with the major axis parallel to the width of the sample. The load profiles of the specimens are shown in Figure 9.8.

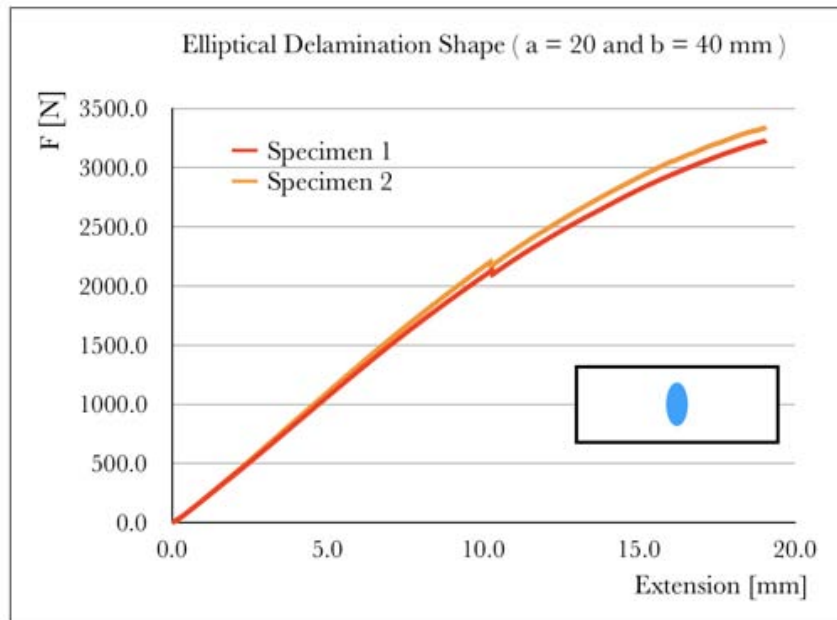


Figure 9.8: Repeatability Load/Extension diagram for specimens with Elliptical Vertical insert.

The first specimen has a thickness of 4.06 ± 0.03 mm, instead, the other has 4.11 ± 0.03 mm. The load profiles differ due to the difference in the

thickness of the samples.

Delamination Size

The longitudinal strains along the transverse data paths suggested defect widths of 47.3 mm and 49.7 mm respectively at the time of Pop-Up and at the End of the test. Instead, 46.7 mm and 49.9 mm were obtained with the out-of-plane displacement along the data line.

Size of Delamination along Y using ϵ_{xx}		
	After Pop-Up [mm]	End [mm]
Specimen 1	47.4	49.6
Specimen 2	47.1	49.8
Average	47.3	49.7
Standard Deviation	0.2	0.1

Table 9.10: Values of the Delamination main Size for samples with Elliptical Vertical insert calculated with DIC Strain.

Size of Delamination along Y using Displacement		
	After Pop-Up [mm]	End [mm]
Specimen 1	46.4	49.6
Specimen 2	46.9	50.1
Average	46.7	49.9
Standard Deviation	0.4	0.4

Table 9.11: Values of the Delamination main Size for samples with Elliptical Vertical insert calculated with DIC Displacement.

The accurate value of the delamination at the End of the test, measured with the *pixel-mm* correlation, is $47.9 \pm 0.4 \text{ mm}$. So, an error of 3.8% and 4.2% was made with the strain and displacement data.

Bulge Area

As regards the values for the Bulge Area, in the following Table 9.12 the calculated area at the time of the Pop-Up of the top layer and at the End of the test are shown.

Area of the Bulge using Displacement		
	After Pop-Up [mm ²]	End [mm ²]
Specimen 1	542.0	506.3
Specimen 2	536.9	516.5
Average	539.5	511.4
Standard Deviation	3.6	7.2

Table 9.12: Values of the Bulge Area for specimens with Elliptical Vertical insert.

Although a decrease of the Bulge Area can be seen from Table 9.12, the real growth of the delamination along its transverse direction is clear from Figure 9 and Figure 10 (see Appendices: A.2).

Chapter 10

Monitoring of Delamination Growth in the Specimens with Double Delamination Insert

The analysis of the load data of the tests was conducted in a similar way to that performed for samples with a Single Delamination Insert. While, as regards the analysis of data collected via DIC Technique, the investigation was exclusively focused on the strain profiles. Starting from those profiles the investigation determined the transverse extension of the delamination. The values determined by the DIC data were as far as possible, also in this case, compared with the measurements of the delamination carried out using the *ImageJ*[®] software on the images acquired at the end of the tests.

10.1 Specimens with $\phi_1 = 20 \text{ mm}$ and $\phi_2 = 40 \text{ mm}$ insert

Only two specimens with this type of insert were tested. The load profiles of the specimens are shown in Figure 10.1.

The first specimen has a thickness of $4.00 \pm 0.05 \text{ mm}$, instead, the other has $4.08 \pm 0.04 \text{ mm}$, so it is for this difference in thickness that the load profiles are not identical.

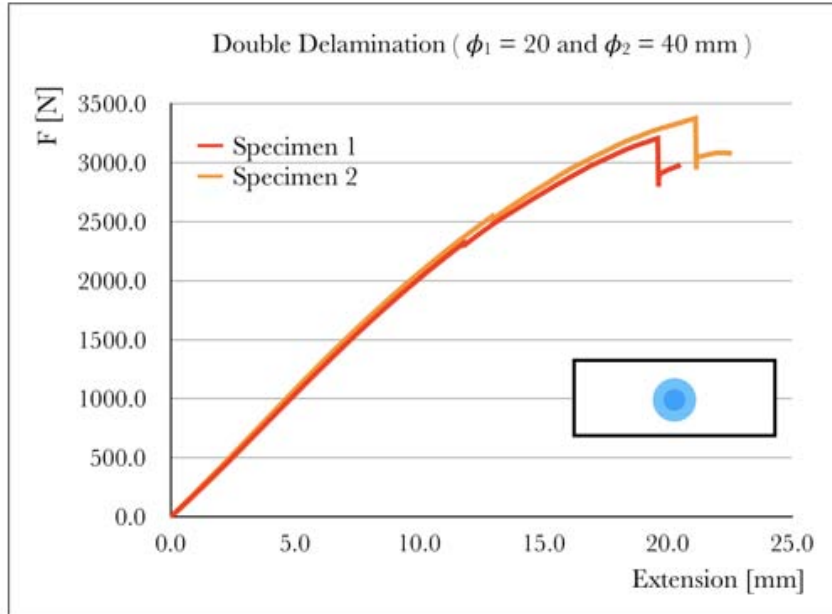


Figure 10.1: Repeatability Load/Extension diagram for specimens with Double Circular Delamination insert with the smallest above.

The load profiles of these samples are characterised by two different drops, this is due to the fact that the specimens have two delamination inserts.

Delamination Size

For the determination of the delamination size the method previously proposed in Section 9.1.2 was used, taking into consideration only the strain profiles and ignoring the out-of-plane displacement profiles.

From the investigation via DIC, the strain profiles shown in Figure 10.2 were obtained. There are two completely different strain patterns. At the time of the first Pop-Up, the green profile in Figure 10.2, the delamination on the upper layer above the insert with $\phi_1 = 20$ mm begins. While, at the time of the second Pop-Up there is the growth of delamination due to the other insert placed deeper in the sample. At the time of the 2nd Pop-Up, there is a consistent loss of data at the delamination front, as can be seen from the red profile of Figure 10.2, but despite that it is nevertheless possible to hypothesise the trend of the strain, being symmetrical with respect to the centre by analogy with the green profile. The red profile shows that the delamination due to the second insert ($\phi_2 = 40$ mm) is much greater than the first delamination.

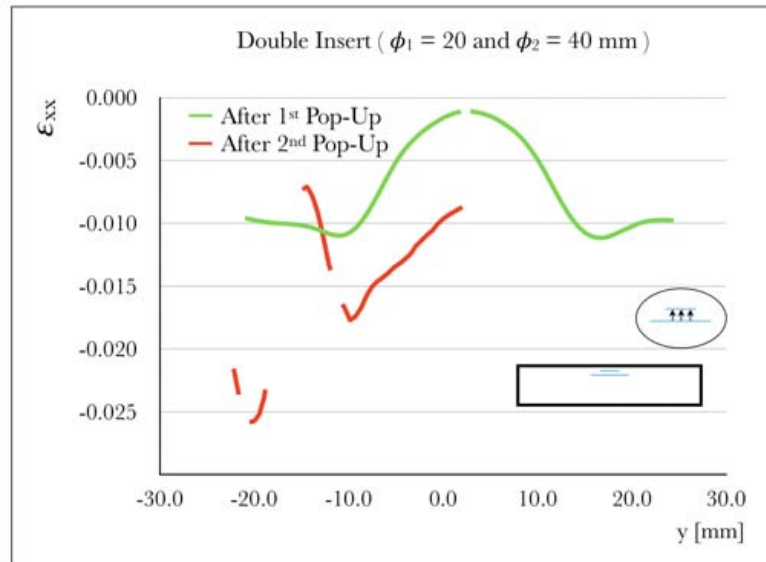


Figure 10.2: DIC Strain profile at the moment of the 1st and 2nd Pop-Up in the specimen with Double Delamination insert with the smallest above.

From the data obtained via the DIC, it was possible to determine only the size of the delamination at the time of the 1st Pop-Up, while it was not possible to determine for Specimen 1 the value of the delamination at the time of the 2nd Pop-Up, and for neither sample it was possible to determine the value of the delamination at the End of the test (Table 10.1).

Size of Delamination along Y using ϵ_{xx}			
	After 1st Pop-Up [mm]	After 2nd Pop-Up [mm]	End [mm]
Specimen 1	29.0	nn	nn
Specimen 2	29.1	55.3	nn
Average	29.1	55.3	
Standard Deviation	0.1		

Table 10.1: Values of the Delamination main Size for samples with Double Circular insert, the smallest above, calculated with DIC Strain.

The delamination value at the end of the test was measured exclusively with the *pixel-mm* correlation and it was equal to 55.9 *mm* for the first sample and 65.4 *mm* for the other.

With the DIC it was possible to evaluate the size of the delamination at the time of the first Pop-Up, which is during the test. By contrast, this technique proved to be useless when the data on the front of the delamination were limited. Therefore, if an excessive loss of information occurs, it is necessary to use an optical measurement technique via *pixel-mm* correlation for determining the size of the delamination.

Bulge Area investigations were not conducted for those samples.

10.2 Specimens with $\phi_1 = 40 \text{ mm}$ and $\phi_2 = 20 \text{ mm}$ inserts

Only a specimen with this type of insert has been tested. The load profile of the specimen having a thickness of $4.01 \pm 0.06 \text{ mm}$ is shown in Figure 10.3.

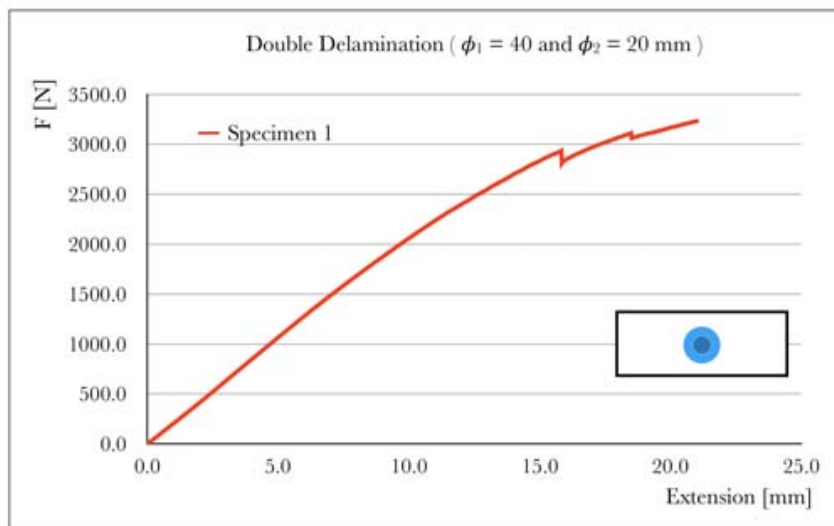


Figure 10.3: Repeatability Load/Extension diagram for specimens with Double Circular Delamination insert with the biggest above.

The load profile is characterised by two different drops.

Delamination Size

From the investigation via DIC, the strain profiles shown in Figure 10.4 were obtained. The strain patterns are almost the same. In the red one, the only difference is due to the growth of the delamination.

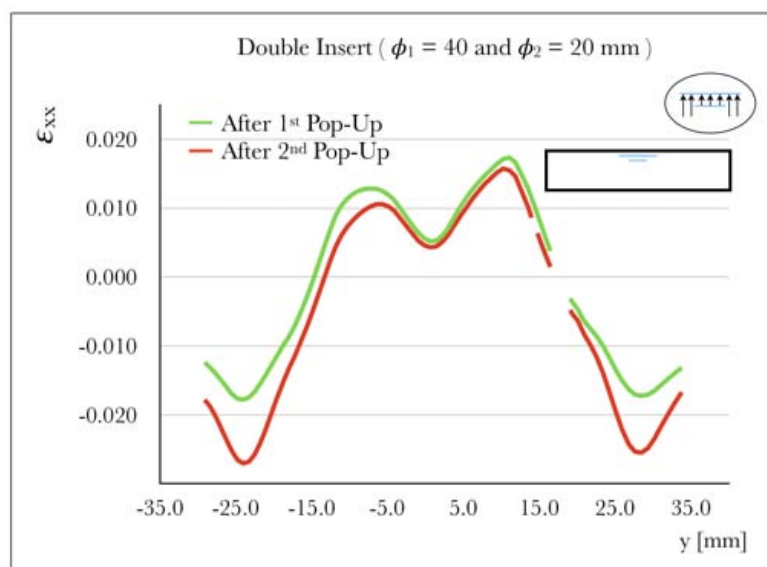


Figure 10.4: DIC Strain profile at the moment of the 1st and 2nd Pop-Up in the specimen with Double Delamination insert with the biggest above.

From the data obtained via the DIC, it was possible to determine the size of the delamination at the 1st and 2nd Pop-Up, and at the End of the test.

Size of Delamination along Y using ϵ_{xx}			
	After 1st Pop-Up [mm]	After 2nd Pop-Up [mm]	End [mm]
Specimen 1	53.7	54.2	55.6

Table 10.2: Values of the Delamination main Size for sample with Double Circular insert, the biggest above, calculated with DIC Strain.

The accurate value of the delamination at the End of the test, measured with the *pixel-mm* correlation, is 54.0 mm. So, an error of 3.0% was made with the strain data.

Chapter 11

Finite Element Analysis of Specimens

This chapter proposes a viable strategy for the finite element modelling of what was investigated experimentally in this work. Firstly, the modelling and simulation of the Four - Point Bending Test of a sample without a delamination insert is reported. Secondly, the tests relating to the specimens with an embedded delamination are reported. All the numerical simulations were performed using the commercial software *Abaqus CAE* of *Dassault Systèmes*[®].

11.1 Numerical Model of the Four - Point Bending Test on a specimen without delamination insert

To simulate numerically the experimental tests carried out with the testing machine suitably set following the standard method ASTM D7264 / D7264M, both the load and support rollers and the specimen were modelled (Figure 11.1). For the cylindrical rollers (radius of the base 5.0 mm and height 70.0 mm) *3D Deformable Shell* elements were used, instead for the specimen (200.0 mm long, 70.0 mm wide and 4.2 mm thick) a single *3D Deformable Solid* element was used.

After reproducing the sample geometrically, its elastic properties (Table 11.1) and the stacking sequence $[(0/90)/(90/0)]_{4S}$ were assigned to it. So, such characteristics have been inserted in *Mechanical Elastic Property* in *Lamina*; whereas, the stacking of the layers that make up the sample was imported by using the *Composite Layup Manager* command, again in the *Property Module*. In particular, *Continuum Shell* was selected as the *Element Type* of the *Composite Layup*. Finally, the *Element Relative Thickness* (0.2625 mm) and the *Rotation Angle* were set for each ply.

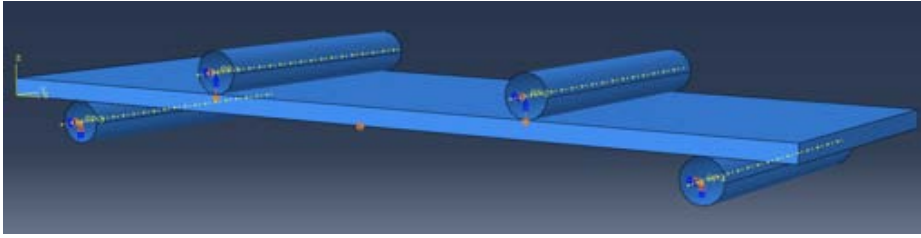


Figure 11.1: The numerical geometry of Four - Point Bending Test with the Boundary Conditions.

$E_1 = E_2$	ν_{12}
21000 [MPa]	0.2
G_{12}	$G_{13} = G_{23}$
4200 [MPa]	3500 [MPa]

Table 11.1: Material properties of 8-HS Glass Woven / Epoxy laminate.

The rollers were modelled by using 144 S4R elements, which are four-node doubly curved thin shells; by contrast the specimen was modelled by using 900 SC8R elements, which are eight-node quadrilateral in-plane general-purpose continuum shells.

The Four - Point Bending Test carried out in displacement control was simulated by setting the following *Boundary Conditions*:

- *Encastre* for the support rollers;
- a negative translation ($z = -1 \text{ mm} / \text{min}$ to replicate the controlled descent of the machine cross-head) for the loading rollers.

In addition, the boundary conditions that impose rigid movement to the body were applied directly to the central section of the sample.

Then, after simulating the test, it was possible to extract the trend of the Force on the Displacement, which can be compared with the corresponding curve generated directly by the testing machine, as shown in the following Figure 11.2.

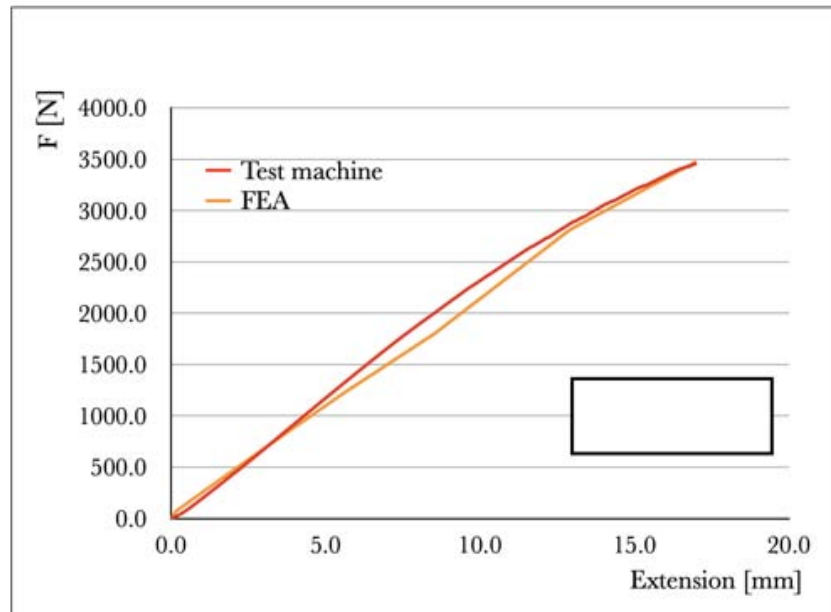


Figure 11.2: Comparison between the Load/Extension curve generated by the Instron[®] 5982 test machine with that generated by the numerical simulation with *Abaqus CAE*.

From the previous graph it can be seen that there is a good correspondence between what has been obtained by numerical simulation and experimentally. Accordingly, it can be assumed that the model implemented is good for simulating the test.

11.2 Numerical Model of the Four - Point Bending Test on a specimen with a delamination insert

The Four - Point Bending Test was again modelled; but this time, differently from the model previously implemented, the delamination artificially inserted into the samples during manufacturing was also modelled. So, a three-dimensional cohesive element was used to simulate the delamination, by implementing the Cohesive Zone Model (CZM)^{[36][48]}. The specimen was divided into three parts (Figure 11.3):

- the Sub-Laminate Layer, which is the part of the specimen above the delamination insert (only the 1st ply);
- the Cohesive Interface Layer, which is the interface zone, populated

with cohesive elements^[46], that joins the Sub-Laminate Layer and the Base Layer;

- the Base Layer, which is the part of the specimen below the delamination insert (the remaining fifteen plies).

The Cohesive Interface Layer has a hole, with which the delamination insert is reproduced. Because there is no continuity of the material at the hole, the detachment between the layers which occurs as a result of delamination is replicated. However, in order to prevent overlap or interpenetration between the Sub-Laminate and the Base was introduced a *Surface-to-Surface Contact Constraint* in the delamination zone^{[36][46]}.

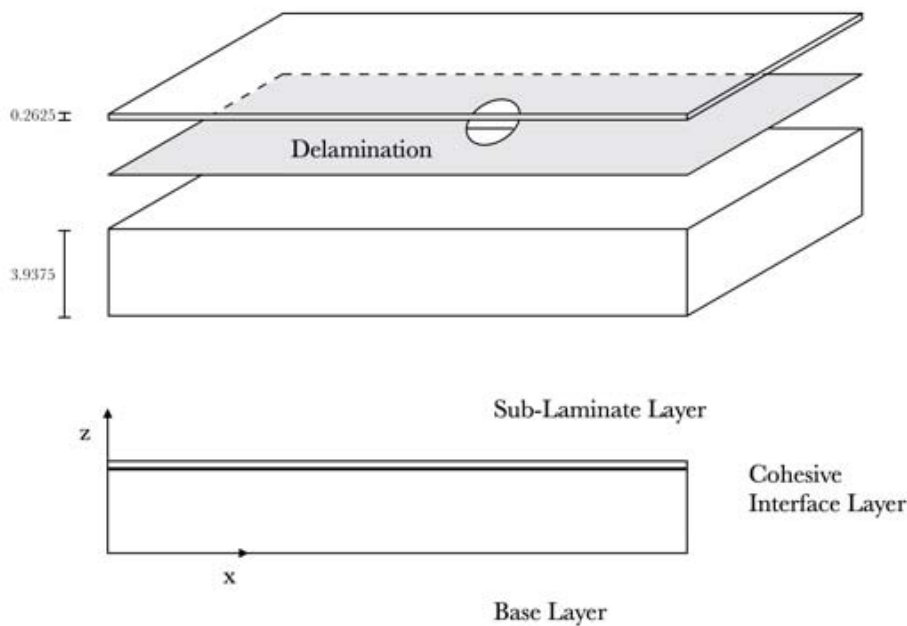


Figure 11.3: Schematic of the Finite Element Model, showing an exploded view of the Sub-Laminate Layer, the Cohesive Interface Layer and the Base Layer^{[36][46]}.

As an alternative to modelling delaminations using the CZM approach, the Virtual Crack Closure Technique (VCCT) can be used^[44].

11.2.1 Cohesive Zone Modelling (CZM)

In order to model the delamination and its behaviour with the cohesive elements, several aspects has to be taken into account. Firstly, the behaviour of the cohesive elements themselves must be described and a

traction - separation law is used to do this. In *Abaqus*, the modelling of that law requires multiple input parameters, since it describes the initial elastic linear behaviour, the initiation and evolution of the damage (Figure 11.4).

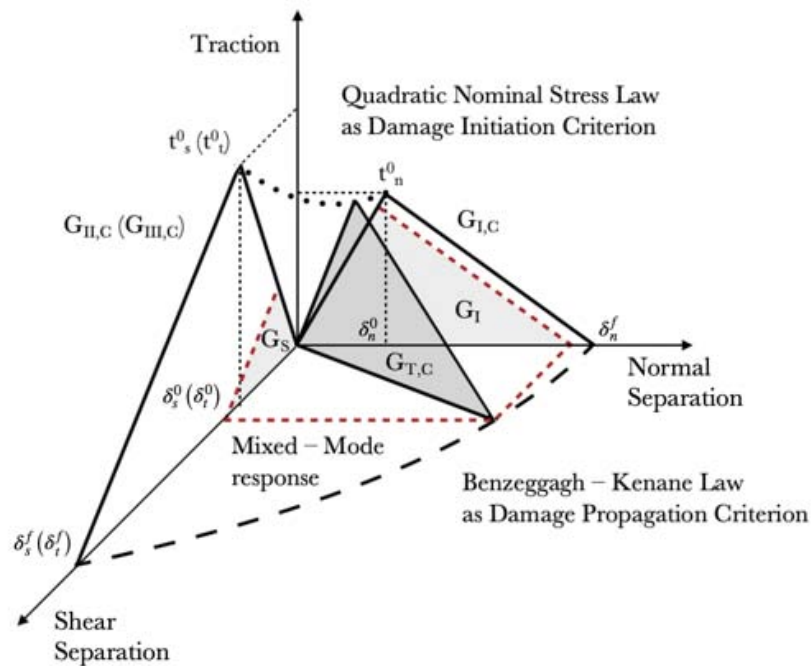


Figure 11.4: Schematic representation of the Traction - Separation Law.

Linear Elastic Behaviour

The elastic behaviour is described by a stress - strain curve, $\mathbf{t} = \mathbf{E} * \boldsymbol{\varepsilon}$ where the elastic matrix $[\mathbf{E}]$ relates the nominal stresses to the nominal deformations across the interface. In particular, as specified in the guide *Defining the constitutive response of cohesive elements using a traction - separation description* supplied by MIT.edu, the nominal stress are the force components divided by the original area at each integration point, while the nominal strains are the separations divided by the original thickness at each integration point. The constituent parameters of the elastic matrix must be appropriately inserted so that the cohesive elements have an interface stiffness that guarantees a good bond between the parts before the damage.

The Penalty Stiffness values adopted in the simulation are reported in the Table 11.2.

Damage Initiation Criterion

Because the growth of delamination is likely to occur following a mixed-mode loading, then the stiffness degradation of the structure occurs before the nominal stresses involved reach their respective maximum value; so, in order to predict the damage initiation, as the Maximum Stress Criterion cannot be adopted, the Quadratic Failure Criterion (QUADS) must be used^[43]. The law of the QUADS Criterion is shown below:

$$\left(\frac{t_n}{t_n^0}\right) + \left(\frac{t_s}{t_s^0}\right) + \left(\frac{t_t}{t_t^0}\right) = 1 \quad (11.1)$$

where t_n represents the nominal traction stress in pure mode I, t_s and t_t represent the nominal shear stress along the first (mode II) and the second (mode III) shear directions, respectively, t_n^0 , t_s^0 and t_t^0 are the corresponding ultimate strength^[36], whose values, for the case-study, are reported in Table 11.2.

The criterion does not take into account the normal compression stresses as they do not affect the onset of delaminations^[43].

Damage Propagation Criterion

After the first damage event, the delamination can grow; a criterion based on the Fracture Energy can be adopted in order to predict its evolution^[46]. The Benzeggagh - Kenane law can be used, whereby the delamination growth occurs when the combination of the components of the Energy Release Rate is equal to the critical value G_{TC} ^[45]. The Benzeggagh - Kenane is shown below:

$$G_{TC} = G_{IC} + (G_{IIc} - G_{IC}) \left(\frac{G_{II} + G_{III}}{G_I + G_{II} + G_{III}} \right)^\eta \quad (11.2)$$

where η is an empirical parameter derived from mixed-mode tests, G_{IC} , G_{IIc} and G_{IIIc} are the critical energy release rates for modes I, II and III, respectively (Table 11.2), and G_I , G_{II} and G_{III} are the corresponding values determined from analysis^[46]. In order to obtain the critical energy release rates values, it is necessary to conduct the characterisation of the interlaminar fracture strength of the material, by using the Double Cantilever Beam (DCB) specimens for mode I, the End-Notched Flexure (ENF) test specimens for mode II and the Mixed-Mode Bending (MMB) test specimens for the mixed-modes I and II^[43].

$E_{nn} = E_{ss} = E_{tt}$	t_n^0	$t_s^0 = t_t^0$
8550 [N/mm ³]	35 [MPa]	65 [MPa]
$G_{I,C}$	$G_{II,C} = G_{III,C}$	η
0.5 [N/mm]	1.8 [N/mm]	2.284

Table 11.2: Mechanical properties of Interface^[47].

11.2.2 Simulation Results

The results obtained for samples with a Single Circular Delamination Insert ($\phi = 20 \text{ mm}$) are shown below; in particular, Specimen 3 was replicated. Only this specimen was modelled in this work.

Given the axial symmetry in y of the sample and the load, only half of the specimen and a single pair of rollers were modelled. To assign the characteristic properties of the materials to the components, the steps proposed in the previous Paragraph 11.1 were followed. While, as regards the mesh, S4R elements were used for the rollers, SC8R elements for the Base Layer and the Sub-Laminate Layer, and COH3D8 elements for the Cohesive Interface Layer. In order to obtain accurate results for the cohesive zone, the distance between the delamination edge and the point where the maximum cohesive traction is reached^[45] must be properly discretised. Therefore, it is necessary to create an adequate mesh for that zone (Figure 11.5).

In the simulation of the load test, a displacement $z = -17.75 \text{ mm}$ was imposed on the load rollers so as to replicate the final value of the descent of the load cross-head of the test machine for Specimen 3 tested. After setting the calculation software parameters, the deformation of the specimen, and the growth of the delamination were obtained (Figures 11.6 and 11.7).

Good correspondence of the values of the delamination size at the End of the test was obtained between the results generated by the simulation in *Abaqus* and those deriving from the DIC analysis. This is shown in Figure 11.8, where the comparison of the out-of-plane displacement profile of the Bulge for the simulation and for the DIC analysis is carried out. In particular, for Specimen 3 a delamination size equal to 28.3 *mm* was obtained with the simulation and a delamination size of 30.1 *mm* with the DIC analysis. If the value obtained from the simulation is compared to the value obtained with the *pixel-mm* correlation (29.1 *mm*) the match is almost identical.

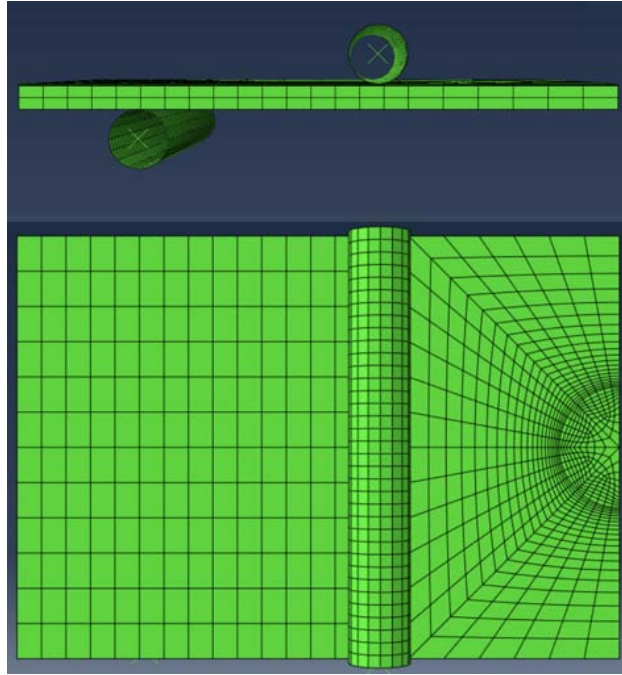


Figure 11.5: Side View and Top View of the specimen highlighting the Mesh pattern.

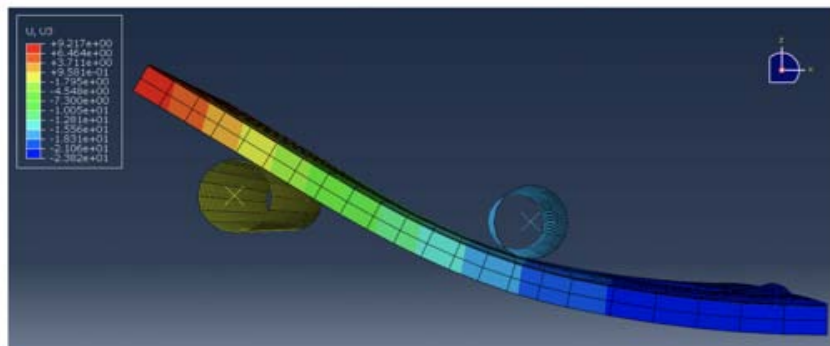


Figure 11.6: Final deformation of the sample for a displacement of the load roller $z = -17.75 \text{ mm}$.

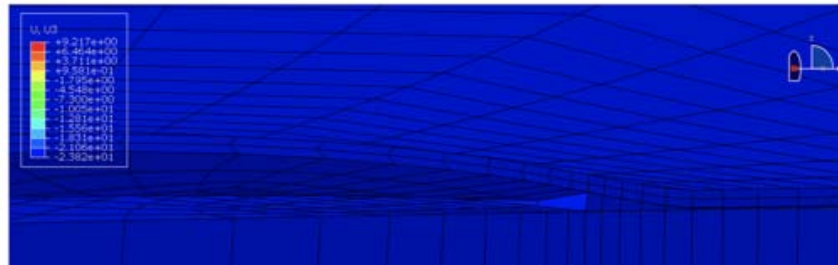


Figure 11.7: Delamination at the final instant of the simulated test with *Abaqus*.

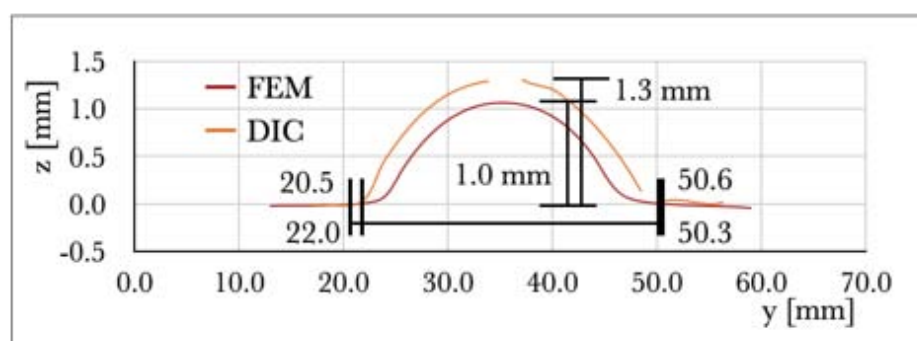


Figure 11.8: Out-of-plane displacement profile of the Bulge at the End of the test for the simulation with *Abaqus* and for the DIC analysis.

Part V
Conclusion

Chapter 12

Concluding Remarks

In this dissertation, the applicability of Digital Image Correlation as an NDT Technique for the detection of delaminations in FRP composite structural elements was investigated. The work focused on the development of elements in which it was possible to introduce defects artificially capable of reproducing delaminations. All of the flat coupons used were made out of 8HS Glass Fibre Fabric impregnated with Epoxy Resin. The choice of these materials was done to allow the creation of transparent samples, in which the damage as a consequence of the load, could be visually monitored. Two categories of specimens were mechanically loaded in Four - Point Bending to evaluate their behaviour depending on the type of insert. The first is composed of specimens having a Single Delamination Insert embedded during the manufacturing, between the top and the adjacent layer. In the other, instead, the samples were produced with Double Delamination Insert, with the first insert between the 1st and 2nd ply and the second insert between the 3rd and 4th ply. For all the inserts, a PTFE film was used.

The following sections outline the conclusions from each area in more detail.

12.1 Single Delamination Insert

Starting from the results obtained, it was possible to conclude that it is the transverse dimension of the insert, and not its area, that controls the growth of the delamination. Therefore, a comparison between the results obtained in the samples having the insert with the transverse dimension of 20 *mm*, and a comparison of the behaviour of the samples with an insert having the size of 40 *mm* are proposed below.

12.1.1 Comparison between Specimens with Circular Delamination Insert ($\phi = 20 \text{ mm}$) and Specimens with Elliptical Horizontal Insert

The specimens characterised by inserts having the transverse dimension of 20 mm are the specimens that have the Circular insert with a radius of 10 mm and those that have the Elliptical Horizontal insert.

The average values of the final size of the delamination determined with the various investigation techniques are summarised in the following Table 12.1.

Size of Delamination along Y at the End of the Test		
	Circular $\phi = 20 \text{ mm}$ Insert	Elliptical Horizontal Insert
DIC - Strain	$31.4 \pm 0.5 \text{ [mm]}$	$31.3 \pm 0.5 \text{ [mm]}$
DIC - Displacement	$30.8 \pm 0.6 \text{ [mm]}$	$31.5 \pm 0.3 \text{ [mm]}$
Correlation pixel - mm	$29.3 \pm 0.2 \text{ [mm]}$	$30.1 \pm 0.8 \text{ [mm]}$

Table 12.1: Comparison between the values of the Delamination main Size for samples with Circular $\phi = 20 \text{ mm}$ insert and those with Elliptical Horizontal insert.

The results show a good compatibility, because the values are mostly consistent among themselves. This is true even though the values resulting from DIC are slightly overestimated with respect to those resulting from the *pixel – mm* correlation optical technique. The values differences between one type of insert and the other are presumably dictated by the use of inserts with geometries that are not perfectly circular and elliptical.

In addition to the correspondence between what has been achieved in terms of maximum extension of the delamination in the two types of specimen, there are also almost identical values concerning the Bulge Area determined from the DIC analysis. Figures 12.1 and 12.2 respectively show the average values of the Bulge Area and an example of the geometry and evolution of this Bulge.

In conclusion, it can be said that the samples with 20 mm transversals size insert present at the end of the test a delamination of a size between 29 and 31 mm . Furthermore, in those specimens the area of the Bulge is approximately 230 mm^2 , that also coincides with the Delaminated Area (see Paragraph 12.1.3).

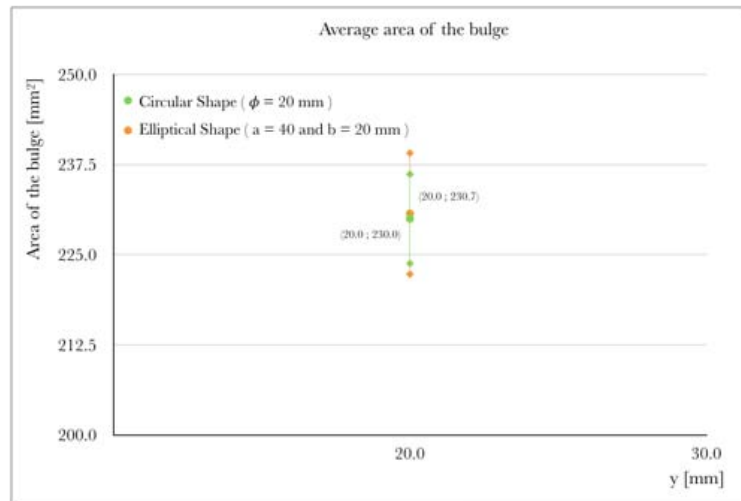


Figure 12.1: Comparison between the Average Bulge Areas of the specimens with an embedded insert having a size of 20 mm along y .

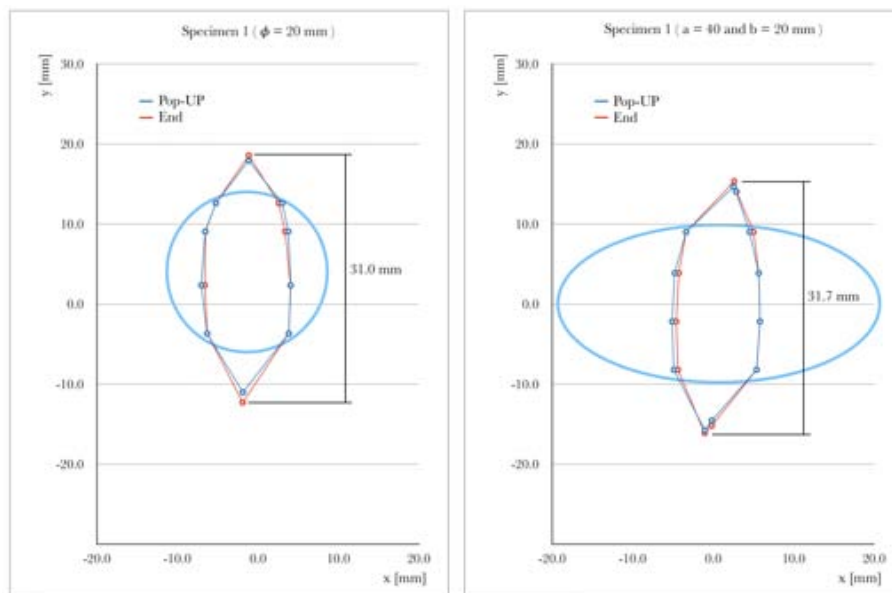


Figure 12.2: Example of the evolution of the Bulge Area for a specimen with Circular $\phi = 20$ mm insert and for one with Elliptical Horizontal insert.

12.1.2 Comparison between Specimens with Circular Delamination Insert ($\phi = 40 \text{ mm}$) and Specimens with Elliptical Vertical Insert

The specimens characterised by inserts having the transverse dimension of 40 mm are the specimens that have the Circular insert with a radius of 20 mm and those that have the Elliptical Vertical insert.

The average values of the final size of the delamination determined with the various investigation techniques are summarised in the following Table 12.2.

Size of Delamination along Y at the End of the Test		
	Circular $\phi = 40 \text{ mm}$ Insert	Elliptical Vertical Insert
DIC - Strain	$54.3 \pm 0.3 \text{ [mm]}$	$49.7 \pm 0.1 \text{ [mm]}$
DIC - Displacement	$54.5 \pm 0.7 \text{ [mm]}$	$49.9 \pm 0.4 \text{ [mm]}$
Correlation pixel - mm	$53.0 \pm 0.5 \text{ [mm]}$	$47.9 \pm 0.4 \text{ [mm]}$

Table 12.2: Comparison between the values of the Delamination main Size for samples with Circular $\phi = 40 \text{ mm}$ insert and those with Elliptical Vertical insert.

From Table 12.2 it can be seen that the values are not consistent with each other. The delamination reaches higher transversal size in specimens having a Circular insert.

This non-compatibility of the values also occurs in the Bulge Area. The average values of the Bulge Area and an example of the geometry and evolution of this bulge are respectively shown in Figures 12.3 and 12.5.

Given that inserts having the same dimensions along y are present in the samples, the differences in the extent of delamination and in the values of the Bulge Area may be due to a different longitudinal development of the inserts. In samples that have an Elliptical insert, as can be seen in Figure 12.5, the geometry of the bulge follows the edge of the insert in an almost identical way, while in samples with a Circular insert the delaminated area outside the edge of the insert is bigger than that for the Elliptical insert. As evidence of that, the delaminated areas outside the edge of the insert differ approximately by 40 mm^2 with each other (Table 12.3), and that is precisely the difference that occurs in the Bulge Area (Figure 12.3).

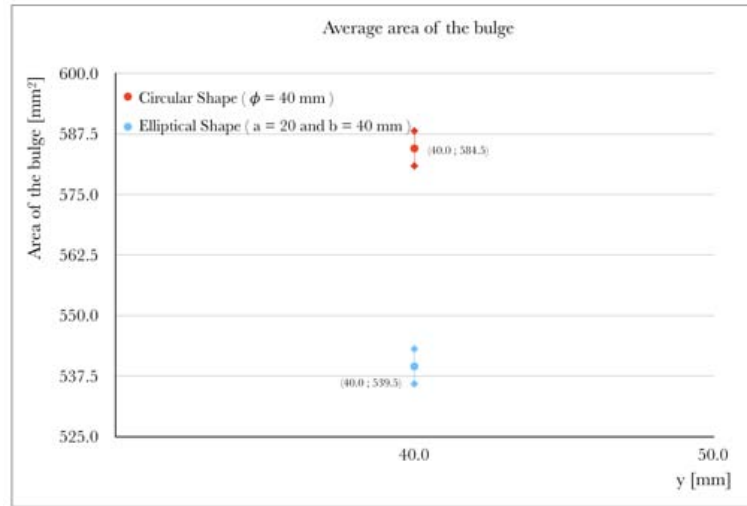


Figure 12.3: Comparison between the Average Bulge Areas of the specimens with an embedded insert having a size of 40 mm along y .

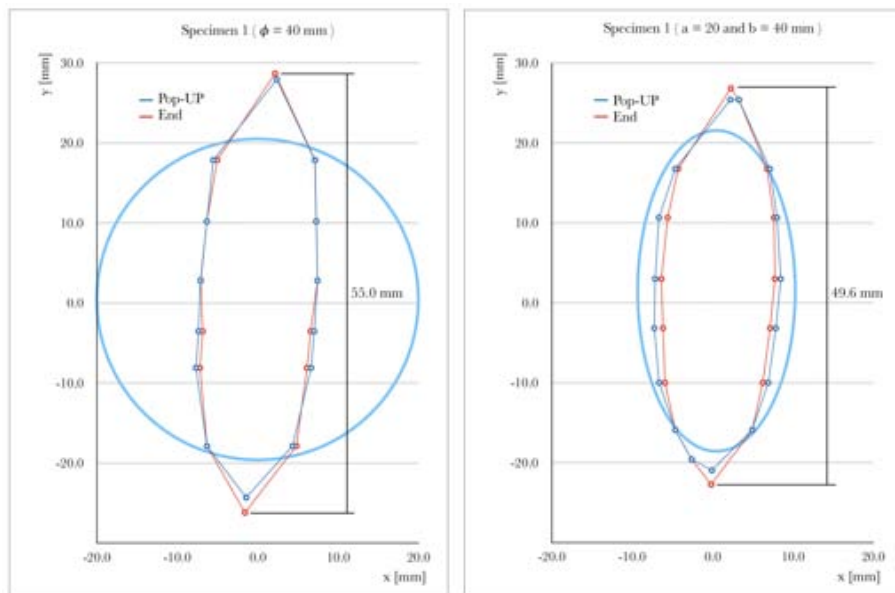


Figure 12.4: Example of the evolution of the Bulge Area for a specimen with Circular $\phi = 20$ mm insert and for one with Elliptical Vertical insert.

12.1.3 From the Bulge Area to the Delaminated Area: Validation Process

In this section the possibility of using the Bulge Area, identified thanks to DIC analysis, to determine the real delaminated area of the upper layer of the samples is investigated. The validation process is shown below.

The delaminated area outside the edge of the insert was calculated respectively from the images acquired after the tests and from the results derived from the DIC analysis. Then, the values obtained were compared with each other to verify the existence of a correlation in the results (Table 12.3). To determine the delaminated areas, the *ImageJ*[®] software was used once the *pixel-mm* conversion factor of each image was set. An example of what has been done is shown in Figure 12.5.

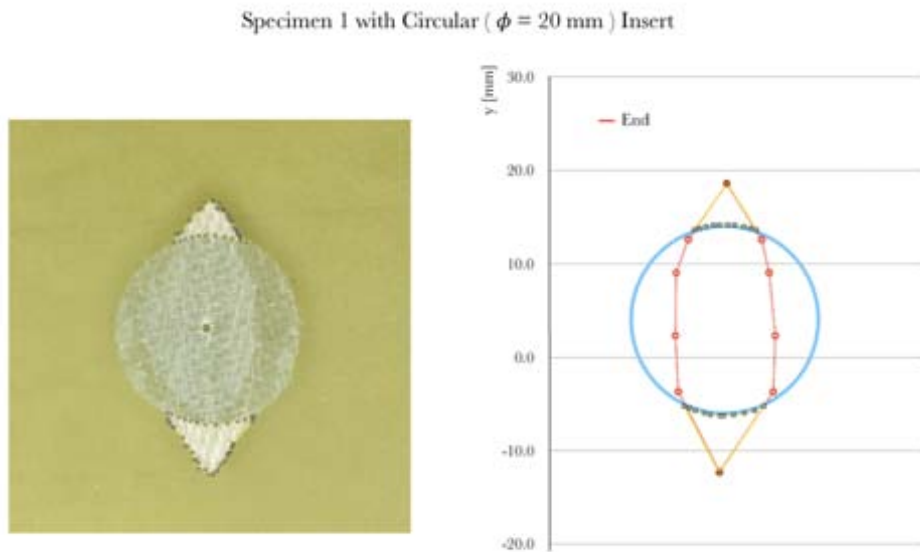


Figure 12.5: Example of the method used to calculate the Delaminated Area with *ImageJ*[®] software.

The polygons created in correspondence with the delaminated areas outside the inserts have ad hoc number of points, for each image analysed, in the attempt to best replicate the border of the delamination and the edge of the insert.

The measurement results are summarised in the following Table 12.3.

Delaminated Area outside the edge of the PTFE Insert [mm ²]								
	Circular $\phi = 20$ mm Insert		Elliptical Horizontal Insert		Circular $\phi = 40$ mm Insert		Elliptical Vertical Insert	
	From Images	From DIC	From Images	From DIC	From Images	From DIC	From Images	From DIC
Specimen 1	42.6	39.3	42.5	44.7	74.2	70.9	35.4	36.8
Specimen 2	43.5	44.8	50.2	42.4	90.9	85.2	44.3	38.2
Specimen 3	41.0	36.7			85.4	76.7		
Average	42.4	40.3	46.4	43.6	83.5	77.6	39.9	37.5
Standard Deviation	1.3	4.1	5.4	1.6	8.5	7.2	6.3	1.0
Difference [%]		5.0		6.0		7.1		6.0

Table 12.3: Comparison between the values of the Delaminated Area outside the edge of the Delamination Insert calculated respectively from the images acquired after the tests and from the results obtained with the DIC analysis.

Although the measurement performed from the results obtained from the DIC analysis is approximate, since few measuring points were used to determine the edge of the delaminated area outside the insert and the precise position of the insert itself, there is a good correlation of the results with what was obtained precisely from the images acquired after the tests. What has been determined is of considerable importance, since it shows that it is possible to objectively establish the entire delamination edge only through investigations by means of the DIC. It is plausible to consider that the Delaminated Area coincides with the Bulge Area. By contrast, Figure 12.5 shows that it is not possible with the optical *pixel-mm* correlation method to identify in an objective manner the edge of the delamination that occurred over the insert, and consequently, it is not possible to determine the total delaminated area.

In conclusion, it is recommended to use the DIC to find the bulge and, therefore, to calculate the delamination area: what is calculated in terms of the Bulge Area can also be considered the real Delaminated Area.

12.2 Double Delamination Insert

Although a limited number of samples having two delamination inserts were tested, it was possible to identify the damage evolution due to the growth of delaminations.

As regards the samples having inserts with a diameter of 20 and 40 *mm* respectively, there is a first delamination due to the upper insert and the second delamination due to the lower one. Given the characteristics of the inserts used in these samples, an analogy was found with what was obtained with the samples having a single circular insert. At the time of the first Pop-Up, it was established, starting from the DIC analysis, that the size of the delamination due to the upper insert is approximately 29 *mm*, thus finding a match with the values calculated in the specimens with a $\phi = 20$ *mm* insert. Despite the impossibility of determining the average value of the delamination that occurred at the time of the second Pop-Up in the samples in question a correspondence was found, however, with the typical values of the delaminations in the samples having single circular $\phi = 40$ *mm* insert.

Because only one sample having inserts with a diameter of 20 and 40 *mm* respectively, was tested, no conclusions can be drawn on the general evolution of the delamination. However, this does not preclude comparing what was obtained for this sample with the values of the typical delamination of specimens with a $\phi = 40$ *mm* insert. The comparison shows a correspondence in the values of the transverse dimension of the delamination: actually, the delamination due to this type of insert has an approximate size equal to 55 *mm*.

Finally, it is possible to note the influence that the relative position of the inserts has in the generation of delaminations. If in the case of samples with a lower insert positioned above the larger one, the two distinct delaminations occur at different instants (Figure 10.2); instead, for the sample with a lower insert positioned in depth, the two delaminations are presumably created simultaneously, even though if they have different sizes.

Chapter 13

Possible Future Works

The present work provided supplementary evidence that the strain and out-of-plane displacement profiles measured by using DIC can be used to monitor delaminations in structural elements given certain load cases. The novelty introduced in this project was the search for methods for evaluating the delamination growth. The characteristic size of the delamination that drives its growth was studied and quantified by measuring its extension. Furthermore, the Bulge Area due to the occurrence of the localised buckling in the compression surface of the structural element in correspondence to the PTFE insert was determined, and its evolution was assessed, for increasing load levels.

The following are suggestions on areas where further investigations could be conducted.

To further this work directly, the specimens could be subjected to fatigue tests, since testing them in quasi-static manner causes a low degree of delamination, so that the component failure is eventually due to the initiation of other types of damage, such as fibre breakage. Arguably, through fatigue tests, the growth of delamination damage would be facilitated without the development of other damage phenomena typical of composites.

In addition, it is possible to test samples with multiple delamination inserts. The inserts could be placed in such a way so as to create what could be the typical damage cone of elements that have undergone a barely visible impact damage, so as to be able to assess the residual resistance of the component.

Probably, these new studies should be carried out by using a thicker PTFE film for the realisation of the delamination inserts. This because with the film used in this work it is not possible to guarantee an adequate

degree of debonding between the plies where it is interposed, because, by adhering, it becomes one with them.

However, the simple extension of the present investigation to different composite material systems would increase the confidence in the results obtained.

Part VI
References

Bibliography

- [1] Daniel I. M. and Ishai O. (1994), Engineering Mechanics of Composite Materials. *Oxford University Press*
- [2] Hull D. and Clyne T. W. (1996), An Introduction to Composite Materials (Cambridge Solid State Science Series). *Cambridge University Press*
- [3] Bolotin V.V. (1996), Delaminations in composite structures: Its origin, buckling, growth and stability. *Composites Part B: Engineering* **27**, pp. 129-145
- [4] Campbell F. C. (2004), Manufacturing Processes for Advanced Composites. *Elsevier*
- [5] Quaresimin M. (2009), Introduzione alla Progettazione con i Materiali Compositi. *Università di Padova*
- [6] Senthil K., Arockiarajan A., Palaninathan R., Santhosh B. and Usha K. M. (2013), Defects in Composite Structures: Its effects and prediction methods - A comprehensive review. *Composite Structures* **106**, pp. 139-149
- [7] Heslehurst R. B. (2014), Defects and Damage in Composite Materials and Structures. *CRC Press*
- [8] Kharghani N. and Guedes Soares C, (2016), Behaviour of composite laminates with embedded delaminations. *Composite Structures* **150**, pp. 226-239
- [9] McLoughlin J. and Sabir T. (2018), High-Performance apparel: Materials, Development and Applications. *Elsevier*
- [10] Adams R. D. and Cawley P. (1988), A review of defect types and Nondestructive Testing Techniques for composites and bonded joints. *NDT International* **21**, pp. 208-222

- [11] Dong Y. and Ansari F. (2011), Non-destructive Testing and Evaluation (NDT/NDE) of civil structures rehabilitated using Fiber Reinforced Polymer (FRP) Composites. *Service Life Estimation and Extension of Civil Engineering Structures*, pp. 193-222
- [12] Ibrahim M. E. (2014), Non-destructive Evaluation of Thick- Section Composites and Sandwich Structures: A review. *Composites Part A: Applied Science and Manufacturing* **64**, pp. 36-48
- [13] Jolly M. R., Prabhakar A, Sturzu B., Hollstein K., Singh R., Thomas S., Foote P. and Shaw A. (2015), Review of Non-Destructive Testing (NDT) Techniques and their applicability of thick walled composites. *Procedia CIRP* **38**, pp. 129-136
- [14] Gholizadeh S. (2016), A review of Non-Destructive Testing Methods of Composite Materials. *Procedia Structural Integrity* **1**, pp. 50-57
- [15] Helm J. D., McNeil S. R. and Sutton M. A. (1996) Improved Three-Dimensional Image Correlation for surface displacement measurement. *Optics and Lasers in Engineering* **35**, pp. 1911-1920
- [16] Lecompte D., Smits A., Bossuyt S., Sol H., Vantomme J., Van Hemelrijck D. and Habraken A. M. (2006), Quality assessment of speckle patterns for Digital Image Correlation. *Optics and Lasers in Engineering* **44**, pp. 1132-1145
- [17] Yaofeng S. and Pang J. H. L. (2007), Study of optimal subset size in Digital Image Correlation of speckle pattern images. *Optics and Lasers in Engineering* **45**, pp. 967-974
- [18] Pan B., Xie H. M., Wang Z. Y., Qian K. M. and Wang Z. Y. (2008), Study on subset size selection in Digital Image Correlation for speckle patterns. *Optics Express* **16**, pp. 7037-7048
- [19] Pan B., Qian K., Xie H. and Asundi A. (2009), Two-Dimensional Digital Image Correlation for in-plane displacement and strain measurement: A review. *Measurement Science and Technology* **20**, 062001
- [20] Sutton M. A., Orteu J.-J. and Schreier H. W. (2009), Image correlation for shape, motion and deformation measurement. *Springer*
- [21] McCormick N. and Lord J. (2010), Digital Image Correlation. *Materialstoday* **13**, pp. 52-54
- [22] Reu P. (2012), The art and application of DIC. *Experimental Techniques*

- [23] Chen F., Chen X., Xie X., Feng X. and Yang L. (2013), Full-field 3D measurement using multi-camera Digital Image Correlation system. *Optics and Lasers in Engineering* **51**, pp. 1044-1052
- [24] Pan B. (2018), Digital Image Correlation for surface deformation measurement: Historical developments, Recent advances and Future goals. *Measurement Science and Technology* **29**, 082001
- [25] Jones E. M. C. and Iadicola M. A. (2018), A good practices guide for digital image correlation. *International Digital Image Correlation Society (iDICs)*
- [26] Brynk T., Molak R.-M., Janiszewska M. and Pakiela Z. (2012), Digital Image Correlation measurements as a tool of composites deformation description. *Computational Materials Science* **64**, pp. 157-161
- [27] Bataxi, Chen X., Yu Z., Wang H. and Bil C. (2015), Strain monitoring on damaged composite laminates using Digital Image Correlation. *Procedia Engineering* **99**, pp. 353-360
- [28] Ajmal O. Z. (2018), The use of digital image correlation to monitor delaminations in composite structures. *University of Surrey*
- [29] Bataxi, Chen X., Yu Z., Wang H. and Bil C. (2019), Detection of delamination in polymer composites by Digital Image Correlation - Experimental test. *Polymers* **11**, pp. 353-360
- [30] Hu N., Fukunaga H., Sekine H. and Mohammad Ali K. (1999), Compressive buckling of laminates with an embedded delamination. *Composite Science and Technology* **59**, pp. 1247-1260
- [31] Short G. J., Guild F. J. and Pavier M. J. (2002), Delamination in flat and curved composite laminates subjected to compressive load. *Composite Structures* **58**, pp. 249-258
- [32] Ruan J. T., Aymerich F., Tong J. W. and Wang Z. Y. (2014), Optical evaluation on delamination buckling of composite laminate with impact damage. *Advances in Materials Science and Engineering* **2014**, 390965
- [33] Rhead A. T., Butler R. and Hunt G. W. (2017), Compressive strength of composite laminates with delamination-induced interaction of panel and sublaminates buckling modes. *Composite Structures* **171**, pp. 326-334

- [34] Szebényi G. and Hliva V. (2019), Detection of Delamination in Polymer Composites by Digital Image Correlation - Experimental Test. *Polymers 2019* **11**, 523
- [35] Gong W., Chen J. and Patterson E. A. (2015), An experimental study of the behaviour of delaminations in composite panels subjected to bending. *Composite Structures* **123**, pp. 9-18
- [36] Gong W., Chen J. and Patterson E. A. (2016), Buckling and delamination growth behaviour of delaminated composite panels subject to four-point bending. *Composite Structures* **138**, pp. 122-133
- [37] Shen F., Lee K. H. and Tay T. E. (2001), Modelling delamination growth in laminated composites. *Composite Science and Technology* **61**, pp. 1239-1251
- [38] Reeder J. R., Chunchu P. B., Song K. and Ambur D. R. (2002), Postbuckling and growth of delaminations in composite plates subjected to axial compression. *American Institute of Aeronautics and Astronautics* **1749**
- [39] Raju J., Sreedhar D. S. and Manjunatha C. M. (2014), Prediction of delamination growth behavior in a Carbon Fiber Composite laminate subjected to constant amplitude compression-compression fatigue loads. *Global Journal of Engineering, Design and Technology* **3** (4), pp. 19-23
- [40] Greenhalgh E. and Singh S. (2019) Investigation of the Failure Mechanisms for Delamination Growth from embedded defects. *Mechanical Sciences Sector, DERA*
- [41] Composite plate saw User Manual for COMPCUT 200. *Sharp & Tappin Technologies*
- [42] ASTM International. Standard Test Method for Flexural Properties of Polymer Matrix Composite Materials. D7264/D7264M-07
- [43] Camanho P.P., Dávila C.G. and De Moura M.F. (2003), Numerical Simulation of Mixed-mode Progressive Delamination in Composite Materials. *Journal of Composite Materials* **37**, pp. 1415-1438
- [44] Rathinasabapathy M. (2005), The Application of VCCT for *Abaqus* to Prediction and Simulation of Delamination Growth in Composite Structures. *SAE Technical Paper Series*
- [45] Turon A., Dávila C.G., Camanho P.P. and Costa J. (2007), An Engineering Solution for solving Mesh Size Effects in the Simulation

- of Delamination with Cohesive Zone Models. *Engineering Fracture Mechanics* **74** (10), pp.1665-1682
- [46] Butler R., Rhead A. T., Liu W. and Kontis N. (2012), Compressive strength of delaminated aerospace composites. *Philosophical Transactions of the Royal Society A* **370**, pp. 1759-1779
- [47] Singh K. K., Singh N. K. and Jha R. (2015), Analysis of symmetric and asymmetric glass fiber reinforced plastic laminates subjected to low-velocity impact. *Journal of Composite Materials* **0** (0), pp. 1-11
- [48] Mekonnen A. A., Woo K., Kang M. and Kim I.-G. (2020), Post-buckling and delamination propagation behavior of composite laminates with embedded delamination. *Journal of Mechanical Science and Technology* **34** (3), pp. 1099-1110

Part VII
Appendices

A.1 Support for the description of test repeatability

Circular $\phi = 20$ mm Delamination Insert

Specimens Thickness [mm]			
Measurement Points	Specimen 1	Specimen 2	Specimen 3
A	4.27	4.36	4.10
B	4.31	4.32	4.14
C	4.33	4.31	4.14
D	4.35	4.27	4.13
E	4.22	4.29	4.18
F	4.35	4.28	4.26
G	4.35	4.29	4.25
H	4.37	4.24	4.24
Average	4.32	4.30	4.18
Standard Deviation	0.05	0.04	0.06

Table 1: Average Thickness of specimens with $\phi = 20$ mm insert.

Load at the moment of the Pop-Up		
	Load [N]	Extension [mm]
Specimen 1	2798.6	12.4
Specimen 2	2608.0	11.4
Specimen 3	2438.2	11.1

Table 2: Load at the moment of the Pop-Up for specimens with $\phi = 20$ mm insert.

Circular $\phi = 40$ mm Delamination Insert

Specimens Thickness [mm]			
Measurement Points	Specimen 1	Specimen 2	Specimen 3
A	4.27	4.22	4.15
B	4.27	4.26	4.16
C	4.30	4.27	4.16
D	4.31	4.30	4.22
E	4.34	4.24	4.24
F	4.35	4.29	4.24
G	4.32	4.30	4.25
H	4.29	4.33	4.29
Average	4.31	4.28	4.21
Standard Deviation	0.03	0.04	0.05

Table 3: Average Thickness of specimens with $\phi = 40$ mm insert.

Load at the moment of the Pop-Up		
	Load [N]	Extension [mm]
Specimen 1	2759.0	12.5
Specimen 2	2663.7	11.8
Specimen 3	2585.2	12.7

Table 4: Load at the moment of the Pop-Up for specimens with $\phi = 40$ mm insert.

Elliptical Horizontal Delamination Insert

Specimens Thickness [mm]		
Measurement Points	Specimen 1	Specimen 2
A	4.14	4.10
B	4.10	4.13
C	4.10	4.10
D	4.12	4.05
E	4.10	4.14
F	4.10	4.16
G	4.12	4.16
H	4.10	4.09
Average	4.11	4.12
Standard Deviation	0.02	0.04

Table 5: Average Thickness of specimens with Elliptical Horizontal insert.

Load at the moment of the Pop-Up		
	Load [N]	Extension [mm]
Specimen 1	2357.7	11.3
Specimen 2	2394.7	11.3

Table 6: Load at the moment of the Pop-Up for specimens with Elliptical Horizontal insert.

Elliptical Vertical Delamination Insert

Specimens Thickness [mm]		
Measurement Points	Specimen 1	Specimen 2
A	4.11	4.12
B	4.05	4.13
C	4.03	4.12
D	4.03	4.05
E	4.12	4.14
F	4.07	4.12
G	4.04	4.13
H	4.05	4.06
Average	4.06	4.11
Standard Deviation	0.03	0.03

Table 7: Average Thickness of specimens with Elliptical Vertical insert.

Load at the moment of the Pop-Up		
	Load [N]	Extension [mm]
Specimen 1	2135.5	10.3
Specimen 2	2205.2	10.2

Table 8: Load at the moment of the Pop-Up for specimens with Elliptical Vertical insert.

Double Circular Delamination Insert $\phi_1 = 20 \text{ mm}$ and $\phi_2 = 40 \text{ mm}$

Specimens Thickness [mm]		
Measurement Points	Specimen 1	Specimen 2
A	4.00	4.10
B	3.97	4.10
C	3.96	4.10
D	3.95	4.05
E	4.09	4.01
F	4.03	4.11
G	4.01	4.09
H	3.98	4.05
Average	4.00	4.08
Standard Deviation	0.05	0.04

Table 9: Average Thickness of specimens with Double Circular insert, with the smallest above.

Load at the moment of the Pop-Up				
	1st Pop-Up		2nd Pop-Up	
	Load [N]	Extension [mm]	Load [N]	Extension [mm]
Specimen 1	2317.0	11.8	3211.0	19.6
Specimen 2	2549.3	13.0	3380.2	21.1

Table 10: Load at the moment of the Pop-Up for specimens with Double insert, with the smallest above.

Double Circular Delamination Insert

$\phi_1 = 40 \text{ mm}$ and $\phi_2 = 20 \text{ mm}$

Specimens Thickness [mm]	
Measurement Points	Specimen 1
A	3.99
B	4.00
C	4.03
D	4.10
E	3.93
F	3.96
G	3.99
H	4.07
Average	4.01
Standard Deviation	0.06

Table 11: Average Thickness of specimens with Double Circular insert, with the biggest above.

Load at the moment of the Pop-Up				
	1st Pop-Up		2nd Pop-Up	
	Load [N]	Extension [mm]	Load [N]	Extension [mm]
Specimen 1	2936.7	15.8	3113.5	18.5

Table 12: Load at the moment of the Pop-Up for specimens Double Circular insert, with the biggest above.

A.2 Support for the calculation of the Bulge Area

Circular $\phi = 20 \text{ mm}$ Delamination Insert
Specimen 1

Specimen 1 - Area of the Bulge - SUBSET 31 STEP SIZE 10 FILTER SIZE 11 -							
IMAGE 249	POP-UP	IMAGE 276	3000 N	IMAGE 310	3250 N	IMAGE 340	END
X	Y	X	Y	X	Y	X	Y
-1.9	-11.0	-1.89	-11.4	-1.9	-12.3	-1.9	-12.3
-6.3	-3.7	-6.3	-3.7	-6.3	-3.7	-6.3	-3.7
-7.1	2.4	-7.1	2.4	-6.7	2.4	-6.6	2.4
-6.6	9.1	-6.6	9.1	-6.5	9.1	-6.5	9.1
-5.25	12.6	-5.7	12.6	-5.25	12.6	-5.25	12.6
-1.2	17.9	-1.1	18.6	-1.1	18.6	-1.2	18.6
3.0	12.6	2.6	12.6	2.6	12.6	2.6	12.6
3.8	9.1	3.8	9.1	3.4	9.1	3.4	9.1
4.1	2.4	4.1	2.4	4.1	2.4	4.0	2.4
3.8	-3.7	3.8	-3.7	3.8	-3.7	3.8	-3.7
-1.9	-11.0	-1.89	-11.4	-1.9	-12.3	-1.9	-12.3

Table 13: Values for the calculation of the Bulge Area for Specimen 1 with $\phi = 20 \text{ mm}$ insert.

Specimen 1 - Area of the Bulge	
Instant	Area [mm ²]
IMAGE 249	228.7
IMAGE 276	233.8
IMAGE 310	231.1
IMAGE 340	229.9

Table 14: Value of the Bulge Area at different instants for Specimen 1 with $\phi = 20 \text{ mm}$ insert.

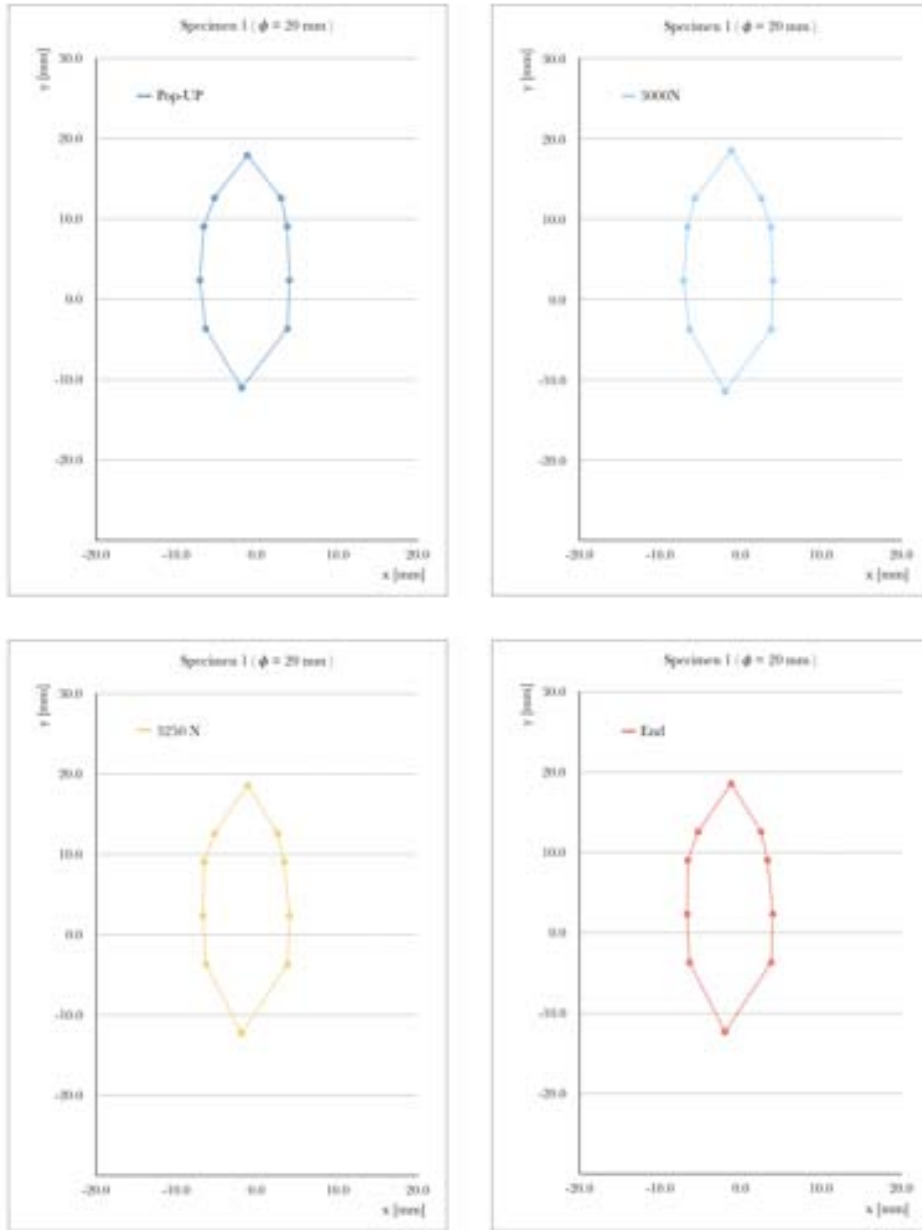


Figure 1: Bulge Area at different instants for Specimen 1 with $\phi = 20$ mm insert.

Specimen 2

Specimen 2 - Area of the Bulge - SUBSET 31 STEP SIZE 11 FILTER SIZE 11 -							
IMAGE 231	POP-UP	IMAGE 293	3000 N	IMAGE 332	3250 N	IMAGE 352	END
X	Y	X	Y	X	Y	X	Y
0.0	-10.5	0.0	-10.5	-0.0	-11.3	-0.0	-11.6
-3.8	-4.8	-3.8	-4.8	-3.8	-4.8	-3.8	-4.8
-4.7	-1.5	-4.7	-1.5	-4.3	-1.5	-4.3	-1.5
-5.2	6.3	-4.7	6.3	-4.7	6.3	-4.7	6.3
-3.6	13.1	-3.6	13.1	-3.6	13.1	-3.6	13.1
0.7	18.85	0.7	18.85	0.75	19.6	0.75	19.7
5.0	13.1	5.0	13.1	5.1	13.1	5.1	13.1
6.2	6.3	6.2	6.3	5.8	6.3	5.8	6.3
6.1	-1.5	6.1	-1.5	5.6	-1.5	5.6	-1.5
5.0	-4.8	5.0	-4.8	5.0	-4.8	5.0	-4.8
0.0	-10.5	0.0	-10.5	-0.0	-11.3	-0.0	-11.6

Table 15: Values for the calculation of the Bulge Area for Specimen 2 with $\phi = 20 \text{ mm}$ insert.

Specimen 2 - Area of the Bulge	
Instant	Area [mm ²]
IMAGE 231	236.7
IMAGE 293	233.1
IMAGE 332	232.6
IMAGE 352	234.3

Table 16: Value of the Bulge Area at different instants for Specimen 2 with $\phi = 20 \text{ mm}$ insert.

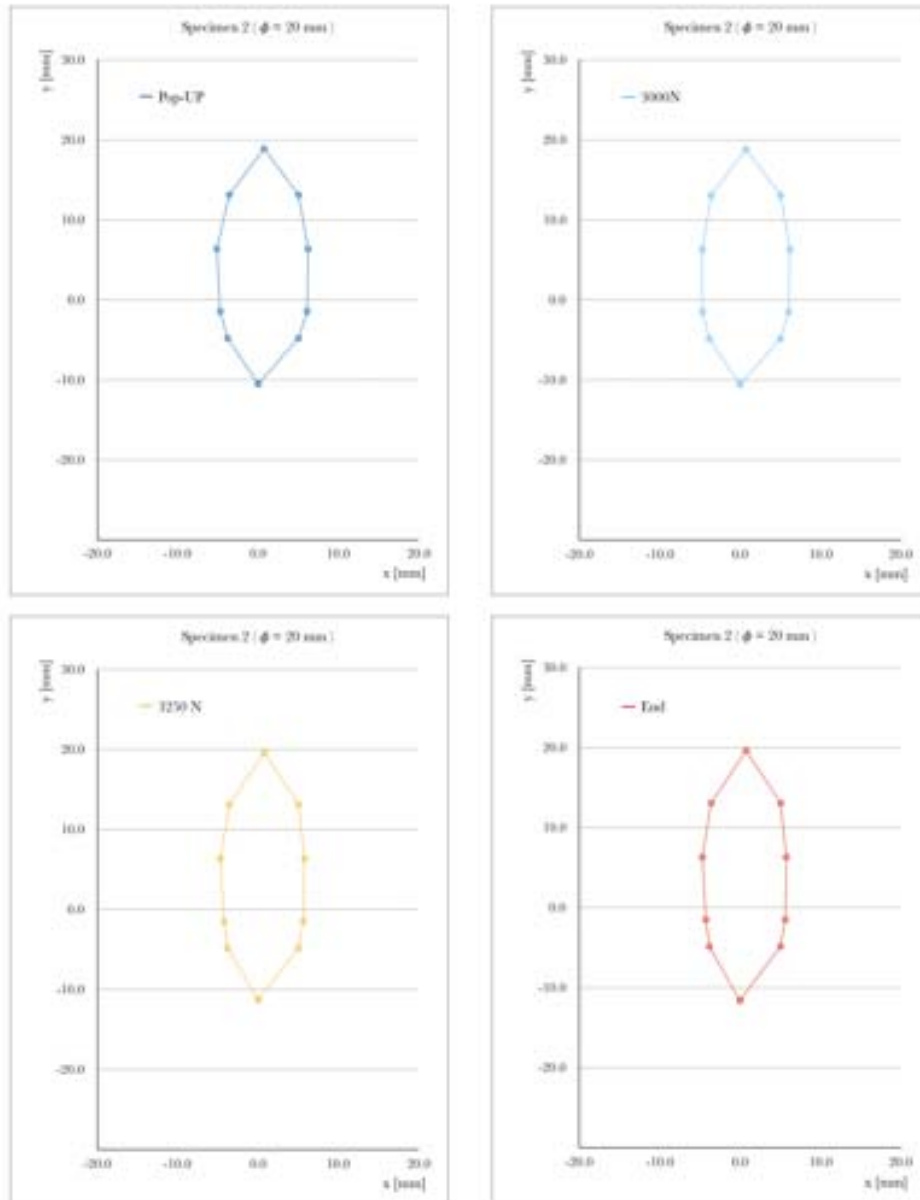


Figure 2: Bulge Area at different instants for Specimen 2 with $\phi = 20$ mm insert.

Specimen 3

Specimen 3 - Area of the Bulge - SUBSET 31 STEP SIZE 11 FILTER SIZE 11 -							
IMAGE 222	POP-UP	IMAGE 293	3000 N	IMAGE 332	3250 N	IMAGE 355	END
X	Y	X	Y	X	Y	X	Y
-1.1	-13.0	-1.1	-13.4	-1.1	-14.1	-1.1	-14.7
-6.6	-8.4	-6.1	-8.4	-6.1	-8.4	-6.1	-8.4
-7.0	-1.0	-7.0	-1.0	-7.0	-1.0	-6.6	-1.0
-6.9	5.6	-6.9	5.6	-6.4	5.6	-6.4	5.6
-5.0	10.0	-5.0	10.0	-5.0	10.0	-5.0	10.0
-1.6	13.7	-1.6	13.7	-1.6	14.3	-1.6	14.3
2.2	10.0	2.2	10.0	2.2	10.0	2.2	10.0
4.1	5.6	3.6	5.6	3.6	5.6	3.6	5.6
4.3	-1.0	3.8	-1.0	3.8	-1.0	3.8	-1.0
2.7	-8.4	2.7	-8.4	2.7	-8.4	2.7	-8.4
-1.1	-13.0	-1.1	-13.4	-1.1	-14.1	-1.1	-14.7

Table 17: Values for the calculation of the Bulge Area for Specimen 3 with $\phi = 20 \text{ mm}$ insert.

Specimen 3 - Area of the Bulge	
Instant	Area [mm ²]
IMAGE 222	224.6
IMAGE 293	217.1
IMAGE 332	219.6
IMAGE 355	219.4

Table 18: Value of the Bulge Area at different instants for Specimen 3 with $\phi = 20 \text{ mm}$ insert.

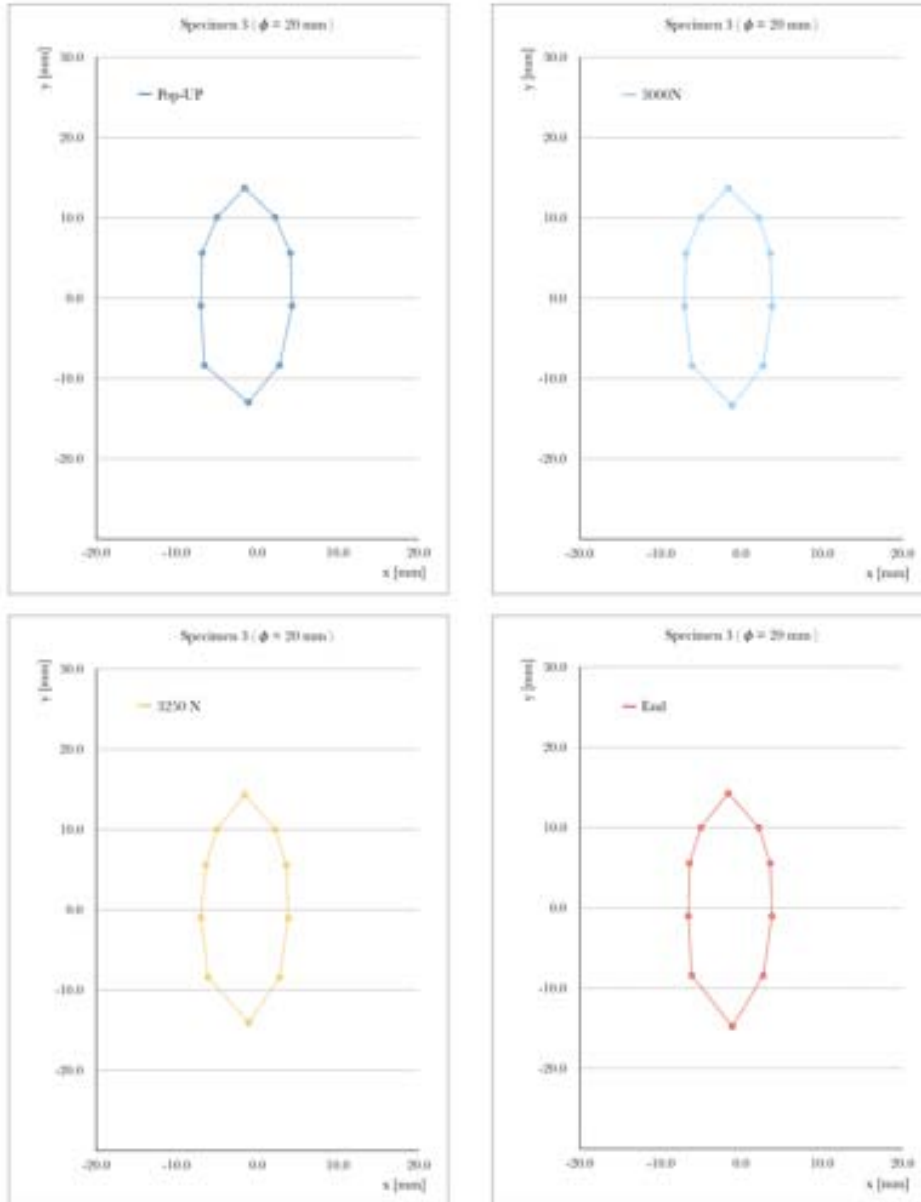


Figure 3: Bulge Area at different instants for Specimen 3 with $\phi = 20$ mm insert.

Circular $\phi = 40 \text{ mm}$ Delamination Insert Specimen 1

Specimen 1 - Area of the Bulge - SUBSET 31 STEP SIZE 10 FILTER SIZE 11 -								
IMAGE 250	POP-UP	IMAGE 291	3000 N	IMAGE 328	3250 N	IMAGE 390	END	
X	Y	X	Y	X	Y	X	Y	
-1.45	-24.3	-1.5	-25.5	-1.6	-25.5	-1.6	-26.2	
-6.3	-17.9	-6.3	-17.9	-6.3	-17.9	-6.3	-17.9	
-7.7	-8.1	-7.2	-8.1	-7.2	-8.1	-7.2	-8.1	
-7.4	-3.5	-7.4	-3.5	-7.4	-3.5	-3.5	-6.9	
-7.1	2.8	-7.1	2.8	-7.1	2.8	-7.1	2.8	
-6.3	10.2	-6.4	10.2	-6.3	10.2	-6.3	10.2	
-5.5	17.9	-5.05	17.9	-5.05	17.9	-5.05	17.9	
2.35	27.9	2.35	28.1	2.4	28.7	2.15	28.7	
7.1	17.9	7.1	17.9	7.1	17.9	7.1	17.9	
7.3	10.2	7.3	10.2	7.3	10.2	7.3	10.2	
7.4	2.8	7.4	2.8	7.4	2.8	7.4	2.8	
7.0	-3.5	6.55	-3.5	6.55	-3.5	6.55	-3.5	
6.6	-8.1	6.1	-8.1	6.1	-8.1	6.1	-8.1	
4.3	-17.9	3.8	-17.9	4.3	-17.9	4.8	-17.9	
-1.45	-24.3	-1.5	-25.5	-1.6	-25.5	-1.6	-26.2	

Table 19: Values for the calculation of the Bulge Area for Specimen 1 with $\phi = 40 \text{ mm}$ insert.

Specimen 1 - Area of the Bulge	
Instant	Area [mm ²]
IMAGE 250	580.8
IMAGE 291	571.2
IMAGE 328	578.4
IMAGE 390	583.9

Table 20: Value of the Bulge Area at different instants for Specimen 1 with $\phi = 40 \text{ mm}$ insert.

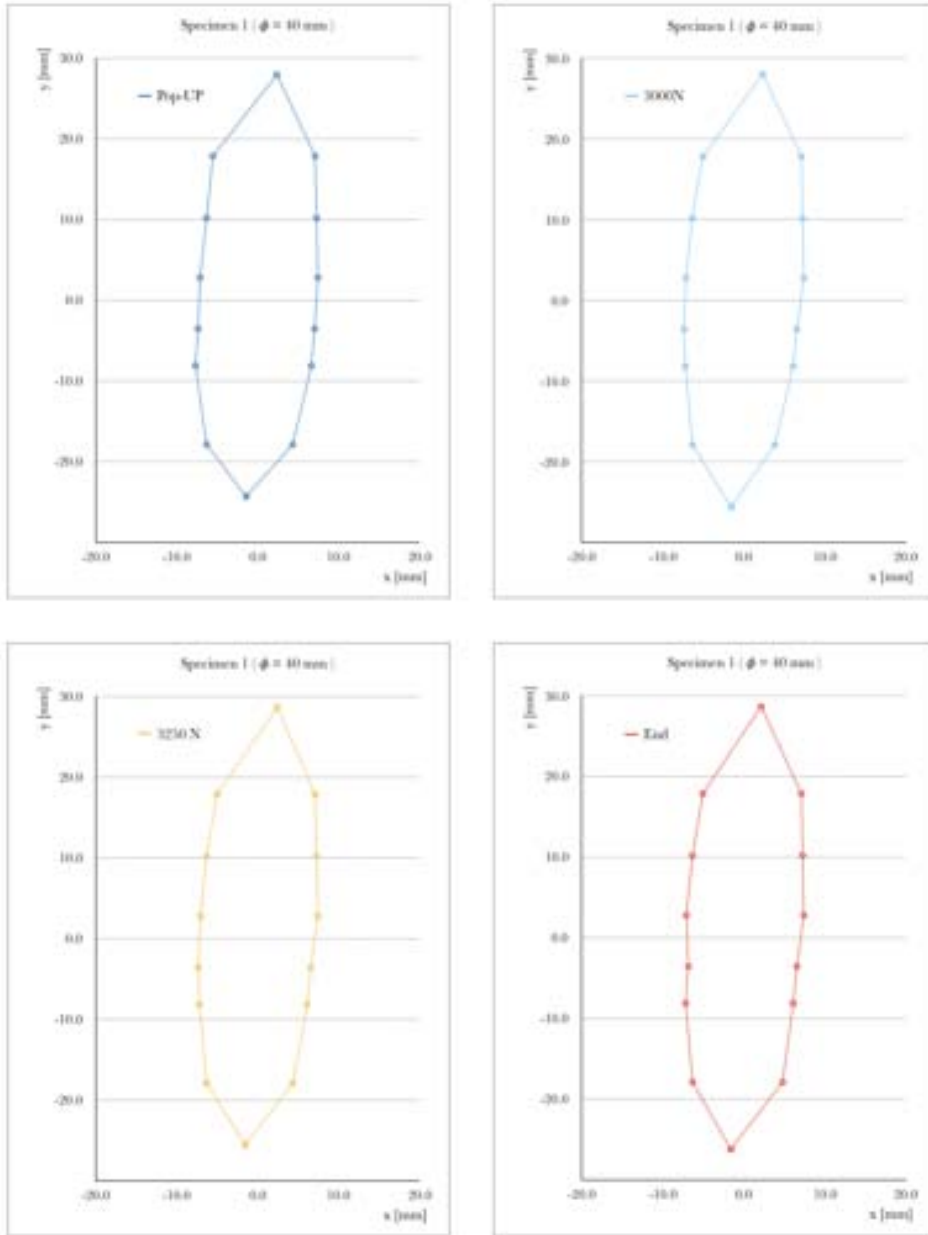


Figure 4: Bulge Area at different instants for Specimen 1 with $\phi = 40$ mm insert.

Specimen 2

Specimen 2 - Area of the Bulge - SUBSET 31 STEP 10 FILTER 11 -							
IMAGE 236	POP-UP	IMAGE 286	3000 N	IMAGE 320	3250 N	IMAGE 375	END
X	Y	X	Y	X	Y	X	Y
-3.4	-20.4	-3.4	-21.2	-3.5	-22.2	-3.5	-22.8
-9.2	-12.7	-8.5	-12.7	-8.5	-12.7	-8.5	-12.7
-9.5	-5.45	-8.9	-5.45	-8.9	-5.45	-8.85	-5.45
-9.1	1.5	-9.1	1.5	-9.1	1.5	-9.1	1.5
-8.8	9.3	-8.1	9.3	-8.1	9.3	-8.1	9.3
-8.3	15.0	-7.7	15.0	-7.6	15.0	-7.6	15.0
-7.2	20.5	-7.20	20.5	-7.1	20.5	-7.1	20.5
-0.3	29.6	-0.40	29.9	-0.5	30.1	-0.7	30.7
5.9	20.5	5.6	20.5	5.3	20.5	5.25	20.5
6.05	15.0	5.7	15.0	5.4	15.0	5.4	15.0
6.2	9.3	5.5	9.3	5.5	9.3	5.5	9.3
5.7	1.5	5.2	1.5	5.0	1.5	5.0	1.5
5.15	-5.45	4.7	-5.45	4.5	-5.45	4.5	-5.45
3.4	-12.7	3.4	-12.7	3.4	-12.7	3.4	-12.7
-3.4	-20.4	-3.4	-21.2	-3.5	-22.2	-3.5	-22.8

Table 21: Values for the calculation of the Bulge Area for Specimen 2 with $\phi = 40$ mm insert.

Specimen 2 - Area of the Bulge	
Instant	Area [mm ²]
IMAGE 236	584.6
IMAGE 286	557.9
IMAGE 320	560.4
IMAGE 375	563.6

Table 22: Value of the Bulge Area at different instants for Specimen 2 with $\phi = 40$ mm insert.

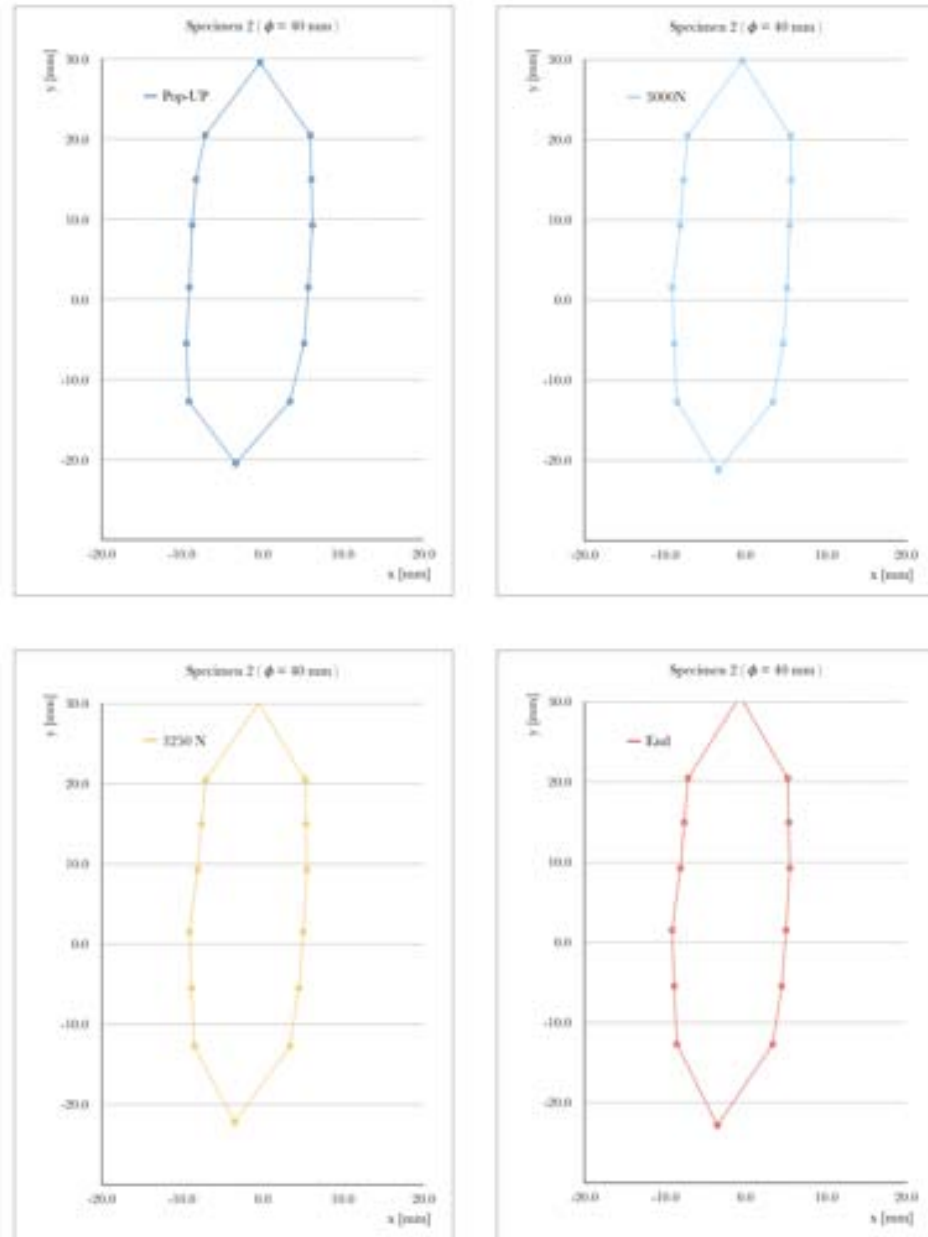


Figure 5: Bulge Area at different instants for Specimen 2 with $\phi = 40$ mm insert.

Specimen 3

Specimen 3 - Area of the Bulge - SUBSET 31 STEP SIZE 10 FILTER SIZE 11 -							
IMAGE 255	POP-UP	IMAGE 323	3000 N	IMAGE 368	3250 N	IMAGE 390	END
X	Y	X	Y	X	Y	X	Y
-0.4	-26.1	-0.4	-26.6	-0.4	-26.6	-0.4	-26.7
-6.5	-17.7	-6.5	-17.7	-6.5	-17.7	-6.5	-17.7
-7.8	-10.9	-6.8	-10.9	-6.8	-10.9	-6.8	-10.9
-7.15	-1.15	-7.6	-1.15	-7.15	-1.15	-7.1	-1.15
-7.4	7.0	-6.9	7.0	-6.9	7.0	-6.9	7.0
-6.1	13.4	-6.1	13.4	-6.1	13.4	-6.1	13.4
-5.2	18.7	-5.2	18.7	-5.2	18.7	-5.2	18.7
0.9	27.3	0.9	27.3	0.9	28.05	0.9	28.1
5.9	18.7	5.9	18.7	6.4	18.7	6.4	18.7
7.0	13.4	6.5	13.4	6.5	13.4	6.5	13.4
7.2	7.0	7.2	7.0	7.1	7.0	7.1	7.0
6.9	-1.15	6.8	-1.15	6.8	-1.15	6.8	-1.15
6.0	-10.9	6.0	-10.9	6.0	-10.9	6.0	-10.9
5.1	-17.7	5.1	-17.7	5.1	-17.7	5.1	-17.7
-0.4	-26.1	-0.4	-26.6	-0.4	-26.6	-0.4	-26.7

Table 23: Values for the calculation of the Bulge Area for Specimen 3 with $\phi = 40 \text{ mm}$ insert.

Specimen 3 - Area of the Bulge	
Instant	Area [mm ²]
IMAGE 255	588.1
IMAGE 323	579.3
IMAGE 368	582.4
IMAGE 390	582.8

Table 24: Value of the Bulge Area at different instants for Specimen 3 with $\phi = 40 \text{ mm}$ insert.

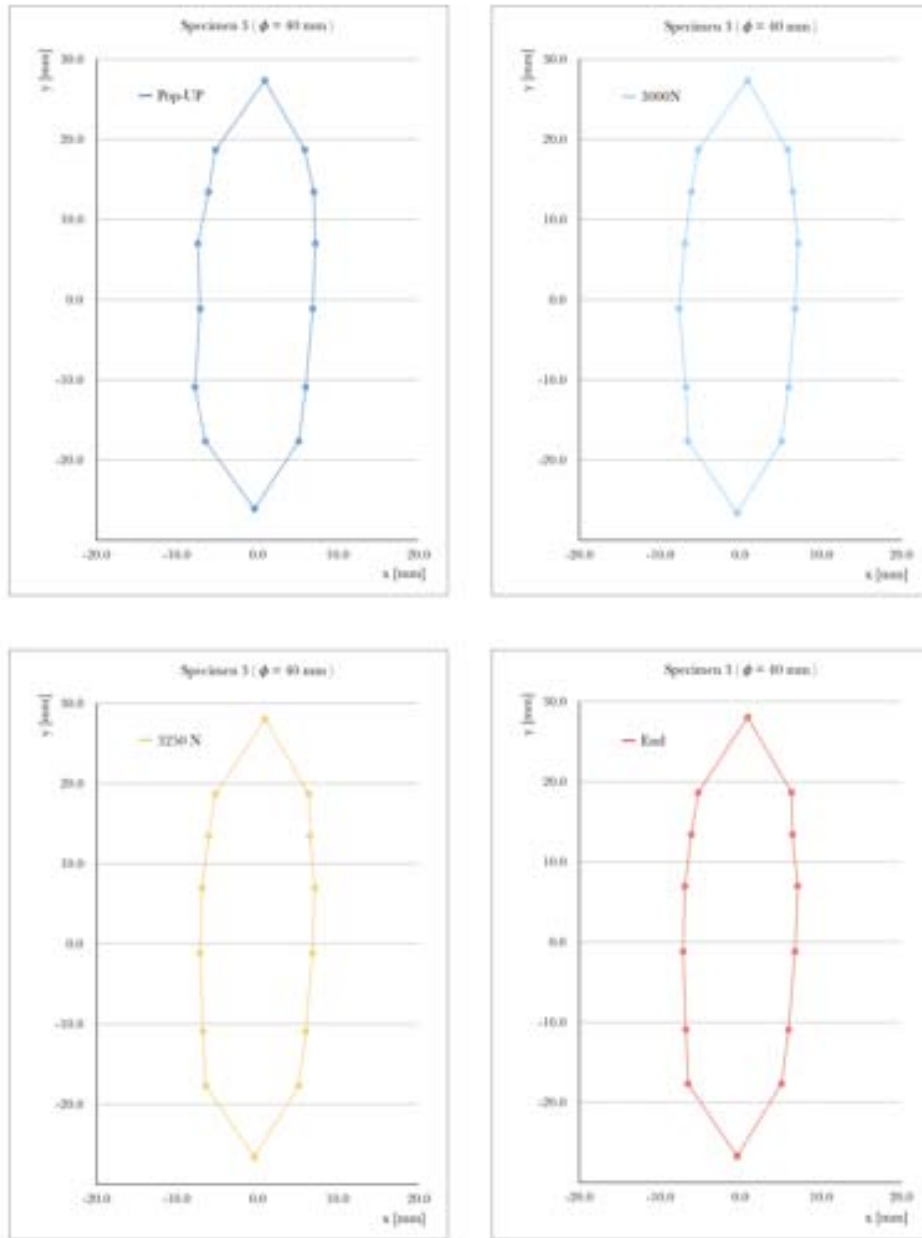


Figure 6: Bulge Area at different instants for Specimen 3 with $\phi = 40$ mm insert.

Elliptical Horizontal Delamination Insert Specimen 1

Specimen 1 - Area of the Bulge - SUBSET 31 STEP SIZE 10 FILTER SIZE 13 -								
IMAGE 227	POP-UP	IMAGE 281	2750 N	IMAGE 332	3000 N	IMAGE 371	END	
X	Y	X	Y	X	Y	X	Y	
-0.2	-14.55	-0.2	-13.9	-0.3	-14.55	-0.2	-15.2	
-1.0	-15.8	-1.1	-16.1	-1.0	-15.9	-1.1	-16.1	
-4.9	-8.2	-4.4	-8.2	-4.4	-8.2	-4.4	-8.2	
-5.1	-2.2	-4.6	-2.2	-4.6	-2.2	-4.6	-2.2	
-4.8	3.9	-4.3	3.9	-4.3	3.9	-4.3	3.9	
-3.4	9.0	-3.4	9.0	-3.4	9.0	-3.4	9.0	
2.5	14.7	2.5	14.0	2.4	13.35	2.6	15.3	
2.8	14.0	2.8	14.05	2.8	14.05	2.9	14.05	
4.5	9.0	4.5	9.0	4.5	9.0	5.0	9.0	
5.7	3.9	5.7	3.9	5.7	3.9	5.7	3.9	
5.8	-2.2	5.8	-2.2	5.8	-2.2	5.8	-2.2	
5.4	-8.2	5.4	-8.2	5.4	-8.2	5.4	-8.2	
-0.2	-14.55	-0.2	-13.9	-0.3	-14.55	-0.2	-15.2	

Table 25: Values for the calculation of the Bulge Area for Specimen 1 with Elliptical Horizontal insert.

Specimen 1 - Area of the Bulge	
Instant	Area [mm ²]
IMAGE 227	236.6
IMAGE 281	224.1
IMAGE 332	223.4
IMAGE 371	235.0

Table 26: Value of the Bulge Area at different instants for Specimen 1 with Elliptical Horizontal insert.

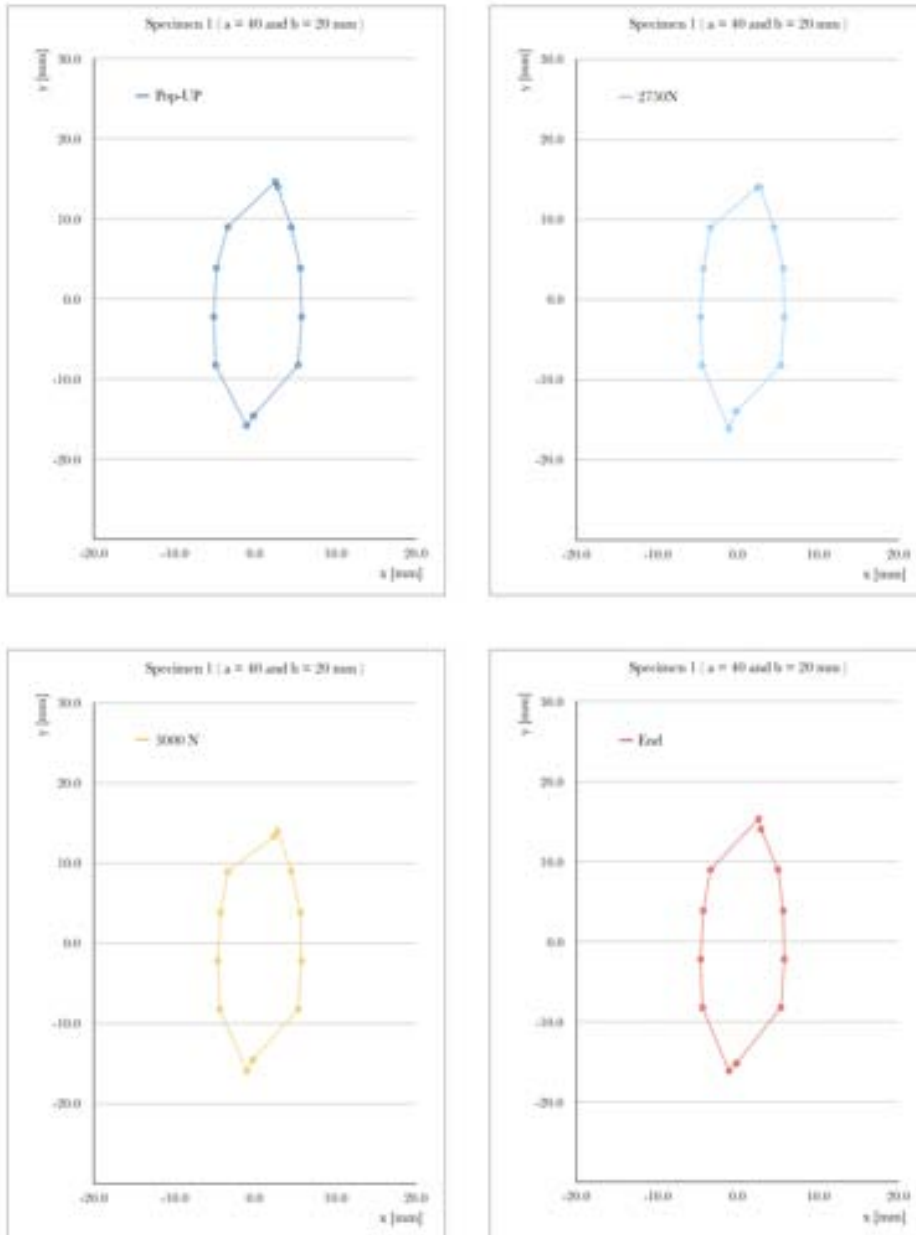


Figure 7: Bulge Area at different instants for Specimen 1 with Elliptical Horizontal insert.

Specimen 2

Specimen 2 - Area of the Bulge - SUBSET 31 STEP SIZE 10 FILTER SIZE 13 -							
IMAGE 227	POP-UP	IMAGE 272	2750 N	IMAGE 308	3000 N	IMAGE 382	END
X	Y	X	Y	X	Y	X	Y
-0.2	-10.5	-0.2	-11.1	-0.2	-11.6	-0.3	-12.1
-3.4	-14.4	-3.4	-14.3	-3.4	-14.35	-3.4	-14.4
-5.6	-7.1	-5.6	-7.1	-5.6	-7.1	-5.6	-7.1
-6.3	-0.1	-6.3	-0.1	-5.8	-0.1	-5.8	-0.1
-5.9	4.0	-5.9	4.0	-5.9	4.0	-5.4	4.0
-5.5	7.6	-5.0	7.6	-5.0	7.6	-5.0	7.6
1.75	15.7	1.55	16.1	1.8	16.4	1.8	16.5
2.3	15.0	2.3	15.0	2.3	15.0	2.3	15.0
5.0	7.6	4.45	7.6	4.45	7.6	4.45	7.6
4.5	4.0	4.5	4.0	4.5	4.0	4.5	4.0
4.6	-0.1	4.6	-0.1	4.6	-0.1	4.6	-0.1
3.2	-7.1	3.2	-7.1	3.2	-7.1	3.2	-7.1
-0.2	-10.5	-0.2	-11.1	-0.2	-11.6	-0.3	-12.1

Table 27: Values for the calculation of the Bulge Area for Specimen 2 with Elliptical Horizontal insert.

Specimen 2 - Area of the Bulge	
Instant	Area [mm ²]
IMAGE 227	224.8
IMAGE 272	222.7
IMAGE 308	221.9
IMAGE 382	221.8

Table 28: Value of the Bulge Area at different instants for Specimen 2 with Elliptical Horizontal insert.

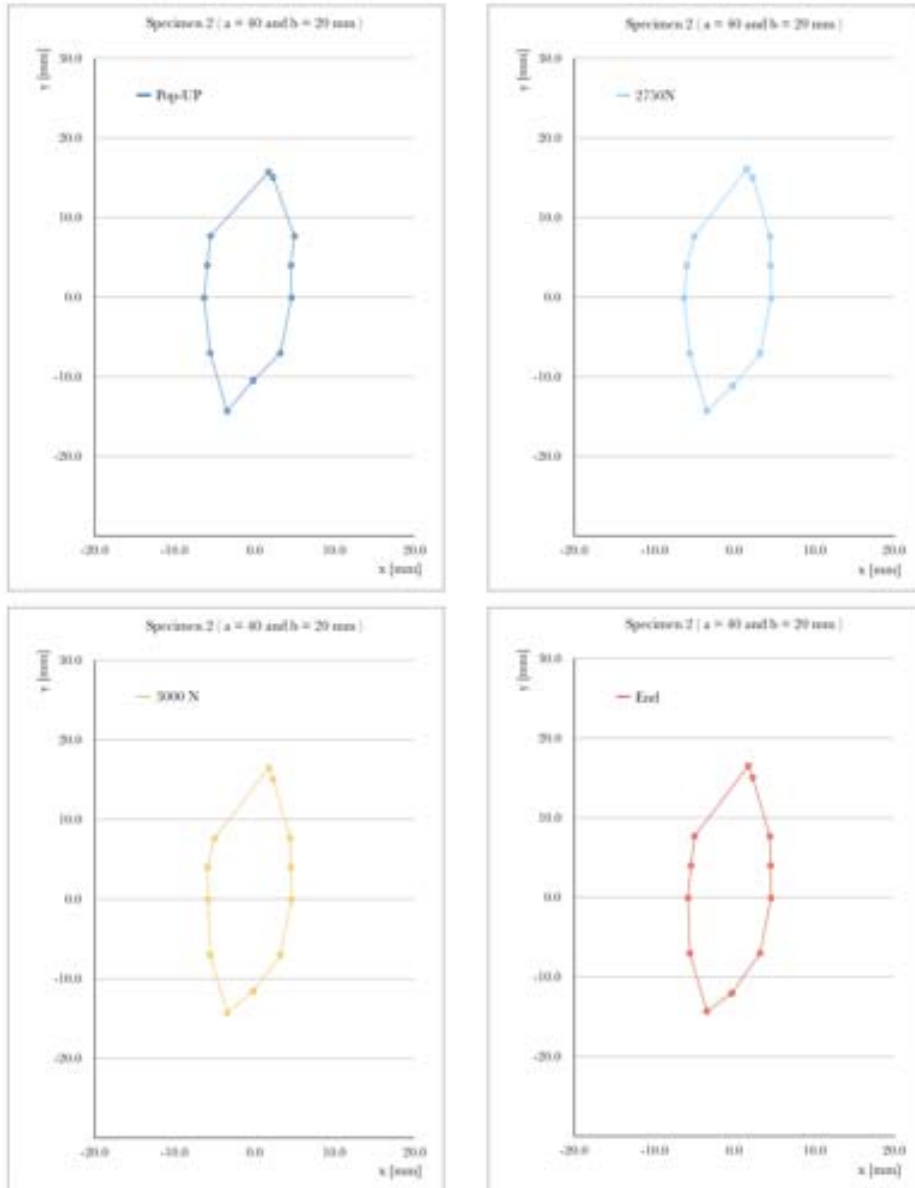


Figure 8: Bulge Area at different instants for Specimen 2 with Elliptical Horizontal insert.

Elliptical Vertical Delamination Insert

Specimen 1

Specimen 1 - Area of the Bulge - SUBSET 29 STEP SIZE 7 FILTER SIZE 15 -							
IMAGE 205	POP-UP	IMAGE 290	2750 N	IMAGE 332	3000 N	IMAGE 378	END
X	Y	X	Y	X	Y	X	Y
-0.1	-20.95	-0.15	-21.8	-0.2	-22.2	-0.2	-22.7
-2.6	-19.6	-2.6	-19.6	-2.60	-19.6	-2.6	-19.6
-4.65	-15.9	-4.65	-15.9	-4.32	-15.9	-4.65	-15.9
-6.7	-10.0	-6.3	-10.0	-5.93	-10.0	-5.9	-10.0
-7.25	-3.2	-6.5	-3.2	-6.21	-3.2	-6.2	-3.2
-7.15	3.0	-6.75	3.0	-6.42	3.0	-6.4	3.0
-6.7	10.7	-5.9	10.7	-5.94	10.7	-5.6	10.7
-4.7	16.8	-4.7	16.8	-4.66	16.8	-4.3	16.8
2.2	25.4	2.3	26.35	2.26	26.4	2.3	26.85
3.3	25.4	3.3	25.4	3.26	25.4	3.3	25.4
7.1	16.8	6.8	16.8	6.78	16.8	6.8	16.8
8.0	10.7	7.6	10.7	7.62	10.7	7.6	10.7
8.5	3.0	7.8	3.0	7.75	3.0	7.75	3.0
7.9	-3.2	7.5	-3.2	7.2	-3.2	7.15	-3.2
6.9	-10.0	6.6	-10.0	6.6	-10.0	6.2	-10.0
4.9	-15.9	4.9	-15.9	4.9	-15.9	4.9	-15.9
-0.1	-20.95	-0.15	-21.8	-0.2	-22.2	-0.2	-22.7

Table 29: Values for the calculation of the Bulge Area for Specimen 1 with Elliptical Vertical insert.

Specimen 1 - Area of the Bulge	
Instant	Area [mm ²]
IMAGE 204	542.0
IMAGE 290	518.4
IMAGE 332	509.6
IMAGE 378	506.3

Table 30: Value of the Bulge Area at different instants for Specimen 1 with Elliptical Vertical insert.

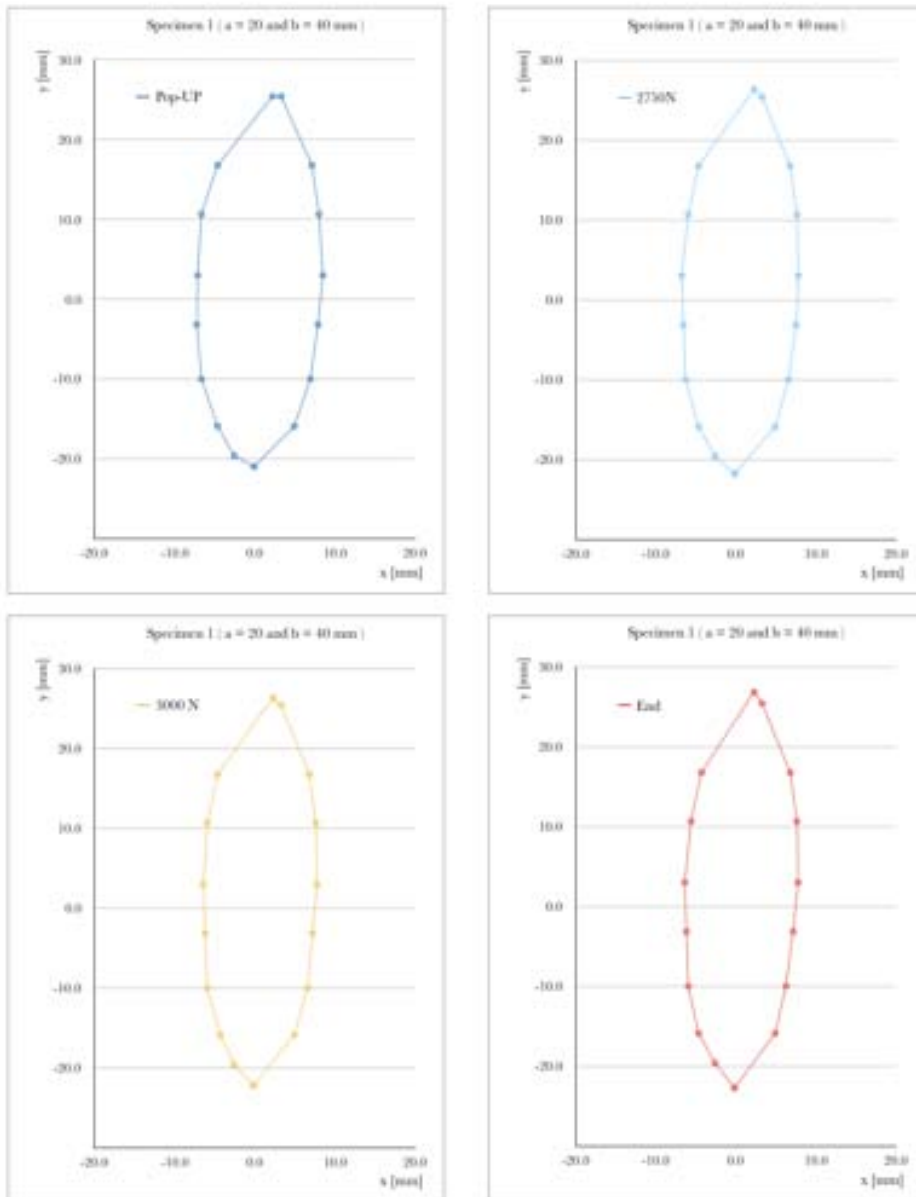


Figure 9: Bulge Area at different instants for Specimen 1 with Elliptical Vertical insert.

Specimen 2

Specimen 2 - Area of the Bulge - SUBSET 29 STEP SIZE 7 FILTER SIZE 15 -							
IMAGE 205	POP-UP	IMAGE 276	2750 N	IMAGE 313	3000 N	IMAGE 380	END
X	Y	X	Y	X	Y	X	Y
-2.3	-22.7	-2.3	-22.7	-2.3	-23.6	-2.35	-24.0
-6.5	-17.45	-6.4	-17.45	-6.4	-17.45	-6.5	-17.45
-8.1	-11.2	-7.8	-11.2	-7.8	-11.2	-7.8	-11.2
-8.7	-5.1	-8.4	-5.1	-8.4	-5.1	-8.3	-5.1
-8.95	0.7	-8.6	0.7	-8.55	0.7	-8.2	0.7
-8.8	8.0	-7.8	8.0	-7.8	8.0	-7.8	8.0
-8.0	14.6	-7.3	14.6	-6.9	14.6	-6.9	14.6
-0.8	24.1	-0.8	25.55	-0.8	25.55	-0.8	26.0
4.9	14.6	4.9	14.6	5.25	14.6	5.25	14.6
6.5	8.0	6.5	8.0	6.1	8.0	6.1	8.0
6.7	0.7	6.3	0.7	5.9	0.7	5.9	0.7
6.4	-5.1	6.0	-5.1	6.0	-5.1	5.3	-5.1
5.1	-11.2	4.75	-11.2	4.75	-11.2	4.75	-11.2
2.7	-17.45	2.4	-17.45	2.4	-17.45	2.75	-17.45
-2.3	-22.7	-2.3	-22.7	-2.3	-23.6	-2.35	-24.0

Table 31: Values for the calculation of the Bulge Area for Specimen 2 with Elliptical Vertical insert.

Specimen 2 - Area of the Bulge	
Instant	Area [mm ²]
IMAGE 205	536.9
IMAGE 276	517.8
IMAGE 313	515.6
IMAGE 380	516.5

Table 32: Value of the Bulge Area at different instants for Specimen 2 with Elliptical Vertical insert.

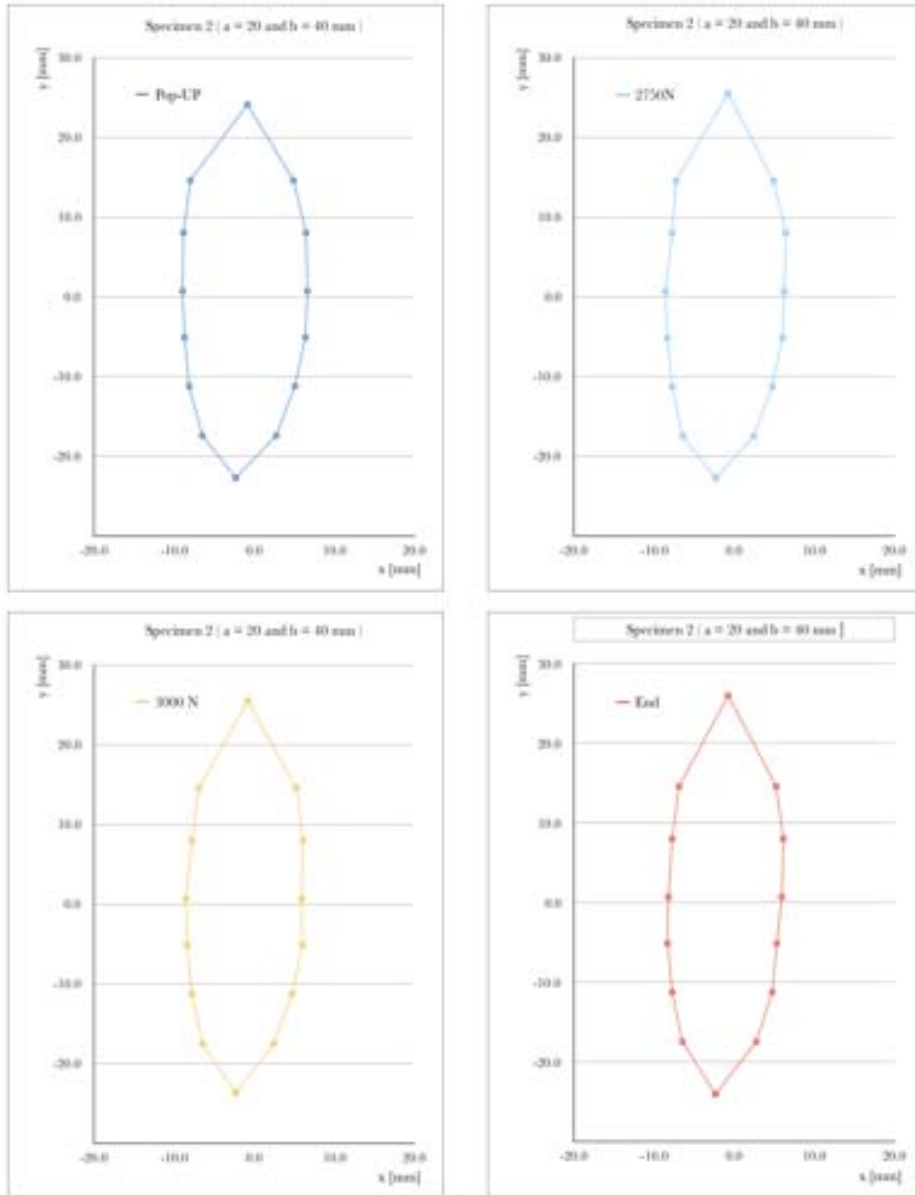


Figure 10: Bulge Area at different instants for Specimen 2 with Elliptical Vertical insert.

